A Compact and Portable Atom Interferometry System

By

Luuk Earl

A thesis submitted to
the University of Birmingham
for the degree of
DOCTOR OF PHILOSOPHY

Cold Atoms Research Group
School of Physics and Astronomy
College of Engineering and Physical Sciences
University of Birmingham
December 2020

UNIVERSITY OF
BIRMINGHAM

University of Birmingham Research Archive

e-theses repository

This unpublished thesis/dissertation is copyright of the author and/or third parties. The intellectual property rights of the author or third parties in respect of this work are as defined by The Copyright Designs and Patents Act 1988 or as modified by any successor legislation.

Any use made of information contained in this thesis/dissertation must be in accordance with that legislation and must be properly acknowledged. Further distribution or reproduction in any format is prohibited without the permission of the copyright holder.

ABSTRACT

The techniques of atom interferometry, which perform the most sensitive absolute gravity measurements to date [1], also offer potential improvement for portable sensors. For this application, atom interferometry systems must be made more portable by reducing the size, weight and power consumption while improving robustness to changing environmental conditions. This thesis presents the design and production of a compact and portable atom interferometry system. A single device with a volume of 72 L, a weight of 17.6 kg and a power consumption of 97 W was created.

A measurement scheme for gravity gradiometry in a compact package and short timescale is introduced. In addition, the design and construction of a single-arm laser system is presented. This uses a novel approach to produce two independently tuneable frequency components, capable of performing various atom-optics processes with rubidium 87. An atomic ensemble of $\sim 4.5 \pm 0.5 \ \times 10^8$ atoms of rubidium 87 was demonstrated, with two independent temperature measurement techniques giving $T = 7 \pm 2$ μK and 5 ± 2 μK. This verifies the operation of the individual sub-systems. Rabi oscillations between the ground states of the $5\ ^2S_{1/2}$ line using both a microwave antenna and a two-photon Raman transition are demonstrated, showing the ability of the system to perform coherent population transfer.

ACKNOWLEDGMENTS

I firstly thank my supervisors, Dr. Mehdi Langlois, Dr. Mike Holynski and Prof. Kai Bongs. They have provided guidance and support throughout my doctorate and beyond. Special thanks go to Mehdi for his tireless dedication to the project and his work during the Covid-19 lockdowns. My thanks also go out to Hester, and again to Mehdi for sharing in the trials of exhibiting at various events. I remember a particularly brutal rain storm which caught us off-guard in Cheltenham.

I am also incredibly grateful to the entire atom interferometry and cold atoms teams at the University of Birmingham, who created great memories and lasting friendships. It will be hard to forget the cave. Andrew, Ben, Jamie, Jonathan, Rustin, Georgina, Farzad, Yu-Hung, Samuel, Archie, Calum, Geoff, Kevin, David, Benjamin, Kyle and Adam; it was my pleasure to work with you all. I am incredibly grateful to Agathe, who brilliantly managed the various people and projects. Also to Steve and Dave in our mechanical workshop, who collaborated on and machined the vacuum chamber crucial for this thesis.

Lastly, but by no means least, I thank my family. Mum, Dad, Janni and James; I thank you for the support and interest. My biggest thanks go to Georgina, who helped me in every way. I must also thank Rufus and Bjorn for their patience, their species has an awkward history with quantum mechanics.

AUTHOR CONTRIBUTIONS

This project was funded by the UK Defence Science and Technology Laboratory (DSTL) as part of the *Gravity Imager* project. This was part of a national programme of research aimed at developing quantum science for particular applications: the UK national quantum technology hub for sensors and timing. Partners from DSTL, along with my supervisors Prof. Kai Bongs and Dr. Michael Holynski, defined the scope of the project along with particular targets for the size, weight and power consumption.

Much of the conceptual design work was performed in collaboration with post-doctoral researcher Dr. Mehdi Langlois. Specifically, we developed the concepts for using a Bloch elevator to create two spatially separated clouds together. Also, the concept for using two IQ modulators in series to create an agile, single arm laser system was done in collaborataion. These two ideas have been filed for patent applications ZSR1208A ("Apparatus for generating vertically separate atom clouds") and ZSR1208B ("Laser System").

I developed the concepts for the compact packaging, including the modular sub-system approach and flexible laser and microwave chain systems. The design of the vacuum system and peripherals was completed by myself. I led the building and development of the system apparatus, such as the vacuum chamber, laser system and microwave chain, with primary support from Mehdi. Similarly, I led all of the experimental work to verify the system with support from my supervision team.

Contents

List of Figures

List of Tables

Acronyms

AOM Acousto-Optic Modulator. ix, 89, 99–101, 108–110

ARP Adiabatic Rapid Passage. 23

CAD Computer Aided Design. 58, 77, 80, 85

DAC Digital to Analogue Converter. 89, 108, 109

DDS Direct Digital Synthesiser. 89, 107

DRO Dielectric Resonator Oscillator. 89, 107

EDFA Erbium Doped Fibre Amplifier. 89, 99

EMI Electromagnetic Induction. 1, 2

EOM Electro-Optic Modulator. 89, 94–96, 103, 104

FM Frequency Modulation. 89, 102, 103

FPGA Field Programmable Gate Array. 89, 108, 109

FWHM Full Width at Half Maximum. 115, 123–125

GPR Ground Penetrating Radar. 1, 2

GPS Global Positioning System. 1, 22

IQM In-phase Quadrature Modulator. viii, ix, 89, 92, 94–100, 102, 106–108, 110

MEMS Micro-Electromechanical System. 1, 13

MOT Magneto-Optical Trap. vii–x, 23, 24, 29, 30, 32, 33, 58, 64, 71–74, 79–81, 84, 115–121, 123, 125, 150, 151

OCXO Oven Controlled Crystal Oscillator. 89, 105

OSSB Optical Single Side-Band. 89, 94–96, 102

PBS Polarising Beam Splitter. 89, 104

PCB Printed Circuit Board. 89, 103

PDH Pound-Drever-Hall. 89

PID Proportional Integral Derivative. 89, 103, 104

PPLN Periodically Poled Lithium Niobate. 89, 99, 100, 103

QHC Quality Hybrid Coupler. 89, 107, 108

RF Radio Frequency. ix, 89, 104, 107, 110, 111, 113, 114

SCOSSB Suppressed Carrier, Optical Single Side-Band. 89, 94–96, 102, 106

SHG Second Harmonic Generator. ix, 89, 100, 101

SMA Sub Miniature version A. 89, 110

SWaP Size, Weight and Power. xi, 1, 6, 8, 10, 11, 15, 20, 89, 105, 109, 110, 114, 135–138

UAV Unmanned Aerial Vehicle. 58, 59

UHV Ultra-High Vacuum. 1, 10, 11, 58, 70

VVA Voltage Variable Attenuator. 89, 100, 108, 109

Chapter One

Introduction

1.1 Sub-surface Mapping

Underneath the surface of the Earth is a whole world of structures, some human-made and some natural. Although normally imperceptible, these structures have a huge impact on daily life. Whole networks of pipes carrying power, clean water and sewage underlay our cities. Mineral deposits lay undetected beneath our feet. The motion of bulk material underground can cause sink holes, earthquakes and volcanoes. Being able to map and monitor these sub-surface structures would improve our ability make use of the space underneath our feet and reduce the risk to human life. This is the aspiration of the field of sub-surface mapping.

Currently, a typical method for performing maintenance on utility pipes is to dig large trial holes. The ability to map the location and type of service pipe from the surface would allow more efficient use of money and time. This can be extended to the monitoring of sink holes. In the United States, sink holes cost at least $300 million a year [2]. Being able to monitor the composition of material below our cities would allow the early detection

and prevention of sink holes forming. In the construction sector, it is necessary to survey a potential site before construction begins. A map of the composition of potential sites taken from the surface could save vast amounts of money. Furthermore, if deposits of valuable natural resources such as metals and oil could be mapped, it would vastly reduce the cost and environmental impact of prospecting. Finally, many human-made structures have been left by our ancestors. A device which could map the underground could enable archaeologists to find new and exciting discoveries.

All of the above examples rely on a sensor which can image structures underground. To be useful in these field applications, such a sensor would have to be portable, robust and easy to use. To produce a map of an area the sensor would have to be moved across a site, measuring either constantly or point-to-point. Ideally, these sensors could be moved and operated by one or two people. Many of the applications require use in rugged environments with less than ideal conditions, the sensors must be robust enough to work in such environments. Also, the operators will not necessarily be experts in the sensor technology so ease of use is key.

Several sensor technologies exist currently which are capable of sub-surface measuring. The most obvious is the method of digging trial holes. While this commonly used method can give an accurate picture of composition, it is time consuming, expensive, disruptive and potentially destructive of any interesting features. Another technique is to use electromagnetic inductive (EMI) sensing. This relies on the sensor inducing a current in underground objects, creating a measurable electro-magnetic field. They are very portable, yet can only map certain materials [3]. The technique of ground penetrating radar (GPR) is also commonly used in sub-surface mapping. GPR relies on detecting the radar signals reflected from underground objects [4]. This technique works best for objects with a reflective boundary with the surrounding material. GPR has limited range as the signals emitted are attenuated by the medium they propagate in. Finally, gravity sensing can be used to

map the underground. This is a passive measurement which relies on detecting the subtle changes in the gravitational acceleration due to the density difference of sub-surface objects.

A benefit of gravity sensors is they can potentially detect objects at arbitrary depth, not being limited by signal attenuation. Gravity sensors can theoretically detect any density difference between two neighbouring materials (usually the difference between soil and a high density object or between soil and a cavity), allowing detection of a huge variety of objects. Due to this, gravity sensing is highly complimentary to other measurement technologies, but not in itself a complete solution. Rather, to build a full picture, a suite of different sensors would be used to image sub-surface structures. While gravity sensing has many benefits and has seen extensive use in surveying [5], there is potential for the technique to become more utilised as the technology improves. To be able to detect smaller objects at a greater depth, the sensitivity of survey relevant devices needs to be improved. Also, to be able to produce maps at a higher spatial resolution, the measurement speed of gravity sensors needs to be increased and the robustness refined.

1.1.1 Gravimetry

Gravity sensors can be divided into two categories: Absolute sensors and relative. An absolute sensor will measure a value of local g, such as via free fall. A commercially available example of an absolute gravimeter is the *Micro-g LaCoste FG5-X* [6]. This measures the falling rate of an in-vacuum corner cube using a Michelson light interferometer. It is precise and accurate but not designed for mobile measurements. Relative gravimeters need to be calibrated against an absolute sensor in order to produce accurate readings. They are typically more prone to measurement drift. The technology used ranges from superconducting levitation [7] to *MEMS* devices, including recent examples [8, 9]. These devices typically can be understood as a mass-on-spring, whether the spring be micro-scale or a magnetic field.

The most pervasive portable relative gravity sensor is the *Scintrex CG-5 Autograv* [10].

However, despite the benefits, gravity sensing is still less commonly used in surveying than other geophysical approaches. A large drawback of gravity sensing is the large measurement times required to produce accurate results. Gravity sensors measure acceleration, meaning any external acceleration of the sensor itself will be interpreted as a change in the measured gravity signal. Such external acceleration can arise from vibrations of the ground, caused by things such as local traffic. Sensitive gravimeters are also affected by micro-seismic vibrations from waves hitting the coast across the UK. To overcome this issue, a gravimeter is typically measured on a single point for long periods to average out the vibrations and produce an accurate result. This process inflates the measurement times necessary for gravity sensors and inhibits their wide-spread use.

1.1.2 Gravity Gradiometry

A particular issue with gravity sensing is dealing with vibration. Gravimeters are in essence accelerometers so any vibration of the sensor will couple into the gravity measurement. This can often be a leading source of noise in gravity measurements. The effect of vibration can be mitigated by averaging the measurement of gravity in a particular point for a long time. This produces more accurate results but vastly increases measurement time. In addition, the sensor can be placed on a vibration isolation stage. This passively compensates the vibrations felt by the sensor, although does not address low frequency noise. These isolation stages are often large in size and heavy, so not ideal for a portable sensor.

An alternative approach is to use a *gravity gradiometer*. Here, two measurements of gravity are made, separated vertically by a baseline, and subtracted. Of particular interest is the use of common mode suppression, where vibration common to both measurements

is subtracted and cancelled. However, this is only possible if the two measurements are simultaneous and coherently linked. The technique gives a gradient of the gravity signal rather than a pure measurement of gravity itself. Although this does remove some ability for *absolute* gravity measurements, for most surveying applications it is the differences from point to point that are important.

1.2 Defining the Problem

A candidate for improving portable gravimeters comes from the field of fundamental physics. *Atom interferometers* have been developed since the early 90's [11], using a cooled cloud of atoms as a test mass. Gravimeters using this technique currently lead the state of the art for precision measurements [1]. They have also been used to test the universality of free-fall [12] and measure the Newtonian gravitation constant [13]. While these instruments are the most sensitive in the world, they are not designed for portable use in a field environment. The fundamental technologies of these instruments are very scale-able however, so it is feasible to design a portable sensor based on these techniques.

The methods of atom interferometry allow a simultaneous gravity gradient measurement. This is achieved by a single coherent laser interacting with two atom ensembles, coupling the measurements and allowing for common mode suppression. Atom interferometry presents an interesting tool to improve gravity sensing for rapid field measurements. It allows a scheme with common mode rejection which can drastically improve measurement speed as the requirement on averaging is alleviated. The techniques can also be highly precise and with good spatial resolution. However, the challenges of producing such a sensor at a convenient size, weight and power must be overcome. Addressing these challenges will be the central theme of this thesis.

The field of using using atom interferometry to improve gravity surveying is presented as a "ladder of abstraction" in figure 1.1. The central question is framed by *why* the problem is important and *how* it might be tackled. Understanding why this is important motivates the work in successively more abstract terms. Asking how the problem can be addressed introduces granularity into the problem, defining the particular points that will be relevant to a research project.

While by no means a complete representation of the problem, figure 1.1 gives an insight into the salient points of this research field. Some work has already been done to explore the points in this diagram, some of which is summarised in section 1.3. The work presented in this thesis will focus on the problem of designing and building a person-portable atom interferometer capable of gravity gradient measurements. This will involve work in designing a compact gradiometer scheme, developing low SWaP (size, weight and power) sub-systems and understanding the systems engineering of a compact atom interferometer. This work will demonstrate the readiness of atom interferometry as a viable technique for gravity surveying.

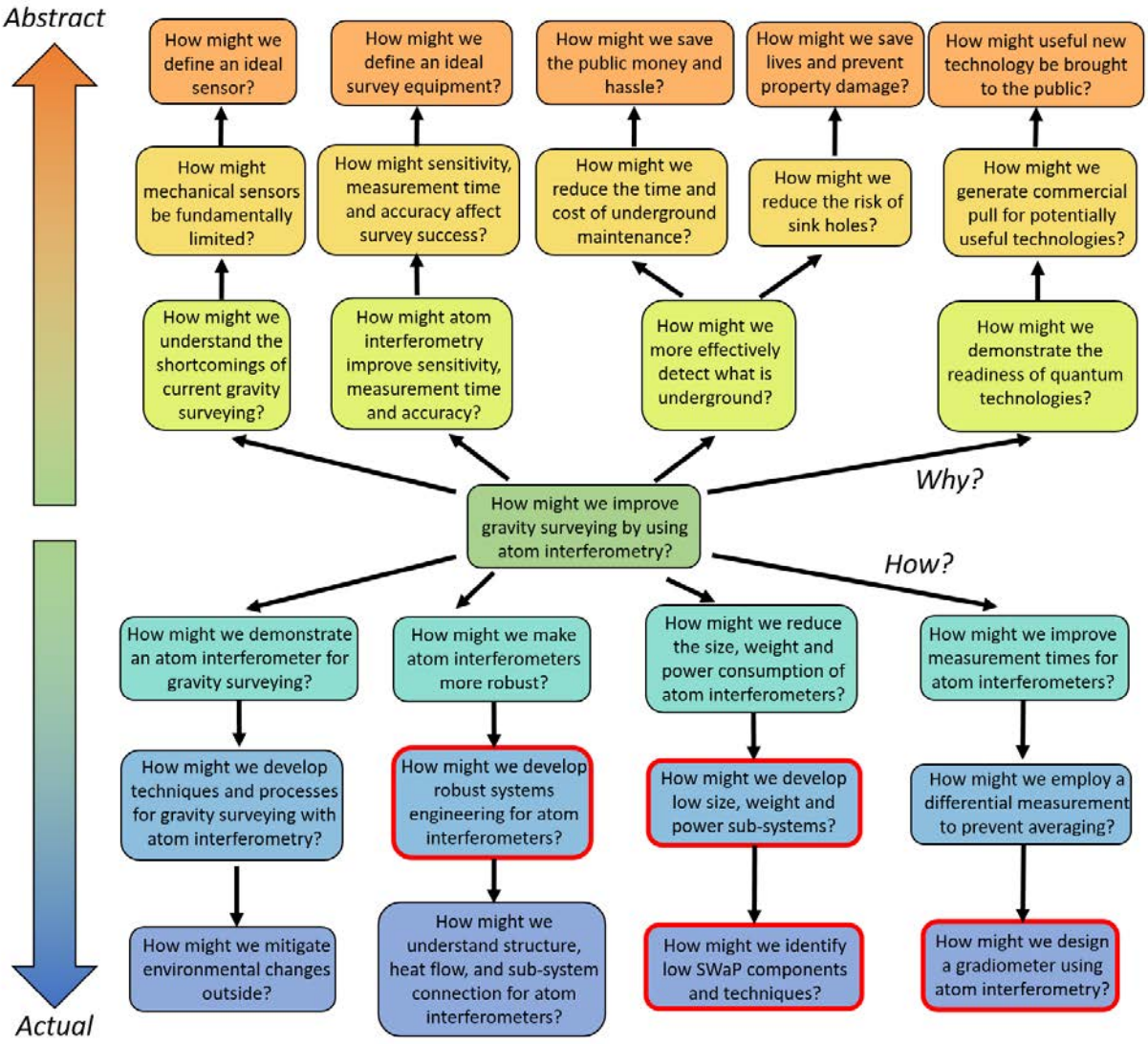

Figure 1.1: A "ladder of abstraction" for the question of how atom interferometry might improve gravity surveying. The problem statement can be framed by asking *why* this question is relevant. These are shown above the central statement, the reasoning becoming more abstract. The problem can be broken down by asking *how* this might be achieved. The answers to this are presented below, becoming more granular and specific. The particular points addressed in this work are outlined in red.

1.2.1 Sensor Performance

For discussing the merit of portable sensors the main comparison points will be the accuracy, sensitivity, stability, measurement rate, size, weight and power consumption (SWaP). The accuracy (given in nm s^{-2}) indicates the smallest deviation from the true value of gravity achievable. The sensitivity (given in nm $s^{-2}/\sqrt{Hz}$) indicates the precision with which measurements can be made. This represents the uncertainty in each measurement caused by noise. It is a measure of the short term stability. The stability (given in nm s^{-2}, usually specified over a time frame) indicates the extent to which the instrument output changes over time. The measurement rate (measured in Hz) indicates the speed with which the sensor can perform a single measurement. A higher rate means the sensor can perform measurements faster. The SWaP characteristics indicate how portable the sensor is. Low SWaP is desireable.

1.2.2 Atomic Sensors

Atom interferometry is a subset of the wider *matter-wave interferometry* field. These phenomena are understood in terms of the wave-particle duality of light and matter. In certain circumstances light can behave as if made of discrete particles (photons). Similarly, matter can be observed to behave as if it were a wave. The earliest examples of this were the famous double-slit experiments performed using electrons [14, 15]. This remarkable result was then later observed to also be true for atoms [16, 17, 18]. It can be seen from this that atoms can exhibit wave-like properties and be made to *interfere*. From this concept the prospect of an *atom interferometer* arises.

At roughly the same time as double-slit experiments were being performed with atoms in the early 90's, Kasevich and Chu performed their seminal work demonstrating the use of

an atom interferometer as a gravity sensor [11]. The concept is to create a Mach-Zehnder like interferometer but rather than use the interference of *light* to measure a path length difference, *atoms* would be put into a quantum superposition and interfered to measure inertial effects. This effectively marries the ability of interferometers to measure very precisely with atoms being sensitive to gravity (as they have mass). Representations of a Mach-Zehnder and atom interferometer are shown in figure 1.2

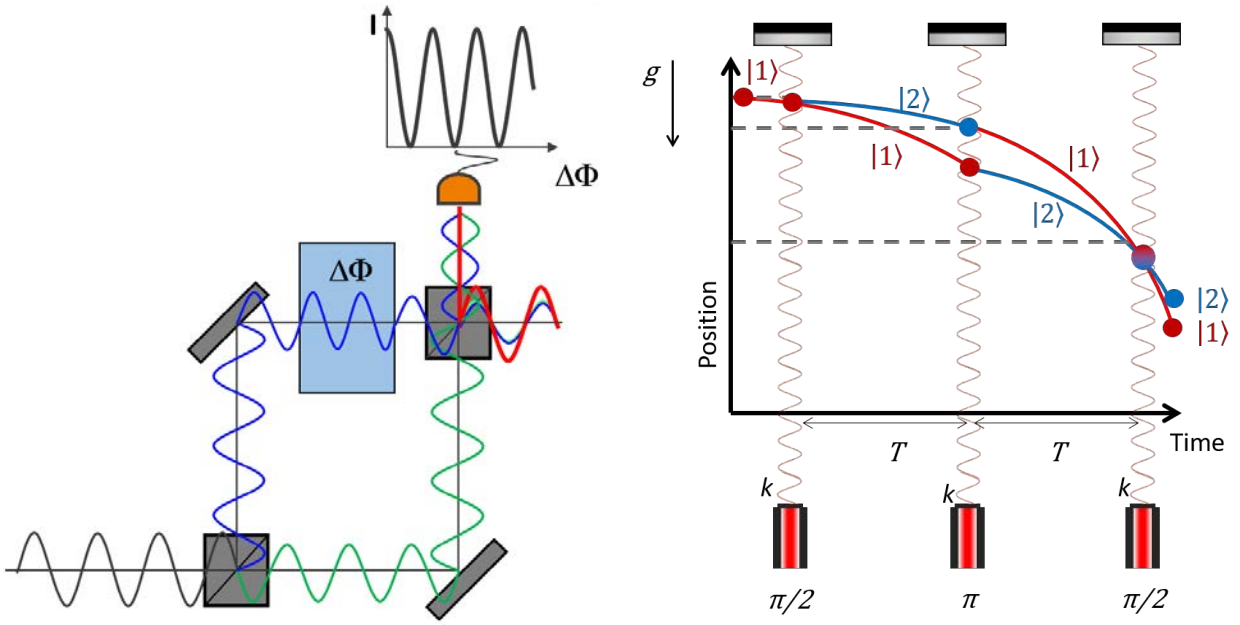

(a) A Mach-Zehnder light interferometer

(b) A gravity sensitive atom interferometer

Figure 1.2: A diagram showing the analogy between Mach-Zehnder light interferometers and atom interferometry. In a light interferometer, a coherent beam is separated with the two arms traversing separate paths controlled by mirrors. The beams are recombined where the path difference between the two arms $\Delta\Phi$ can be measured by observing the interference pattern. Similarly for an atom interferometer the atomic wave-packet is put in a superposition between the two arms traversing different paths, controlled by laser pulses coupled to internal and momentum states. The atomic packets are recombined, here the interferometric phase is measured as a relative population between the two internal states. The phase difference is used to measure gravity.

The operation of the $\pi/2 - \pi - \pi/2$, Kasevich-Chu [11], atom interferometer is analogous to that of the Mach-Zehnder interferometer, however the roles of light and matter are inter-changed. Rather than interfering light and controlling the path of the two arms with matter (mirrors and beam-splitters), matter is interfered and the path of the two atomic packets is controlled by light. This light is delivered as three pulses separated by time T. The pulses coherently transfer the atomic population between two states, using a two-photon transition (*Raman*) in a multi level atom, and couple this internal state to an external momentum state. A more detailed description of Raman transitions, the atom interferometer, and how it can be made sensitive to gravity are given in chapter 2. In the simplest sense an atom interferometer measures gravity by dropping a mass (atoms) and measuring the acceleration caused by gravity.

As the collection of test masses (an atomic ensemble) in an atom interferometer is in free-fall, it performs an *absolute* measurement of gravity. Atoms as a test mass are also "ideal" as each atom of the same species is identical and will always be. The atomic species itself, and therefore the energy transitions, are a constant. Combined with this, the atoms are isolated from the external environment in an ultra-high vacuum so there can be no drift or wear of the test mass. This allows atomic sensors to have the potential to realise low drift. However, care must be taken with magnetically sensitive species to appropriately shield external magnetic fields.

Also, the technologies and techniques of atom interferometry are *scalable*. The techniques used to perform the most sensitive acceleration measurements are the same that would be used for a person-portable sensor, namely the atom-light interactions. The technologies are also *miniaturisable*. The main technologies are UHV (ultra-high vacuum), lasers and radio frequency (RF) electronics. Standard RF and power requirements are used, once designed these could be manufactured more compactly on circuit boards. UHV technology, although has been high SWaP historically, is not fundamentally limited and in recent years incredibly

low SWaP UHV systems have become commercially available [20, 19]. Similarly, laser technology is constantly developing with more precise, higher power and low SWaP components becoming available. Particularly with the use of rubidium-87, telecoms laser components can be used (1560 nm light for telecoms via frequency doubling to the 780 nm required for ^{87}Rb). This allows atom interferometry to connect to highly developed technologies from the telecommunications industry.

The atom shot noise limited sensitivity of an atomic gravimeter is given by the interferometry time, T, the momentum splitting, $k_{\text{effective}}$, and the atom number N. This is the limit on the sensitivity of the instrument imposed by the random nature of detection. In a typical sequence designed for gravity sensing, the shot noise sensitivity is calculated as

$$\delta g_{SN} = \frac{1}{\sqrt{N}.k_{eff}.T^2} \ . \tag{1.1}$$

1.2.3 Atomic Gravity Gradiometers

Of particular interest for mobile measurements is the potential of atom interferometry based gravity gradiometry. Gradiometry can offer faster measurement output times as there is less requirement for averaging. However, this is only the case where there is common mode suppression between the measurements. The use of atom-light interactions, where the atom clouds are interrogated by the same light simultaneously, is particularly interesting for gravity gradiometry as the two measurements are directly coupled so have excellent common mode suppression [21].

As a gravimeter essentially measures vibration, any vibration of the platform the sensor is on will contribute to the measurement. This is often alleviated by employing auxiliary accelerometers [22] or a large and weighty anti-vibration platform [1]. The differential mea-

surement of a gravity gradiometer provides the common mode rejection that reduces the effect of environmental vibration on the instrument. This is particularly important at low frequencies which are difficult to isolate but ubiquitous in the UK (noise caused by waves striking the coast), causing issues in civil engineering applications [23]. By using a gravity gradiometer with common-mode suppression of vibration, a measurement can be obtained faster in the presence of vibration.

Atom interferometry is especially promising for gravity gradiometry. The two measurements are inherently linked by the interrogating laser which simultaneously interacts with both test masses. For a gradiometer the shot noise sensitivity is the gravimeter sensitivity divided by the baseline between measurement points. This is shown as

$$\delta\Gamma_{SN} = \frac{1}{\sqrt{N}.k_{eff}.L.T^2} \ , \tag{1.2}$$

where L is the baseline separation.

By using an atom interferometry based gravity gradiometer, it is likely that the measurement will be limited by sensor sensitivity rather than environmental inertial noise. By using atomic sensors it is possible to create a system with the improved measurement times of a gravity gradiometer with common mode suppression, a high sensitivity and a compact design, showing a large step towards superiority of a quantum sensor. This potential makes this an interesting research topic.

1.3 Gravity Surveying Instruments

Some methods of gravity surveying were briefly discussed in section 1.1. A more detailed comparison of the available technologies will be presented in this section. Firstly, the avail-

able relative instruments for portable surveying will be outlined and compared. These are all based on classical mass-on-spring type systems. Then available absolute gravity sensors that are designed for portability will be compared. Generally these are atom interferometers that are research instruments, however the commercially available *Micro-g LaCoste FG5-X* will also be included. Finally, gravity gradiometers will be compared, both the state of the art in classical and atom interferometry instruments.

1.3.1 Relative Gravimeters

The relative gravimeters chosen for comparison are representative instruments of the technology used. While all designed to be transportable and used in the field, the technology used defines this ability. An important comparison for relative gravimeters is the accuracy, indicating how close the instrument gets to the true value of gravity (measured by comparison to an absolute sensor). For relative gravimeters the drift and stability of the instrument are also crucial. This indicates how much the measured values will change due to an external factor or time. Four relative gravimeters indicative of the technology used are compared in table 1.1. The state of the art of portable gravimeters is the *Scintrex CG-6*, delivering 50 nm s^{-2} level accuracy in a 10 L, 5 kg package.

As can be seen from table 1.1 the available relative gravimeters span a wide range of precision and portability. The instrument most person-portable is the *Scintrex CG-6*, which also has a good showing for accuracy. Superconducting sphere gravimeters are generally accurate and precise, however require specialist cooling liquids. MEMS gravimeters are so far less accurate but offer very fast measurement rates, allowing faster averaging.

Table 1.1: Comparison of relative gravimeters, representative of some key technologies available.

Institute *Instrument* *Principle*	Sensitivity Accuracy	Measurement Rate Drift	Volume Weight Power	References
Scintrex † *CG-6* *Quartz Spring*	N/A 50 nm s^{-2}	10 Hz 200 nm s^{-2}/day	10 L 5 kg 10 W	[10, 24, 25]
CSRI † *Chekan* *Torsion Fibres*	N/A 700 nm s^{-2}	50 Hz 5.6 μm s^{-2}/day	77 L 78 kg 300 W	[26, 27]
GWR † *iGrav* *Superconducting*	3 nm $s^{-2}/\sqrt{Hz}$ 0.01 nm s^{-2}	1 Hz 0.06 μm s^{-2}/day	104 L 37 kg 1.3 kW	[7, 28, 29]
Glasgow ⋆ *Wee-g* *MEMS spring*	400 nm $s^{-2}/\sqrt{Hz}$ 100 nm s^{-2}	0.03 Hz 1.5 μm s^{-2}/day	$\sim$ 0.2 L* - N/A	[9, 30]

⋆ University

† Company

*Excluding control electronics

1.3.2 Absolute Gravimeters

For absolute gravimeters, the absolute measurement isn't as important (so long as drift can be ignored) as changes between locations. Absolute gravimeters have the benefit of not having drift, so generally don't have to be calibrated. The state of the art in classical absolute gravimeters is the *Micro-g LaCoste FG5-X*, based on a falling corner cube light interferometer, with 150 nm $s^{-2}/\sqrt{Hz}$ sensitivity and 20 nm s^{-2} accuracy. This instrument is designed for stationary measurement campaigns and as a reference. In recent years several gravimeters based on atom interferometry have been developed. Some of these are compared in table 1.2. While designed to be transportable, most of these are research instruments so information on the SWaP characteristics is limited. They are designed for a variety of applications, including ship-borne and air-borne measurements, so have not necessarily tried to minimise SWaP to be person-portable. The *AQG* from *μQUANS* exhibits a commercially available atomic sensor which is comparable in specification to the *FG5-X* with 500 nm $s^{-2}/\sqrt{Hz}$ sensitivity and <10 nm s^{-2} accuracy in a 430 L, 100 kg package.

While much exemplary work is being done in developing atom interferometry for use in gravity surveying, the size and weight of these systems is not currently representative of a person-portable instrument. The sensitivity of some absolute gravimeters shown in table 1.2 already surpasses some of the incumbent classical instruments. This is incredibly promising for the use of atom interferometry as these represent the first generation of devices aimed at trans-portability. The scientific techniques can be developed and improved upon significantly as the field is very young. The design and engineering of such instruments can also be greatly improved, especially as the technology moves into commercial development.

From studying the technology available to end users in sub-surface mapping and understanding of the research into portable atom interferometers for gravity, a gap in the field presents itself. Atom interferometers have great potential to revolutionise gravity mapping [1,

Table 1.2: Comparison of available absolute gravimeters

Institute *Instrument* *Principle*	Sensitivity Accuracy Stability	Measurement Rate	Volume Weight Power	References
Micro-g † *FG5-X* *Corner cube*	150 nm $s^{-2}/\sqrt{Hz}$ 20 nm s^{-2} N/A	N/A	1500 L 150 kg 500 W	[6]
Berlin ⋆ *GAIN* ^{87}*Rb Fountain*	96 nm $s^{-2}/\sqrt{Hz}$ 39 nm s^{-2} 0.5 nm s^{-2}	0.7 Hz	2000 L 160 kg <1 kW	[31, 1]
μQUANS † *AQG-A01* ^{87}*Rb Drop*	500 nm $s^{-2}/\sqrt{Hz}$ <10 nm s^{-2} 10 nm s^{-2}	2 Hz	79 + 350 L 25 + 75 kg 300 W	[32, 33]
Zhejiang ⋆ *CAAG* ^{87}*Rb Drop*	3000 nm $s^{-2}/\sqrt{Hz}$ 158 nm s^{-2} 30 nm s^{-2}	2 Hz	85 + 540 L 70 kg* N/A	[34]
ONERA † *GIRAFE* ^{87}*Rb Drop*	8000 nm $s^{-2}/\sqrt{Hz}$ 1700 nm s^{-2} N/A	10 Hz	16 L* N/A N/A	[35, 36, 37]
Berkeley ⋆ *MAI* ^{87}*Rb Drop*	370 nm $s^{-2}/\sqrt{Hz}$ 400 nm s^{-2} 20 nm s^{-2}	N/A	1360 L 100 kg 250 W	[38]
SYRTE † *CAG* ^{87}*Rb Drop*	57 nm $s^{-2}/\sqrt{Hz}$ 1 nm s^{-2} 2 nm s^{-2}	3 Hz	2550 L N/A N/A	[39, 40]
Wuhan ⋆ *Gravimeter* ^{87}*Rb Fountain*	42 nm $s^{-2}/\sqrt{Hz}$ 10 nm s^{-2} 3 nm s^{-2}	1 Hz	400 + 80 L N/A N/A	[41]

1 μGal = 10 nm s^{-2}

⋆ University

† Company

*Sensor head only

32, 35, 36, 38]. However, little work has been done to really miniaturise atom interferometers for smaller scale surveys. No atom interferometer to date is close to matching the small package of the *Scintrex CG-6* [24].

1.3.3 Gravity Gradiometers

There are numerous commercial gravity gradiometers based on classical sensors [42]. These are typically aimed at large feature scale, such as mineral prospecting surveys, usually airborne measurement campaigns over many kilometres squared. Of particular prevalence are the *Gravity Gradient Instrument (GGI)* and *Full Tensor Gradiometer (FTG)* from *Lockheed Martin* [43]. These sensors exhibit extraordinary performance and are typically used in surveys of large areas for mapping and mineral prospecting from an airborne vehicle. Recently, some gravity gradiometers based on atom interferometry have been developed. These are typically laboratory based experiments. However, the potential reduction in measurement time makes these an exciting prospect for use in localised survey, such as to detect pipes or local voids.

Gravity gradiometers can be created using atom interferometry by producing two atomic gravimeters separated by a baseline and interrogating them with the same laser pulses. This process couples the two measurements so they can be subtracted. Gravity gradiometers with common mode suppression have several benefits for surveying over gravimeters (section 1.2.3), most importantly being the decreased averaging time and reduced tilt sensitivity. The key parameters when comparing gravity gradiometers are the sensitivity, accuracy, measurement rate and baseline. The gradiometer accuracy is measured in *Eötvös*, which is the gravimeter accuracy per meter baseline (1 E = nm s^{-2}/m = 10^{-9} s^{-2}). The *Lockheed Martin* sensor, the state of the art in sensitivity (0.5 E/$\sqrt{\text{Hz}}$), is compared to some atom interferometer gravity gradiometers in table 1.3. These are mostly laboratory based

Table 1.3: Comparison of available gravity gradiometers, representative of technology used.

Institute *Instrument* *Principle*	Sensitivity Accuracy	Measurement Rate Baseline	References
Lockheed Martin † *GGI* *Full Tensor*	0.5 E/$\sqrt{\text{Hz}}$ 10 E	5 Hz N/A	[43, 42]
Yale, Stanford ⋆ *(Kasevich)* *Gradiometer* *Atom Interferometry*	4 E/$\sqrt{\text{Hz}}$ 1 E	50 Hz 10 m	[45]
Wuhan ⋆ *Gradiometer* *Atom Interferometry*	670 E/$\sqrt{\text{Hz}}$ N/A	0.25 Hz 0.45 m	[46]
JPL † *Gradiometer* *Atom Interferometry*	40 E/$\sqrt{\text{Hz}}$ 1 E	1 Hz 1 m	[47]

⋆ University

† Company

1 E = 10^{-9} s^{-2}

experiments with a range of baselines used, but are becoming comparable in accuracy and sensitivity in a similar package size. The gradiometer from the *Jet Propulsion Laboratory (JPL)* exhibits an accuracy of 1 E and a sensitivity of 40 E/$\sqrt{\text{Hz}}$ with a 1 m baseline.

Of particular note to the work of this thesis are the systems being produced by the *University of Birmingham* [21] and *Teledyne e2v* [44]. This work, as part of the UK national quantum technology hub, has been undertaken in parallel to the work in this thesis. The system from *Birmingham* demonstrates some early work in developing atom interferometry based gravity gradiometers for use in the field. The work of *Teledyne e2v* builds on early work in conjunction with *Birmingham* to develop commercial systems.

The atom interferometry gravimeters and gravity gradiometers that have been developed in recent years (tables 1.2, 1.3) are matching and even surpassing the incumbent classical sensors in terms of sensitivity and accuracy. However, a gap still exists between the field capable classical sensors and the research instruments based on atom interferometry. This is in the compactness, portability and robustness. If an atom interferometry based gravity gradiometer could be designed into a package that is comparable in portability with current classical gravimeters, high precision and fast surveying on smaller scales might be possible.

1.4 Scope of this Thesis

The work of this thesis aims to address a gap in the development of atom interferometers for gravity surveying. Sensing via gravity has many uses; static high precision measurements, instruments on vehicles for large scale mapping, transportable sensors for civil engineering and even person-portable devices for rapid surveying. Currently, surveying using gravity sensing is not feasible at high measurement rates. This is one of the main drawbacks of using gravity sensing for sub-surface mapping.

The work of this thesis aims to address this issue by investigating the potential for atom interferometry based gravity gradiometry in a portable package. This builds on work previously undertaken at the *university of Birmingham* [21] and fits with the wider goal of the UK national quantum technology hub in developing quantum sensors for field applications. The work presented here will outline the design and development of a person-portable atom interferometer for future field applications such as surveying.

The system has been designed to allow for gravity sensing using multiple different schemes. Measurements can be made as an atomic ^{87}Rb drop, a ^{87}Rb fountain and several

different gravity gradiometry schemes. The sensor head has been designed and constructed with a minimal footprint while maintaining a high potential sensitivity. Sub-systems for the laser, frequency generation, power supplies and computer control have all been designed and built with a low SWaP. The concept for the system integration and packaging is shown in figure 1.3 and the SWaP budget break down is shown in table 1.4. A systems engineering approach has been taken to produce a single sensor package with consideration of heat transfer, weight distribution and ease of use. In summary, the sensor is designed to allow 304 nm $s^{-2}/\sqrt{Hz}$ measurements in an 88 L, 20 kg package consuming less than 150 W. This would be a state of the art performance but in a package fit person-portable survey. Already with the first iteration of this work the sensitivity and portability are projected to be comparable with the current state of the art at this sensor scale.

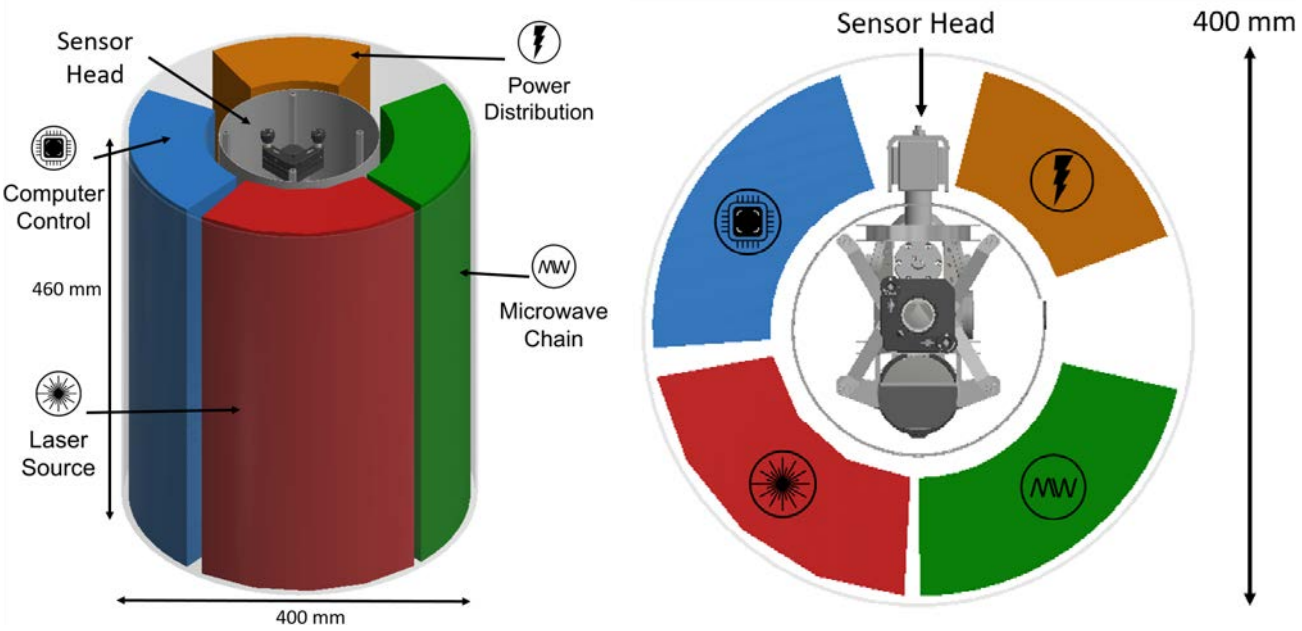

(a) Front view.

(b) Top view.

Figure 1.3: A diagram showing the concept for the full system with the central sensor head and additional sub-systems.

As well as use in gravity surveying applications, a portable atom interferometer could

Table 1.4: A breakdown of the size, weight and power (SWaP) budget for the sensor and how the sub-systems contribute to this.

	Size	Weight	Power
Total Budgeted	<88 L	<20 kg	<100 W
Total Used	36.1 L*	17.6 kg	97 W
Sensor Head	14.1 L	7 kg	-
Laser Box	8.0 L	4.5 kg	30 W
RF Box	8.0 L	4.4 kg	67 W
Lock Box	2.4 L	1.3 kg	-
Power Supply	1.1 L	0.2 kg	-
Control Computer	2.5 L	0.2 kg	-

* Sum of volume of modules, packaged together they fit in 88 L with some spare space.

open many other potential use-cases. There is firstly the demonstration of the technologies involved at a much lower SWaP. This could lead to other quantum technologies being able to be more portable and robust. Of particular interest in this regard is the laser sub-system. The developed laser, in a uniquely small package, has common functionality to many experiments involving ^{87}Rb. The small, agile laser (discussed in chapter 4.6) Could be adopted into other experiments or systems aimed at portability.

A portable accelerometer with the precision afforded by atom interferometry could have an exciting use-case in inertial navigation and map-matching, being used on ships and submarines for way-finding when GPS is unavailable. Overall, the future of gravimetry and portable accelerometers looks to be in developing sensor arrays. This would probably be relative accelerometers disciplined by an absolute atom interferometer. The demonstration of a portable, robust and sensitive instrument will significantly progress the adoption of quantum technologies and the field of sub-surface mapping.

The thesis is organised into six chapters. This first chapter pertains to the current state of the field and the motivations for the work presented. The second chapter presents the atomic physics techniques used in the development of the instrument and how gravity measurements are produced. The design and construction of the sensor head is then presented, followed by a chapter on the compact laser system. Finally, the main results of the sensor as an atom interferometer are presented and the outlook of future work.

Chapter Two

Atomic Physics

2.1 Introduction

In this chapter the physical principles underpinning the work of this thesis will be discussed. While the content described in this chapter is well established in previous work by others, the understanding of this work is crucial as it heavily informs the choices made in the design and execution of our work.

The field of cold atoms is relatively young, the first experiments being performed in the 1970's [48, 49]. The Nobel prize in Physics was awarded in 1997 for work on atom cooling [50, 51, 52]. Initial papers showing the use of cold atoms as a test mass for inertial sensing were published in 1991 [11]. Since then much exciting work has been conducted in developing techniques to use atom clouds for atom interferometry. Methods for making atom clouds colder have been developed as well as those to more efficiently control the internal and external state of the atoms. Many interesting techniques involve coupling an internal quantum state to a macroscopic momentum state.

One of the most interesting elements of this field is that it sits in a confluence of classical and quantum descriptions. On the one hand the macroscopic motion of an atom is easily described by the equations of motion and traditional thermodynamics. On the other, the internal state of the atoms can be described by quantum mechanics. Descriptions of the processes involved run the gamut of classical to quantum physics.

In the next section the key processes relevant to the rest of the work of this thesis will be described. This is referred to as a cold atom *toolbox*. There are several techniques that have become fairly standard in these types of experiments, these will be viewed as tools that can be used to achieve a certain affect in an experiment. Through careful and inventive combinations of these tools, the manipulation of atoms and the design of interesting experiments is achieved. The descriptions presented here are by no means exhaustive, they are just intended to give a picture of the processes to understand their application.

In the final sections of this chapter the process of how atom interferometry can be used to measure gravity is presented. A description of the physical processes involved will be given. This is the *path-integral approach*, a semi-classical description. Another description, the *Bloch sphere approach* (a diagrammatic quantum picture) is presented in appendix A. With regards to these, it can be useful to draw attention to the adage of George Box that *"All models are wrong, but some are useful"*.

2.2 Cold Atom Toolbox

2.2.1 Magneto-Optical Trap

The workhorse of most cold atom experiments is the magneto-optical trap (MOT). This offers a way of simultaneously cooling and trapping a cloud of atoms. The cooling refers

to reducing the spread of velocities in the ensemble to millimetres per second. This cooling is provided by a light force through the process of *Doppler cooling*. The trapping aspect is provided by the combination of this light force and a lifting of the magnetic degeneracy of the atoms internal state.

Doppler Cooling

The first element of the MOT is Doppler cooling of atoms. This is provided by opposing light beams red-detuned from a transition. It can be understood by examining the case of a simple two-level atom. The atom is initially in the ground state, it can be excited by stimulated absorption from a laser. The atom will either decay to the ground state via stimulated or spontaneous emission. In the case of stimulated emission the net momentum change is zero, this process can be discounted from this simple consideration. With spontaneous emission the emitted photon could be in any direction. Over many processes, the emission will be isotropic and the atom will exhibit a random walk. An absorption and spontaneous emission will result in a momentum change. Averaging over many of these processes the net momentum will be in the direction of the incident laser. In this way, force can be applied to an ensemble of atoms.

To *cool* the atoms the light force needs to oppose the atoms motion. The detuning of the laser below the transition imposes this friction force. Figure 2.1 presents the cases for the atom interacting with a detuned laser. If the atom is stationary with respect to the laser source (panel a), the atom will observe a red-detuned laser. The atom will scatter some photons from this beam but at a lower efficiency than if on resonance. If the atom is moving towards the laser source (panel b), the atom will observe the frequency of the laser shifted closer to resonance due to the Doppler effect. This atom will scatter more photons from the beam. Similarly, if the atom moves away from the source (panel c) the atom observes

the laser shifted further from resonance and so will scatter fewer photons. Atoms moving towards the beam scatter the most photons, hence the beam opposes motion towards it.

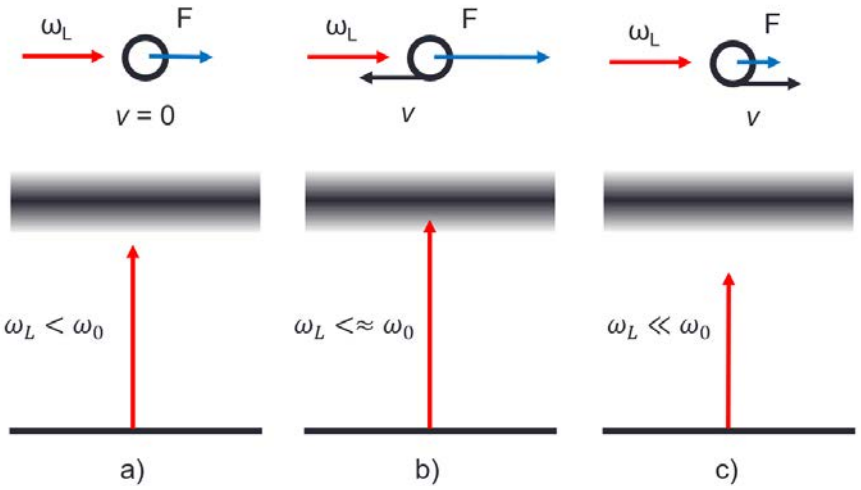

Figure 2.1: Representations of the dynamics of a moving atom and a red-detuned laser beam. ω_0 is the resonant frequency, ω_L is the laser frequency observed by the atom, v is the atom velocity direction and F is the resultant force direction. **a)** The case of a stationary atom. **b)** An atom moving towards the source observes the frequency shifted closer to resonance. **c)** An atom moving away from the source observes the source as frequency shifted away from resonance.

By extending this process by the inclusion of a second, counter-propagating, beam the cooling mechanism can be observed. Both beams are red-detuned from resonance. If the atom moves towards the left beam, it will observe the left beam frequency shifted closer to resonance and the right beam shifted away from resonance. The atom moving to the left will scatter more photons from the left beam so will feel a resultant force to the right. This is the opposite for an atom moving to the right. Whichever way the atom moves in this dimension, its motion will be opposed due to the net difference in photon scattering. This friction force can be formulated as [53]

$$F_L = \frac{\hbar k \Gamma}{2} \frac{s}{1 + s + 4(\frac{\delta - kv}{\Gamma})^2} \ ,$$
$$F_R = \frac{\hbar k \Gamma}{2} \frac{s}{1 + s + 4(\frac{\delta + kv}{\Gamma})^2} \ ,$$
$$F_{total} = F_L + F_R \ , \tag{2.1}$$

where F_L, F_R and F_{total} refer to the force from the left beam, right beam and total force respectively. $\hbar$ is the reduced Plank constant, Γ the natural linewidth, k the wave-vector, δ the detuning from resonance and v the velocity of the atom. s is the saturation parameter, given by the the ratio of the intensity of light, I, and the saturation intensity, $I_{sat} = \pi hc\Gamma/3\lambda^3$. The main form of this force comes from the steady state population in the excited state including a velocity-dependant Doppler term. The relation of the force with the atom velocity is plotted in figure 2.2.

The lowest temperature possible using Doppler cooling is referred to as the Doppler limit. As the cooling mechanism relies on many scattering events, each atom undergoes a random walk. This random process introduces a heating effect given high numbers of scattering events (low detuning) [53, 54]. As the detuning increases, the Doppler beams cool less effectively (though addressing a larger velocity class of atoms). This can be seen in diagram 2.2, the force peaks shift outwards giving a lower gradient which indicates the cooling power. The temperature of the Doppler cooling process is

$$T = \frac{\hbar \Gamma}{4k_B} \frac{1 + (2\delta/\Gamma)^2}{-2\delta/\Gamma} \ , \tag{2.2}$$

where T is the temperature and k_B the Maxwell-Boltzmann constant. This equation is plotted in figure 2.3. This function is minimised when $\delta = -\Gamma/2$. Substituting this into the expression the Doppler limit is given by

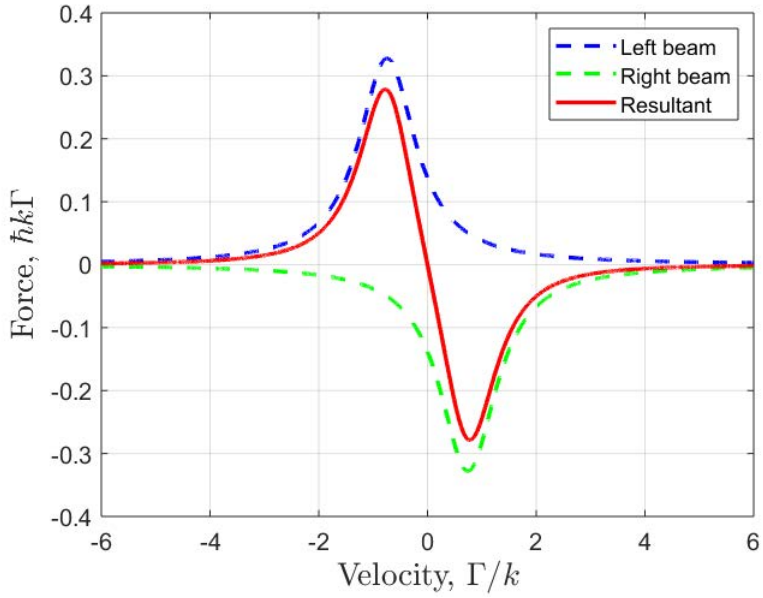

Figure 2.2: A plot of the force-velocity relation given in equation 2.1. The contribution from left and right beams as well as their sum is given. This is calculated for saturation parameter $s = 2$ and detuning $\delta = -\Gamma$.

$$T_D = \frac{\hbar\Gamma}{2k_B} \ , \tag{2.3}$$

which for the rubidium 87 D_2 transition gives $T_D = 145.57\ \mu K$.

Trapping Force

The above process of Doppler cooling only provides cooling, but does not provide a trapping force. To create an ensemble of atom test masses a trapping force is also required, this allows the atoms to be localised in the centre of atom interferometry beams. This trapping force is imposed by driving transitions to a state where the magnetic degeneracy is lifted. By ensuring this magnetic lifting has an appropriate spatial dependence, a trapping force can

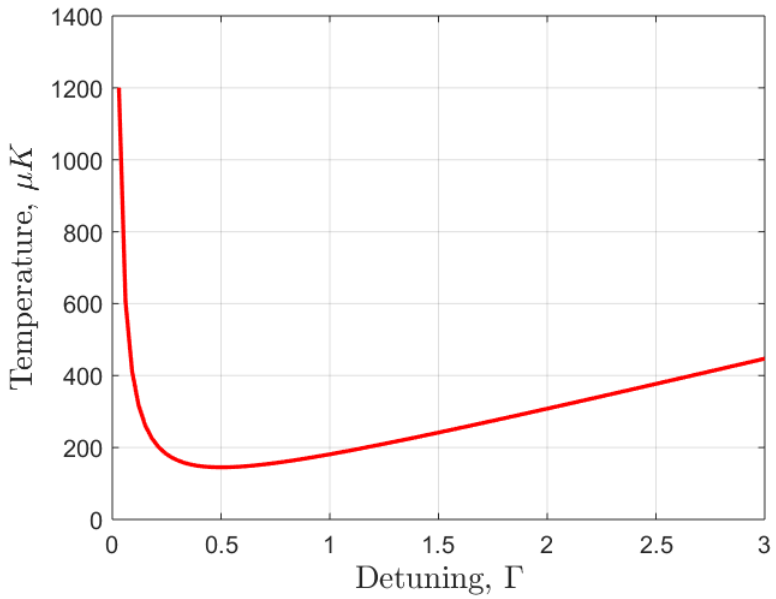

Figure 2.3: A plot of the temperature dependence of the Doppler cooling process on the detuning of the lasers. The detuning is plotted in units of the natural linewidth of the transition.

be included in the light force. The combination of the trapping and cooling forces using lasers and magnetic degeneracy is referred to as the magneto-optical trap (MOT).

The lifting of the magnetic degeneracy is achieved through the Zeeman shift. In the low field limit, where higher order terms are neglected, the anomalous Zeeman effect has the form

$$\Delta E = g\mu_B m_J B_x \ , \tag{2.4}$$

where ΔE is the shift in energy level, g is the Landé-g factor, μ_B the Bohr magneton, m_J indexes the magnetic sub-levels and B_x is the magnetic field strength. At low magnetic field strength this magnetic splitting is linear.

Here, a simple two level model with an excited state having $J = 1$ and ground state having $J = 0$ is considered. The excited state has a magnetic degeneracy giving three sub-levels, $m_J = -1, 0, +1$. The energy levels will only be shifted for the levels $m_J = \pm 1$. The ground state in the cooling transition has $J = 0$ so will not experience perturbation due to this effect [55].

The final piece of this trapping mechanism is that the laser beams are circularly polarised. Circularly polarised light will stimulate transitions where the total orbital angular momentum (L) is changed, such as those between ground state $J_g = 0, m_J = 0$ and excited state $J_g = 0, m_J = \pm 1$. Namely, a σ^- laser will drive transitions to the $m_J = -1$ sub-level and a σ^+ laser will drive transitions to the $m_J = +1$ sub-level.

The above effects can be utilised, along with Doppler cooling, to describe the full MOT mechanism. Firstly, a linearly increasing magnetic field (crossing zero in the trap centre) is used to perturb the $m_J = \pm 1$ sub-levels of the excited state. The $m_J = +1$ level will become increasingly lower than the unperturbed $m_J = 0$ level on the side where the magnetic field is negative, correspondingly the $m_J = -1$ will become increasingly greater. The effect is reversed on the side where the magnetic field is positive. This effect is depicted in figure 2.4.

The polarisation of the Doppler cooling beams are selected so that a σ^+ beam is incident from the side where the $m_J = +1$ level is shifted lower. A σ^- beam is incident from the other side. At a given velocity, an atom further to the σ^+ side (left, in figure 2.4) will absorb more photons from the σ^+ beam than the σ^-. This is because the Zeeman shift has pulled the $m_J = +1$ level closer to the frequency level of the red-detuned beams. The $\sigma^+, m_J = +1$ transition is closer to resonance than the $\sigma^-, m_J = -1$. This adds a spatial dependence to the detuning. The further from the trap centre, the stronger the restoring force will be. This of course extends to atoms on either side of the potential.

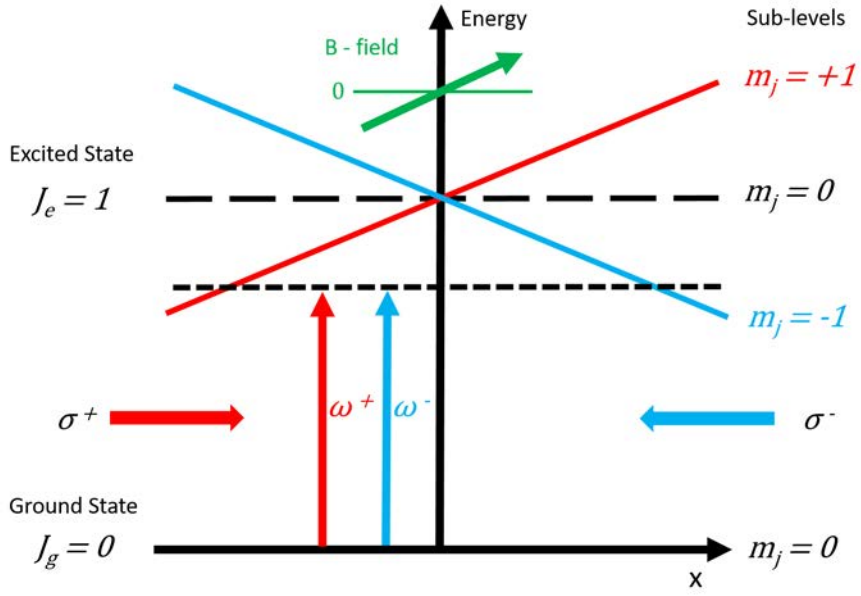

Figure 2.4: A diagram showing the perturbation of magnetic sub-levels due to a magnetic field and how this can be combined with selectively circular polarised, red-detuned lasers to create a magneto-optical trap.

So far the description of the MOT has only considered a single dimension. To create a trap in all three dimensions, three orthogonal pairs of counter-propagating beams can be used. What is important is that in any direction in space an atom moves, there is a restoring force and velocity dependent force. The three orthogonal dimension geometry is the most straight forward and often used. The magnetic field required is referred to as a spherical quadrupole field. This is typically created by a pair of coils arranged to produce a linear gradient. This geometry is represented in figure 2.5.

Rubidium 87

The specific energy level used for cooling rubidium 87 is the D_2 line, shown in figure 2.6. The main cooling cycling transition is between the $F = 2$ ground state and $F = 3$ excited

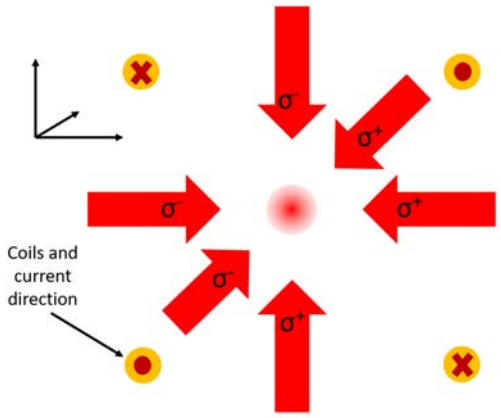

Figure 2.5: A diagram showing the geometry of a MOT using six independent beams.

state. The cooling light has a finite chance to drive transitions to the excited state $F = 2$. These can decay into the $F = 1$ ground state. A *repump* laser is used to pump these atoms back into the cooling cycle.

Optical Pumping

Optical pumping can be used to drive an atom into a particular state, which is "dark" to the applied frequencies. This can be achieved by utilising polarisation to drive an atom into a particular magnetic sub-level. However, in this thesis, optical pumping is performed by allowing decay from an excited state into a hyper fine ground state. Particularly, with the repump turned off, atoms can decay from the ${}^2P_{3/2}$, $F = 2$ state into the ${}^2S_{1/2}$, $F = 1$ state without being driven back into the cooling cycle. Over many cycles, all atoms will be driven into this "dark" state.

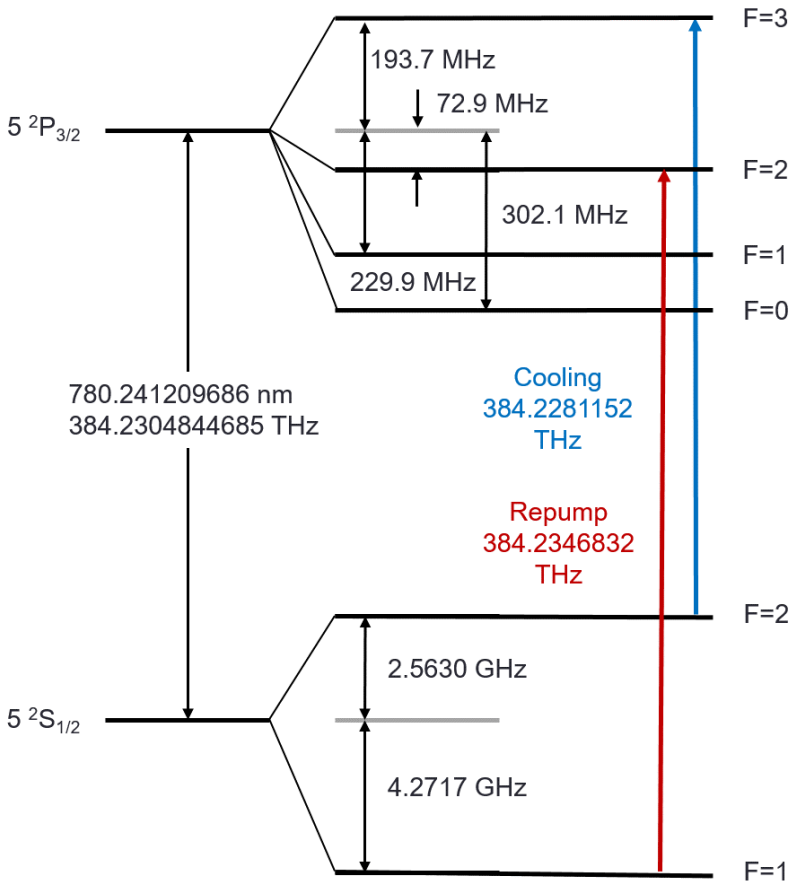

Figure 2.6: Level diagram for the rubidium 87 D_2 line [55].

Prism MOT

For compact systems, a MOT is often created using a single beam and reflections from prisms [56]. The main benefit is in saving space as only one collimator is required. The handedness of circularly polarised light changes upon reflection. Assuming an initially right-handed input beam, the four reflected beams will be left-handed but opposing in direction within each pair. With the addition of a quarter-wave plate, the beam reflected from the bottom mirror is the same handedness as the input beam but in opposite direction. Whether the beams drive σ^- or σ^+ transitions depends on their relation to a magnetic field. The quadrupole must be oriented so that the field is pointing the same way for all the horizontal beams. The

correct polarisations are automatically maintained for the four beams which are reflected by 90°. The geometry can be seen in figure 2.7.

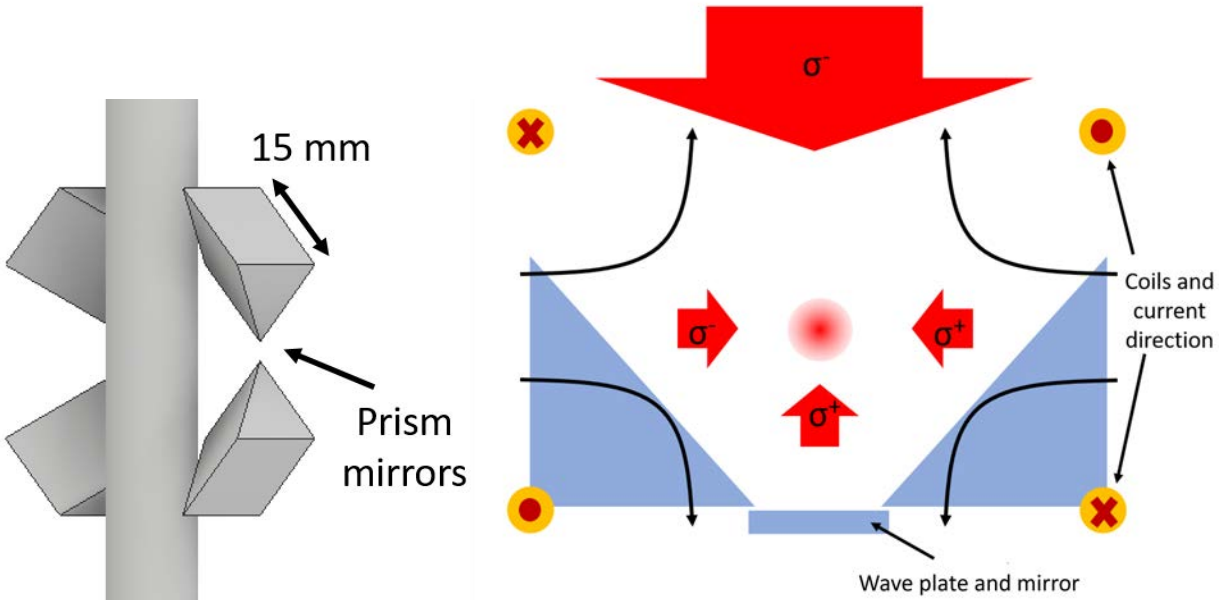

(a) 3D CAD model showing the geometry of the prisms.

(b) A cut-through of prisms, showing reflections of the cooling beams in two dimensions and magnetic field directions.

Figure 2.7: Diagrams showing the geometry of the prism MOT, where the angled edge of the prisms are metallic mirrors.

2.2.2 Sub-Doppler Cooling

Although Doppler cooling is a well developed technique, colder temperatures are required for atom interferometry experiments. As an atom cloud expands, atoms across the ensemble will observe different intensities of a probing Gaussian beam. This can lead to uncertainties. Also, there will be some uncertainty in the position of individual atoms and Doppler broadening due to the velocity spread. For experiments such as the one described in this work, an ensemble temperature of less than 10 μK is desired. To achieve this sub-Doppler cooling is used, also referred to as optical molasses.

With orthogonal, circularly polarised light, the mechanism for sub-Doppler cooling is referred to as polarisation gradient cooling. The resulting optical field of counter-propagating σ^+/σ^- beams is linearly polarised and has a constant magnitude [53]. The direction of the resultant linear field rotates through 2π over an optical wavelength. This process is already present during the magneto-optical trap.

Here, a Zeeman-degenerate ground state is considered where the $J_g = 1$ manifold devolves into $m_g = -1, 0, +1$. For atoms at rest in the above light field, optical pumping will be preferentially distributed in the $m_g = 0$ sub-level. A moving atom will experience a rotation of the quantisation axis of the light field and will be optically pumped correspondingly. Atoms travelling toward the σ^+ beam will preferentially populate the $m_g = +1$ state, and vice versa. Atoms in the $m_g = +1$ state scatter σ^+ light six times more effectively (depending on Clebsch-Gordon coefficients) than σ^- and will remain in the $m_g = +1$ state after scattering [53]. Therefore atoms moving towards the σ^+ beam scatter more light from it and experience a large momentum change to oppose their motion.

Unlike Doppler cooling, the mechanism is not caused by the difference in Doppler shift of the two beams. Instead it is the imbalance in the population caused by the atoms orientation with respect to the light field. For Doppler cooling the friction force is proportional to the power but the capture velocity is independent of power. Conversely in polarisation gradient cooling the friction force is independent of power but the capture velocity is proportional to power [54]. Another limit of cooling via photon scattering is known as the *recoil limit*. This corresponds to the momentum uncertainty associated with a single scattering event,

$$T_R = \frac{(\hbar k)^2}{2Mk_B} \, , \tag{2.5}$$

where T_R is the recoil temperature, k the wave-vector and M the mass of the atom. For the

rubidium 87 D_2 transition this gives $T_R = 0.3\ \mu K$.

2.2.3 Raman Transitions

A key element for performing atom interferometry experiments is the ability to precisely control the atoms internal and external states. Of particular interest are techniques which allow the control we can exert on the internal state with electromagnetic fields to be coupled to the external state of the atom. Transitions between stable ground states offer just such control. Using lasers and magnetic fields, the population inhabiting particular ground states can be controlled and mapped to external momentum states.

In this section the processes used to coherently transfer atomic populations between ground states will be presented. For alkali atoms, a transition with two ground states is often used as these states will have long life times so spontaneous emission between pulses can be ignored. A description for a single photon transition will be given first, then later the more popular technique for inertial sensing: *Raman transitions*, a two-photon transition. The derivations loosely follow [57].

Single Photon Transition

The single photon transition between the two ground states (for the rubidium 87 D_2 line) is in the microwave frequency range ($\sim$6.8 GHz).

The dynamics of the single photon transition can be formulated by considering the Hamiltonian for a two-level atom (states $|1\rangle$, $|2\rangle$) coupled to an electromagnetic field [51],

$$\hat{H} = \hat{H}_A + \hat{H}_{int} \ , \tag{2.6}$$

where $\hat{H}_A$ is the Hamiltonian for the atom (eigenenergies $E_n - \hbar\omega_n$),

$$\hat{H}_A = \hbar\omega_2 \left|2\right\rangle \left\langle 2\right| + \hbar\omega_1 \left|1\right\rangle \left\langle 1\right| \ . \tag{2.7}$$

and $\hat{H}_{int}$ is the Hamiltonian of the atom interaction with the light field,

$$\hat{H}_{int} = -\boldsymbol{d} \cdot \boldsymbol{E} \ , \tag{2.8}$$

where $\boldsymbol{d}$ is the dipole moment operator of the atom and $\boldsymbol{E}$ is the electric field strength. A level diagram of this is shown in figure 2.8. The time dependant Schrödinger equation is solved to find the population in each state at a given time after the interaction field is turned on. Due to this interaction, the probability of an atom being in either state oscillates at the *Rabi frequency*, Ω_{12}. The Rabi frequency is altered if the light light frequency, ω_L is detuned from the transition frequency, ω_{12},

$$\Omega_{12} = -\frac{\left\langle 2\right| \boldsymbol{d} \cdot \boldsymbol{E} \left|1\right\rangle}{\hbar} \ , \tag{2.9}$$

$$\Omega_\delta = \sqrt{\delta^2 + \Omega_{12}^2} \ , \tag{2.10}$$

where δ is the detuning of the light from the transition frequency $\delta = \omega_{12} - \omega_L$ and Ω_δ is the off-resonance Rabi frequency.

The detuning both affects the ability to reach a pure excited state and the period of oscillation. The population in the excited (P_e) and ground (P_g) states at a given time τ are given as

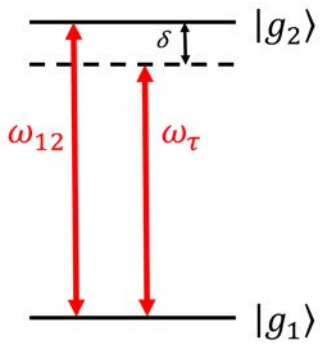

Figure 2.8: Level diagram for the single photon transition for a Rabi oscillation

$$P_e(\tau) = \left(\frac{\Omega_{12}}{\Omega_\delta}\right)^2 \frac{1 - cos(\Omega_\delta \tau)}{2} \ , \tag{2.11}$$

$$P_g(\tau) = \left(\frac{\Omega_{12}}{\Omega_\delta}\right)^2 \frac{1 + cos(\Omega_\delta \tau)}{2} \ . \tag{2.12}$$

Which, with on resonant light, simplify to

$$P_e(\tau) = \frac{1}{2}[1 - cos(\Omega_\delta \tau)] \ , \tag{2.13}$$

$$P_g(\tau) = \frac{1}{2}[1 + cos(\Omega_\delta \tau)] \ . \tag{2.14}$$

The dynamics of equation 2.11, with several values of detuning, are displayed in figure 2.9. It can be interpreted that for a resonant pulse length of $\Omega_\delta \tau = \pi$ the population will invert between the two states. This is referred to as a π pulse. Similarly, a pulse of length $\Omega_\delta \tau = \pi/2$ will create a superposition of both states.

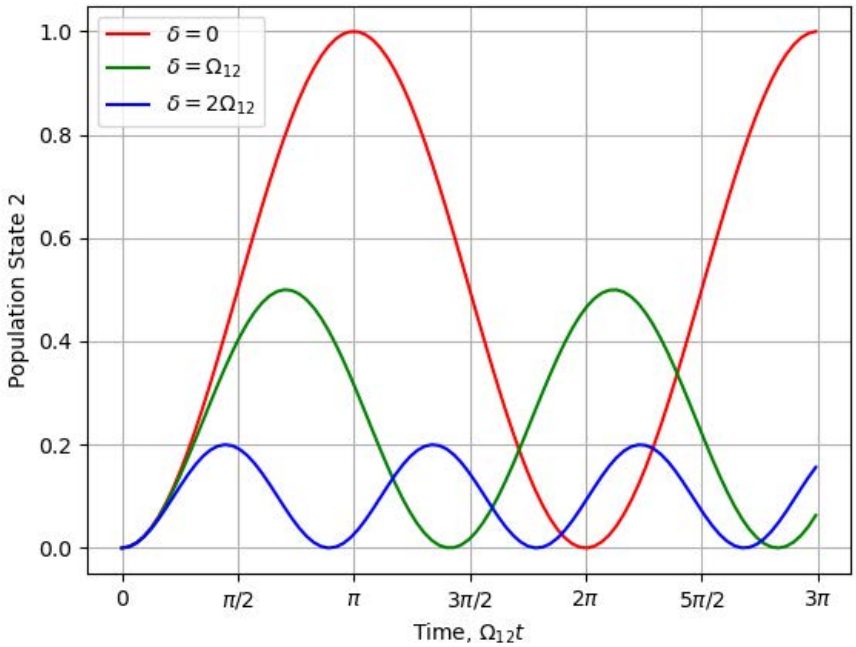

Figure 2.9: A plot of single photon Rabi oscillations with different values of detuning from resonance.

Two Photon Transition

For alkali atoms such as rubidium, a benefit of using a two photon transition is that the frequencies used will be in the optical spectrum (384 THz). Using optical transitions means each photon will transfer significantly more momentum. The photons carry momenta $\hbar k$ which is imparted to the atom when absorbed. When an atom emits a photon via stimulated emission it also changes the atoms momentum by $\hbar k$. The use of lasers also gives incredibly narrow frequency line-widths and directional control. Optical elements such as lenses and wave-plates can be used to finely control all properties of the beam.

To drive the transition between the $^2S_{1/2}$, $F = 1$ and $F = 2$ states using optical frequencies, a two-photon process is used where transitions are between one of the ground

states and a shared intermediate state. This can be seen in figure 2.10. The intermediate is far-detuned to avoid population of the excited states and spontaneous emission. This is an inelastic process commonly called a *Raman transition*.

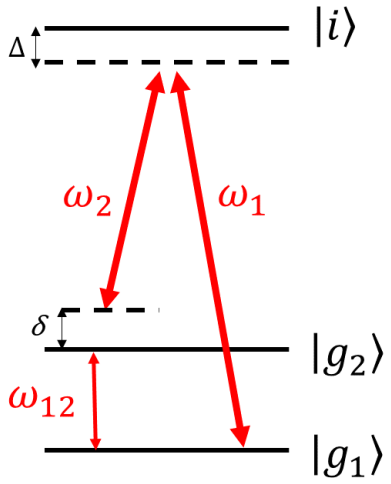

Figure 2.10: A Level diagram for two photon Raman transition.

The single photon equations from section 2.2.3 can be modified for a two photon, three level system. Firstly, the Hamiltonian now becomes

$$\hat{H} = \hat{H}_A + \hat{H}_{int} = \hbar\omega_i \left|i\right\rangle \left\langle i\right| + \hbar\omega_1 \left|1\right\rangle \left\langle 1\right| + \hbar\omega_2 \left|2\right\rangle \left\langle 2\right| - \boldsymbol{d} \cdot \boldsymbol{E} \ , \tag{2.15}$$

and the electric field now has two components,

$$\boldsymbol{E} = \boldsymbol{E}_1 cos(\boldsymbol{k}_1 \cdot \boldsymbol{r} - \omega_1 t + \phi_1) + \boldsymbol{E}_2 cos(\boldsymbol{k}_2 \cdot \boldsymbol{r} - \omega_2 t + \phi_2) \ . \tag{2.16}$$

Similarly, the Rabi frequencies for the individual transitions (Ω_{1i}, Ω_{2i}), the single-photon detuning (δ_{12}), the two-photon detuning (Δ) and the the new *effective* Rabi frequency (Ω_{eff}) can be defined,

$$\Omega_{1i} = -\frac{\langle i|\, \boldsymbol{d}\cdot\boldsymbol{E}\,|1\rangle}{\hbar}\ , \tag{2.17}$$

$$\Omega_{2i} = -\frac{\langle i|\, \boldsymbol{d}\cdot\boldsymbol{E}\,|2\rangle}{\hbar}\ , \tag{2.18}$$

$$\delta_{12} = (\omega_1 - \omega_2) - \omega_{12}\ , \tag{2.19}$$

$$\Omega_{eff} = \frac{\Omega_{2i}^{*}\Omega_{1i}}{2\Delta} e^{i(\phi_1-\phi_2)}\ , \tag{2.20}$$

$$\Omega_{\delta} = \sqrt{\Omega_{eff}^2 + \delta_{12}^2}\ . \tag{2.21}$$

Substituting these new parameters into equation 2.11 the population in the second ground state is found,

$$P_2(\tau) = \left(\frac{\Omega_{eff}}{\Omega_{\delta}}\right)^2 sin^2(\frac{\Omega_{\delta}\tau}{2})\ . \tag{2.22}$$

With this two-photon transition it is also possible to coherently transfer the population between two ground states (π-pulse) and create equal super positions of the states ($\pi/2$-pulse). Converting the electric field magnitude to intensity , $I = \boldsymbol{E}/2$, some dynamics of the Rabi oscillation can be seen,

$$\Omega_{eff} = \frac{\Omega_{2i}^{*}\Omega_{1i}}{2\Delta} = \frac{\Gamma^2\sqrt{I_1 I_2}}{4I_{sat}\Delta}\ , \tag{2.23}$$

where the I_1, I_2, are the Intensities of the respective light fields. It can be seen that increasing the intensity of the Raman lasers will increase the Rabi frequency (More laser power enables shorter pulses). Also, a greater two-photon detuning, Δ reduces the Rabi frequency. It is beneficial to have a large two-photon detuning to avoid population transfer to the excited states, reducing spontaneous emission.

Momentum Transfer

The two-photon process offers an opportunity for the use of two different geometries. Either the photons are incident from the same direction, *co-propagating*, or from opposite directions, *counter-propagating*. The major difference between them for this work is the momentum transferred to the atoms. The impact of this will be detailed in section 2.3 but for now the key point is that a larger momentum will ultimately provide a higher sensitivity for a gravity sensor.

In the co-propagating case both lasers are incident from the same direction. The momentum change to the atom from the absorption and stimulated emission are in opposite directions. The net momentum change on the atom through this Raman process is $\hbar k_{eff} = \hbar(\mathbf{k}_2 - \mathbf{k}_1) = \hbar(k_2 - k_1) \approx 0$. For counter-propagating beams, the momentum change to the atom from absorption and emission are in the same direction. The net momentum change from this Raman transition is $\hbar k_{eff} = \hbar(\mathbf{k}_2 - \mathbf{k}_1) = \hbar(k_2 + k_1) \approx 2\hbar k$.

2.2.4 Bloch Elevator

While the techniques of atom cooling and trapping provide an excellent way of generating an atomic ensemble source and Raman transitions offer a method to couple the internal states to external momentum states, another method can be used to macroscopically affect the location of the ensemble without altering the internal state. This technique is known as the Bloch elevator [58]. This technique has seen particular use in *launching* atomic ensembles to increase free-fall time in a given drop distance [59]. However, there are a wide variety of ways this can be used in cold atom experiments. It allows the efficient manipulation and control of the position and velocity of an atomic ensemble. The internal state is maintained but the ensemble can be moved by many tens of centimetres.

The Bloch elevator is created from many subsequent momentum transfers to the atoms from a *moving lattice*. The moving lattice is formed from counter-propagating laser beams of the same intensity I, detuned by Δ from the single-photon transition with a frequency difference between them. The interference of the two beams creates a periodic potential [59],

$$U(x) = \frac{U_0}{2}(1 + cos(2kx)) \ , \tag{2.24}$$

where $k = 2\pi/\lambda$ is the wave-vector and $U_0 = \frac{2}{3}\hbar\Gamma\frac{I}{I_s}\frac{\Gamma}{\delta}$, with Γ the natural linewidth and I_s the saturation intensity.

In the presence of a constant force F, crucially weak enough to not cause excitation out of this potential, oscillatory motion of the atoms will be induced. The period with which they oscillate in the potential is given by [59]

$$\tau_B = \frac{h}{|F|d} \ , \tag{2.25}$$

where $d = \lambda/2$ is the periodicity of the potential. A constant force can be applied to the standing wave by tuning the frequency between the two lattice lasers at $\Delta\nu(t)$. For a linear frequency difference, the atoms observe an accelerating potential. Hence, atoms bound in the potential experience a constant inertial force,

$$F = -ma = -m\frac{\lambda}{2}\frac{d}{dt}\Delta\nu(t) = -\frac{m}{2k}\frac{d}{dt}\Delta\omega(t) \ , \tag{2.26}$$

where $\Delta\omega/2k$ is the lattice velocity. By creating a linear frequency ramp of one of the beams in a lattice holding an atomic ensemble, the ensemble can be efficiently accelerated. It can be viewed as the atoms being caught in a potential well, but the well itself is moving. This method can be used to launch atom ensembles with over 90% efficiency [60]. Also, by

utilising an accelerator and a mirrored deceleration, an efficient process can be produced which transports atoms to a new location and brings them to rest. These techniques are what constitutes a Bloch *elevator*.

Another view of this process is to consider the particle interactions, similar to the Raman transitions in section 2.2.3. Instead of a two-photon transition between the two ground states, a Bloch elevator transition can be seen as a two-photon transition back to the *same* ground state. Similar to the Raman transition, the counter-propagation of the beams gives a strong directionality to the momentum transfer. At each transfer the atom will receive momentum $\approx 2\hbar k$. The transition can be seen in figure 2.11. The detuning is chosen to be blue shifted to reduce the effect of spontaneous emission.

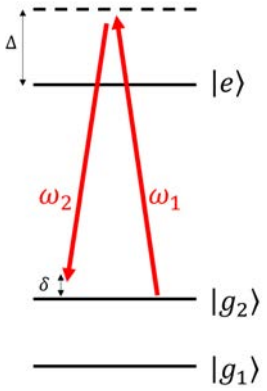

Figure 2.11: A Level diagram for a Bloch elevator transition. The detuning Δ is far from resonance and blue detuned to reduce spontaneous emission compared to red detuning. The single-photon detuning δ is linearly ramped.

The Bloch elevator process starts with atoms at rest. After an interaction with the equal frequency beams the atomic ensemble will have a momentum of $2\hbar k$. The atoms, now travelling with velocity, will observe the beams as off resonance. One of the beams needs to be constantly tuned to compensate the Doppler effect of the increased velocity of the atoms. As the laser beam detuning is changed linearly at rate $\Delta\omega$ the atoms will make transitions,

each increasing their momentum, sequentially. The states and the sequential transitions are displayed on an energy-momenta parabola in figure 2.12. A transition is encountered when the frequency of the detuned laser has changed by

$$\Delta\omega_T = 8E_R/\hbar \ , \tag{2.27}$$

where $E_R = \hbar^2 k^2/2m$ is the recoil energy associated with the transition [61].

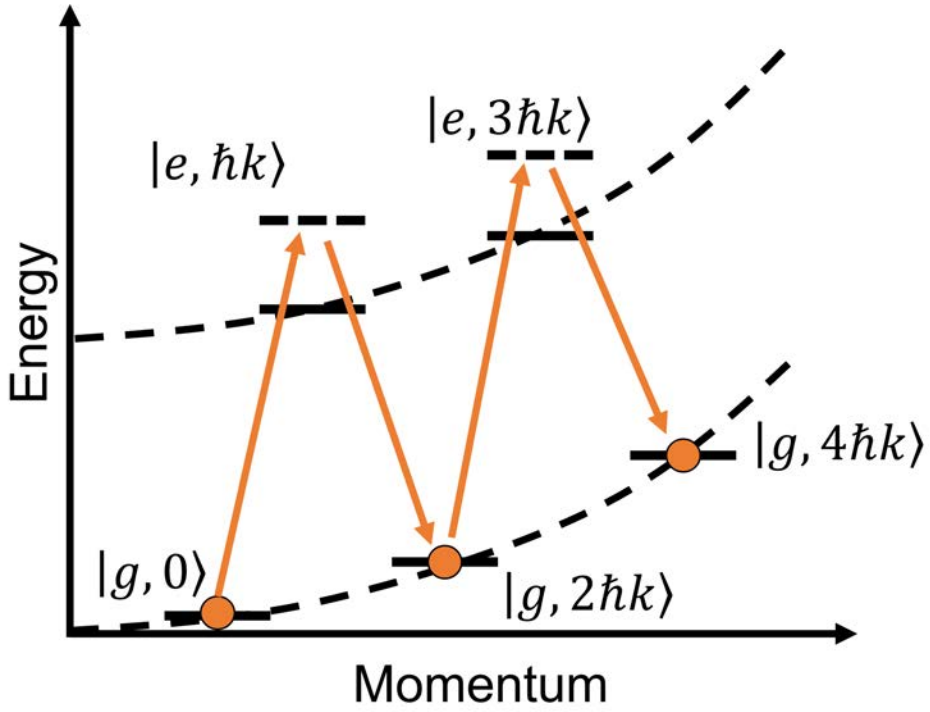

Figure 2.12: A diagram showing sequential Bloch transitions on an energy-momentum parabola. The atoms are transferred through states $|g, 2j\hbar k\rangle\,, j = 0, 1, 2, 3...$ via adiabatic rapid passage. The frequency difference between counter-propagating beams is chirped to remain on resonance with the accelerating atoms.

For a constant frequency change of $\Delta\omega$ with rate $\Delta\dot{\omega}$, the time between transitions is hence

$$t_T = \frac{8E_R}{\hbar\Delta\dot{\omega}} = \frac{4E_R}{\hbar k a} = \frac{2\hbar k}{ma} \ . \tag{2.28}$$

By inspecting equation 2.25 and 2.26 it can be seen that the time between transitions is equal to the Bloch period for an inertial force $ma = m\Delta\dot{\omega}/2k$. Hence the atomic ensemble velocity increases by $2\hbar k/m$ in each Bloch period.

2.3 Atom Interferometry for Gravity Sensing

Atom interferometry is a technique used to precisely measure inertial effects. In simple terms, it can be viewed as a Galilean measurement of gravity. A value of gravitational acceleration can be obtained by measuring the position of an object in free fall at three separate times (see figure 2.13). The acceleration is found as the second derivative of position,

$$z(t) = -1/2gt^2 - vt(t_0) - z(t_0) \ , \tag{2.29}$$

$$\frac{[z(t_3) - z(t_2)] - [z(t_2) - z(t_1)]}{T^2} = -g \ , \tag{2.30}$$

where $z(t)$ denotes the altitude of the test mass at a time t, g is the acceleration due to gravity, $v(t_0)$ and $z(t_0)$ are the initial velocity and position, and T is the time between measurements.

Although in detail very complex, the basic function of atom interferometry is to measure the position of an ensemble of atoms at three separate times and deduce the acceleration from this. The specifics of the process detail how a measurement can be made precisely enough to provide the most sensitive measurements of gravity currently performed [1, 40].

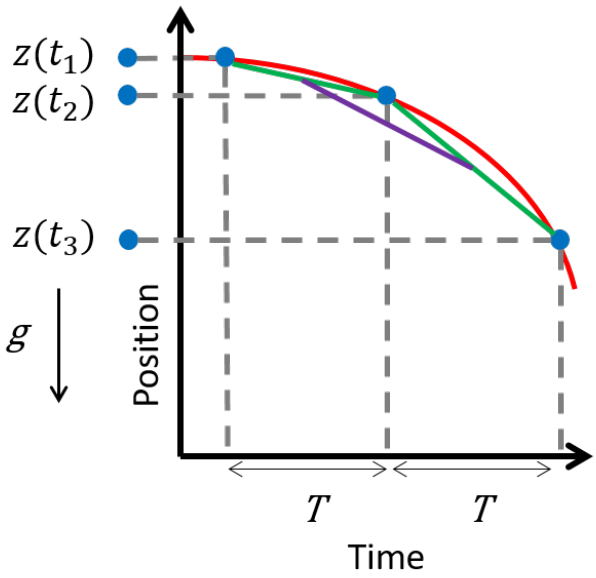

Figure 2.13: A diagram of a Galilean measurement. Gravitational acceleration can be deduced from a position measurement of an object in free fall at three unique times.

2.3.1 Path Integral Approach

The processes involved and dynamics of atom interferometry can be understood by looking at the Feynmann *path integral* formulation, laid out by Storey and Cohen-Tannoudji [62]. In this section some of the insights of this work will be discussed in relation to gravity sensing experiments.

As with a light interferometer, it can be useful to consider the *phase* accumulated along the different interferometer arms. A physical description of the phase through an atom interferometer is given in appendix A, but for now it can be considered that the phase is a quantity which the *observable* state population depends on. The state population is the measured quantity at the output of the interferometer,

$$P_1 = |c_{|1,p\rangle}|^2 = \frac{1}{2}C[1 + cos(\Delta\phi)] \ , \tag{2.31}$$

$$P_2 = |c_{|2,p+\hbar k_{eff}\rangle}|^2 = \frac{1}{2}C[1 - cos(\Delta\phi)] \ , \tag{2.32}$$

where P_1 and P_2 are the populations in state $|g_1\rangle$ and $|g_2\rangle$ respectively, C is the contrast (used to account for non-ideal experiment parameters) and $\Delta\phi$ the phase difference accumulated between the interferometer paths.

The total phase accumulated along an interferometer arm is a sum of the phase contributed from the propagation and the phase accumulated through the atom-light interaction,

$$\phi^{total} = \phi^{prop} + \phi^{laser} \ . \tag{2.33}$$

Propagation

The phase accumulated along a path due to the propagation is found from the evolution of the wave-function of an atom between two points,

$$\Delta\phi_{a\to b} = \frac{S_{cl}(z_b t_b, z_a t_a)}{\hbar} \ , \tag{2.34}$$

where $\Delta\phi_{a\to b}$ is the phase accumulated and S_{cl} is the *classical action* [63, 62] between heights z at times t, given by

$$S_{cl}(z_b t_b, z_a t_a) = \int_{t_a}^{t_b} [L(z, \dot{z})]dt \ . \tag{2.35}$$

$L(z, \dot{z})$ defines the Lagrangian, which solves

$$\frac{d}{dt}\frac{\partial L}{\partial \dot{z}} = \frac{\partial L}{\partial z} \ . \tag{2.36}$$

For a particle in a gravitational field the Lagrangian is given by

$$L(z, \dot{z}) = \frac{1}{2}m\dot{z}^2 - mgz \ , \tag{2.37}$$

which is a sum of the particles kinetic and potential energy where m is the mass of the particle and z its altitude. Calculating the classical action now gives

$$S_{cl}(z_b t_b, z_a t_a) = \frac{m}{2}\frac{(z_b - z_a)^2}{t_b - t_a} - \frac{mg}{2}(z_b - z_a)(t_b - t_a) - \frac{mg^2}{24}(t_b - t_a)^3 \ . \tag{2.38}$$

The paths of the interferometer arms must now be defined. The final solutions will be independent of the starting position, velocity and time so are set as $z_A = 0$, $\dot{z}_A = 0$ and $t_A = 0$. A path which will be referred to as the upper path starts at position A, interacts at vertex C and recombines at point B. The lower path starts at A, interacts at D and recombines at B. The relative positions can be seen in figure 2.14. At any given time t, the altitude of the particle will be

$$z(t) = z_a + \dot{z}_a(t - t_a) - \frac{1}{2}g(t - t_a)^2 \ . \tag{2.39}$$

The positions of the atoms at the vertices of the interferometer can be found by substituting into equation 2.39,

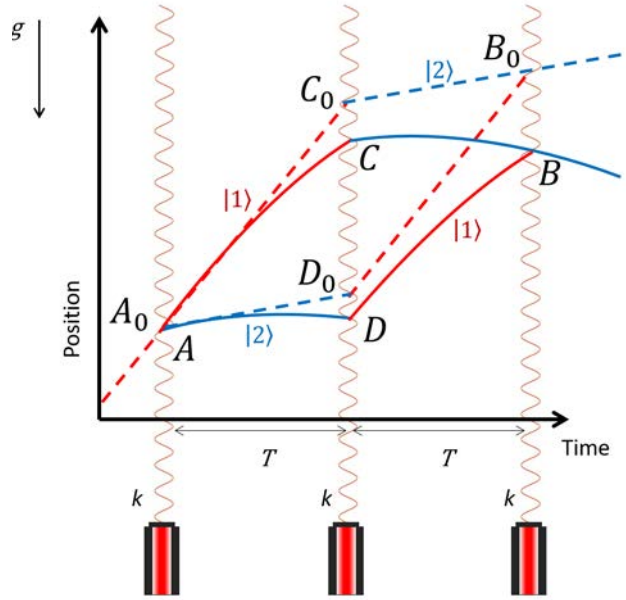

Figure 2.14: A diagram showing the generalised paths of an atom interferometer. The upper path follows ACB and the lower follows ADB. The affect of gravity can be seen as a perturbation on the motion to the idealised paths $A_0C_0B_0$, $A_0D_0B_0$ which form a parallelogram.

$$z_A = 0 \ , \tag{2.40}$$

$$z_C = -\frac{1}{2}gT^2 \ , \tag{2.41}$$

$$z_D = -\frac{1}{2}gT^2 + \frac{\hbar k_{eff}}{m}T \ , \tag{2.42}$$

$$z_B = -2gT^2 + \frac{\hbar k_{eff}}{m}T \ . \tag{2.43}$$

$$\tag{2.44}$$

One of these terms comes from the gravitational acceleration on the particle, the other from the momentum imparted by the Raman pulses ($\dot{z} = p/m$).

Now the difference in phase between the two paths can be calculated by substituting

2.40 into 2.38,

$$\Delta\phi^{prop} = \Delta S_{cl} = [S_{cl}(AC) + S_{cl}(CB)] - [S_{cl}(AD) + S_{cl}(DB)] \tag{2.45}$$

$$= \frac{m}{\hbar T}[z_C^2 - z_D^2 - z_B z_C + z_B z_D] \tag{2.46}$$

$$= 0 \ . \tag{2.47}$$

The propagation of the atom packets around the interferometer does not contribute any phase difference between the arms. This is because the atom packets start and end at the same point, making a closed loop. If the times between pulses were not equal, the packets would not coincide at the final pulse. This would create some phase shift between the arms. Also, as the packets both spend equal time in both internal states, there is no contribution from the internal evolution. Hence, the only contribution to the phase difference is from the laser interaction,

$$\phi^{total} = \phi^{laser} \ . \tag{2.48}$$

Laser Interaction

When an atom interacts with the vertical Raman laser, there are four possible situations that can occur. The atom is treated as a two-level system and the interaction occurs at a single point z_0, t_0. If the atom is initially in state $|g_1, p\rangle$ it could pass through the laser and not change state. It could also transition to state $|g_2, p + \hbar k_{eff}\rangle$. Similarly an atom starting in state $|g_2, p + \hbar k_{eff}\rangle$ could remain in that state or transition to state $|g_1, p\rangle$. The interactions are summarised in figure 2.15. The affect of the interaction is to change the atomic wave-function by one of four multiplying factors,

$$U_{11} \qquad (1 \to 1)\ , \tag{2.49}$$

$$U_{22} \qquad (2 \to 2)\ , \tag{2.50}$$

$$U_{21}e^{i(k_{eff}z_0-\omega_L t_0-\phi)} \qquad (1 \to 2)\ , \tag{2.51}$$

$$U_{12}e^{-i(k_{eff}z_0-\omega_L t_0-\phi)} \qquad (2 \to 1)\ , \tag{2.52}$$

where k_{eff}, ω_L and ϕ represent the effective wave-number, frequency and phase of the laser. U_{ij} denotes the transition amplitude between the jth and ith internal states.

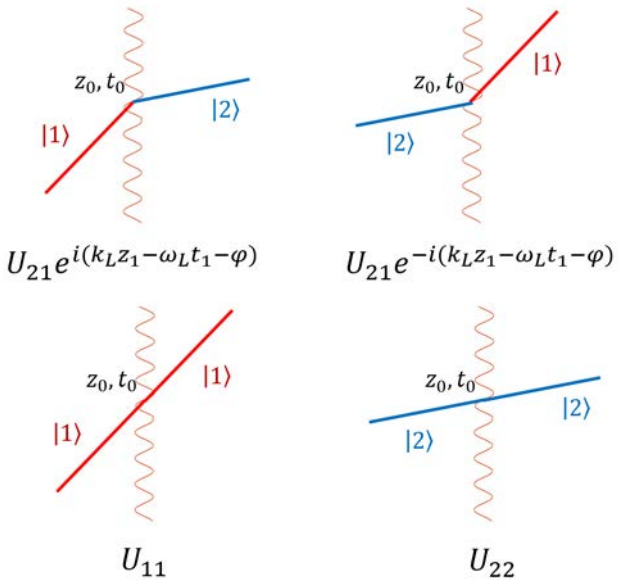

Figure 2.15: A diagram showing the possible interactions of a laser and a two-level atom. The atom can start in state $|1\rangle$ and transition to state $|2\rangle$. This alters the atom wave-function by the accompanying multiplying factor. The reverse process can also happen, with corresponding multiplying factor. The atom can also pass through without interaction.

The contribution of the laser interaction on the phase of the atoms in the interferometer can now be calculated. The sequence calculated will be that shown in figure 2.14. An

atom ensemble is initially in a pure $|1\rangle$ state. Upon interacting with the first $\pi/2$ beam half of these atoms will interact, following path AD. The other half will not interact and follow path AC. After time T a π pulse interacts with both packets, fully transferring the state of all atoms. After another time T, a final $\pi/2$ pulse recombines the atomic packets. The output of this will be a mix of the states (depending on the phase difference accumulated). The output of the ACB arm is chosen to be observed, although the process works for any choice.

For arm ACB there is only one transition occurring, at vertex C. This gives the phase accumulated along this path as

$$\phi^{ACB} = U_{22}U_{21}exp\{i[k(z_{C_0} - \tfrac{1}{2}gT^2) - \omega T - \phi_{II}]\}U_{11} \ , \tag{2.53}$$

where z_{C_0} is the unperturbed position and ϕ_{II} is the laser phase for the second pulse. Similarly, the accumulated phase along path ADB is

$$\phi^{ADB} = U_{21}exp\{i[k(z_{B_0} - 2gT^2) - 2\omega T - \phi_{III}]\}\times \tag{2.54}$$

$$U_{12}exp\{-i[k(z_{D_0} - \tfrac{1}{2}gT^2) - \omega T - \phi_{II}]\}\times \tag{2.55}$$

$$U_{21}exp\{i[kz_{A_0} - \phi_I]\} \ . \tag{2.56}$$

The phase difference accumulated between the two arms can be formulated in a similar way to in equation 2.45. The similar terms are collected and examined together. The multiplying factors U_{ij} are ignored here as they are independent of g and the laser phase,

$$\Delta\phi^{laser} = \phi^{ACB} - \phi^{ADB} \tag{2.57}$$

$$= k(z_{C_0} - z_{B_0} + z_{D_0} - z_{A_0}) \qquad \rightarrow = 0 \tag{2.58}$$

$$+ k(-\tfrac{1}{2}gT^2 + 2gT^2 - \tfrac{1}{2}gT^2) \qquad \rightarrow = kgT^2 \tag{2.59}$$

$$+ (-\omega T + 2\omega T - \omega T) \qquad \rightarrow = 0 \tag{2.60}$$

$$+ (\phi_I - 2\phi_{II} + \phi_{III}) \ , \tag{2.61}$$

giving the final result,

$$\Delta\phi^{laser} = kgT^2 + \phi_I - 2\phi_{II} + \phi_{III} \ , \tag{2.62}$$

which is sensitive to gravity. The first term (2.57), containing the vertex positions unaffected by gravity, sum to zero due to the geometry of the parallelogram. The contributions from the phase of the laser ϕ_i at the interaction points is included as it can be used as a control in experiments.

Some understanding of the process can be gleaned from inspection of where the kgT^2 term arises. A term in kgT^2 is accumulated in both arms from the interaction of the mirror pulse. As the packets experience an opposite momentum change here, the terms do not cancel but add. A further term in kgT^2 is accumulated at the final pulse. This is only present for one arm however, as in only the ADB arm does the state change. For either final state that is measured, only one of the arms interacts with the final pulse.

It is due to the affect of an *acceleration* that the inertial effect can be measured using this sequence. The motion perturbs the position of the atoms relative to the laser *more* for the final pulse. This gives rise to the asymmetry between the arms as only a single arm interacts with the final pulse. However, this sequence is not sensitive to *velocity*. A term

$v_0 T$ could also be included but the contributions to the phase difference would cancel. This is because the affect of the velocity on the position of the atoms is linear in T and not quadratic.

It is the interaction of the lasers with the atom packets that introduces a change in the arms of the interferometer. Particularly, the gravitational acceleration alters the position of the atoms at *state changing* interactions. A choice in which state is observed at the output creates an asymmetry as only one arm will effectively interact with the last pulse.

2.3.2 Measuring Gravity

So far the discussion has been about how an atom interferometer is sensitive to gravity. The act of *measuring* gravity adds some nuance. In a light interferometer, an induced path difference between the arms alters the interference at the output. This is not *measuring* the path difference, however. First, a reference measurement of zero path difference must be taken. Ideally many measurements are then taken at different path differences around this value, this will map out an *interference fringe*. From this fringe the relationship between the interference and phase difference can be fit.

A similar extension must be made to create a gravity *measurement* using an atom interferometer sensitive to gravity. The act of performing a gravity measurement is akin to finding the reference value of zero path difference. It is very difficult to decouple gravity from an atom interferometry measurement; the gravitational acceleration will always create a phase difference between the arms which spans many interference fringes. In order to compensate this, the interaction laser is *chirped* to compensate the Doppler shift due to the free fall. When the chirp rate exactly compensates the gravitational acceleration, there will effectively be zero phase difference between arms.

If a linear chirp α MHz s^{-1} is added to ω_2 (the single photon detuning), its angular frequency will be $\omega_2(t) = \omega_2 + 2\pi\alpha t$. This time dependant factor can be absorbed into the phase contributed by laser interactions. The path difference from equation 2.62 is now

$$\Delta\phi^{laser} = kgT^2 - 2\pi\alpha T^2 + \phi_I - 2\phi_{II} + \phi_{III} \ . \tag{2.63}$$

The state populations can be shown to have the form,

$$P_1 = \frac{1}{2}C\{1 + cos([2\pi\alpha - k_{eff}g]T^2 + \phi_I - 2\phi_{II} + \phi_{III})\} \ , \tag{2.64}$$

$$P_2 = \frac{1}{2}C\{1 - cos([2\pi\alpha - k_{eff}g]T^2 + \phi_I - 2\phi_{II} + \phi_{III})\} \ . \tag{2.65}$$

There exists a value $\alpha_0 = k_{eff}g/2\pi$ which exactly cancels the phase shift due to gravity. This is true for any value of T. There will of course be occurrences where the interference is compensated (once every fringe) but the value α_0 will compensate gravity for any time T. Hence, a measurement of gravity can be made by finding the value α_0 which creates a global compensation. This is shown in figure 2.16.

An extension to measurements of the gravitational acceleration is the use of an interferometer to create gravity maps. With a very sensitive device, minute changes in g can be measured. A sensor can be moved from point to point, measuring g in the above described method. This still involves producing at least three chirp rate scans. In fact, if the chirp rate is selected to not sit at a turning point but rather on the slope of a fringe, measurements between points can be done with only a single shot and observing how the output changes along a slope.

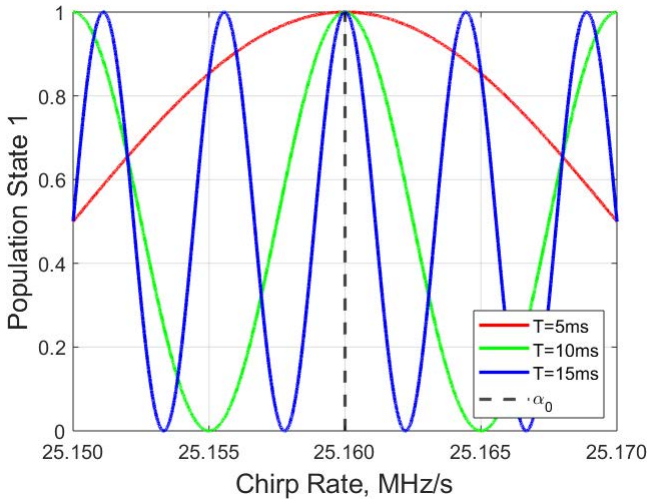

Figure 2.16: A model showing how gravity can be measured from several chirp rate scans with different drop times. At a particular value of the chirp rate, α_0, the phase shift from the gravitational acceleration will be exactly compensated. This is the case independent of the drop time T.

2.4 Summary

Although a relatively young field, cooling and trapping atoms has rapidly become the basis of a very exciting and fruitful field. The variety of tools available to an atomic physicist is ever growing. The well-equipped have many options for controlling both the internal and external parameters of atomic ensembles and with this control, ground-breaking experiments can be designed and built. In the latter sections of the chapter, the physics of atom interferometry and how it can be used to measure gravity was discussed.

Chapter Three

Compact Gravity Sensor

While much work has been put into developing inertial sensors using atom interferometry techniques, the work presented in this thesis aims to produce a sensor which demonstrates a significant reduction in the size, weight and power requirements of such systems. Over recent years there has been significant progress in realising more portable sensors. Most of these focus on large platforms such as trucks [1, 38], planes [35], or ships [36]; though there is interest in sensors for unmanned aerial vehicles citeWeiner. While there is significant potential benefit for the improved sensitivity offered by atomic sensors in these cases, there is also an application for a person portable system. The incumbent gravity sensor used for civil applications is the *Scintrex CG6* [24] which is portable and operable by a single person. The work of this thesis aims to, for the first time, demonstrate atom interferometry in a similar form factor to incumbent technology, linking it to a wider array or applications.

This chapter will outline the work done to design a novel measurement scheme used to perform atom interferometry based gravity gradiometry (section 1.2.3) in a system with unprecedented size and weight. The process for design and realisation of the *sensor head*, including the vacuum chamber and peripherals, is presented. The sensor head is the central

part of the system design. The laser system and driving microwave chain will be presented in chapter 4.

3.1 Design Criteria

To realise a person-portable system, requirements on the size, weight and power consumption must be met. This system is designed to be moved by a single person or an unmanned aerial vehicle (UAV) between measurement points in order to produce a survey of local gravitational acceleration. A useful comparison for volume is a backpack, with the smallest being around 20-30 L and larger expedition packs being in the range of 80-100 L. A volume of 100 L is the limit for the design of this system, with 80 L desireable. For weight, the limit for safe manual handling in a workplace is suggested as 25 kg (the suitcase limit for most airlines is 23 kg). 25 kg will hence be the weight limit, with 20 kg desireable. This includes projected battery operation, from 4 kg's of lithium-polymer battery. The power consumption imposes portability limits in whether the system can be powered from a battery, generator or mains tethered. A designed limit of 150 W is feasible and allows comfortable battery operation for several hours.

As described in section 1.2.3, there are several benefits to using a gravity gradiometer for surveying over a gravimeter. However in gradiometric measurements the signal size is typically smaller, due to subtraction at each gravimeter, and the system design is necessarily more complex. This is especially true when developing an instrument with many novel aspects. There are many application areas of interest for a portable gravity sensor and it would be useful to look at the benefits of gravity and gravity gradiometry measurements in each. Therefore, the system is designed to operate in several gravimetry and gravity gradiometry schemes.

In cold atom experiments, typically the cold atom generation chamber is the largest part of the vacuum chamber in terms of volume, weight and power consumption. These have been significantly reduced by using prism MOT's [64]. In order to have a single cold atom generation site and be able to perform gravity gradiometry measurements, some novelty will have to be used in the design of the physics processes and the physical design. To achieve this a Bloch elevator will be used to manipulate a single cold atom cloud into the two starting positions for a gradiometer. In addition to this atom launching will be used in order to have long interrogation times in a small vertical distance.

Another important aspect for designing a portable experiment is compensating for environmental changes. Particularly for atom interferometry systems using rubidium 87 the external magnetic field has to be controlled, otherwise the Zeeman shift will change the transition frequencies. In lab experiments this is often performed using compensation coils. However, for a portable system, the possibility of magnetic fields changing with spatial position in a survey must be addressed. This could either be achieved using active feedback into the coil system or by passive magnetic shielding. In order to reduce the complexity of the system as much as possible as well as to reduce the power supplies, the system will be designed to use magnetic shields. Although typically weighty, in this work lightweight shields are used.

3.1.1 System Geometry Concept

In order to meet the volume constraint, as well as allow both gravity and gravity gradiometry measurements from a single cold atom generation site, a novel system geometry has been developed. To house all of the necessary sub-systems (lasers, powers supply, control etc.) and maintain a gradiometer baseline which allows for sensitive measurements, the system is conceptualised as a cylinder with a tall sensor head core surrounded by sub-system blocks.

This can be seen in figure 1.3. This cylinder will be ∼460 mm tall and ∼400 mm in diameter.

The sensor head will consist of a cold atom generation zone, slightly above centre. Hollow tubes to allow movement of atom ensembles will extrude vertically above and below this with detection zones at the ends. The distance between the central zone and the lower detection zone will be ∼170 mm. The distance between the central zone and the upper detection zone will be ∼100 mm. These distances will allow for a gradiometer baseline of ∼270 mm with the whole system not exceeding ∼460 mm. The height difference accounts for laser collimators. For both gravimeter and gradiometer sequences, the measurement cycle time will be limited by the initial atom cloud generation. For all sequences described subsequently, a cycle time of 1.5 s is assumed.

3.2 Compact Gravity Sensing Schemes

There are several principles to consider when designing schemes for gravity sensing. Some of these are fundamental to the measurement and some related to the techniques of atom interferometry. When measuring gravity, the sensitivity is highly dependent on the time in free fall (the separation between pulses). If a test mass is dropped, a longer measurement time necessitates a longer instrument. To some extent, this can be overcome by launching the test mass. Much longer measurement times can be achieved in the same space. However, this does increase the complexity of the system.

For a gravimeter the atom shot noise limited sensitivity is found from

$$\Delta g = \frac{1}{\sqrt{N}.k_{eff}.T^2} \ , \tag{3.1}$$

where Δg is the sensitivity to changes in acceleration, N is the atom number participating

in the measurement, k_{eff} the effective wave number and T is the time between interrogation pulses.

A key factor in the sensitivity of a gradiometer is the vertical baseline between the two atom interferometers. When creating a compact gradiometer there is a trade off between length and sensitivity. For a gradiometer the sensitivity is the gravimeter sensitivity divided by the baseline between measurement points. This is shown as

$$\Delta G_{zz} = \frac{1}{\sqrt{N}.k_{eff}.L.T^2} \ , \tag{3.2}$$

where L is the baseline separation. It can be seen in equation 3.2 that while the gradiometer sensitivity scales linearly with the baseline, it scales with the inverse square of the interferometer time. For this reason more emphasis will be put on maximising the interferometer time than increasing the baseline. The interferometer time can be vastly increased by launching the atomic clouds, quadrupling the interferometer time for a given vertical height. Thus, it is possible to achieve a higher sensitivity within the given length constraints by an increased interferometer time via launching.

In this work the tight constraints have motivated the implementation and combination of techniques to create novel sequence schemes. In order to produce a compact sensor which mitigates the loss of sensitivity from being more compact, new measurement sequences have been developed. These are built upon the atomic physics processes described in chapter 2. In the rest of this section, sequences for both gravity and gravity gradient measurements will be presented which meet the size constraints outlined in section 3.1. The most relevant for this is that the design will have only a single cold atom generation zone and the total vertical height cannot exceed 500 mm.

3.2.1 Gravimeter Schemes

The simplest measurement scheme will be to create a cloud and drop it. While in free fall the Kasevich-Chu interferometry sequence [11] is performed, shown in figure 3.1. While useful for developing the sensor and for some laboratory experiments, gravity measurements will not maximise the potential of cold atom devices for rapid gravity surveying. Using the maximum possible drop distance of 170 mm for the total interferometer time and a 1.5 s cycle time, a quantum projection noise limited sensitivity of 66 nm $s^{-2}/\sqrt{Hz}$ when using 10^5 atoms [31] is possible in this scheme (equation 3.2).

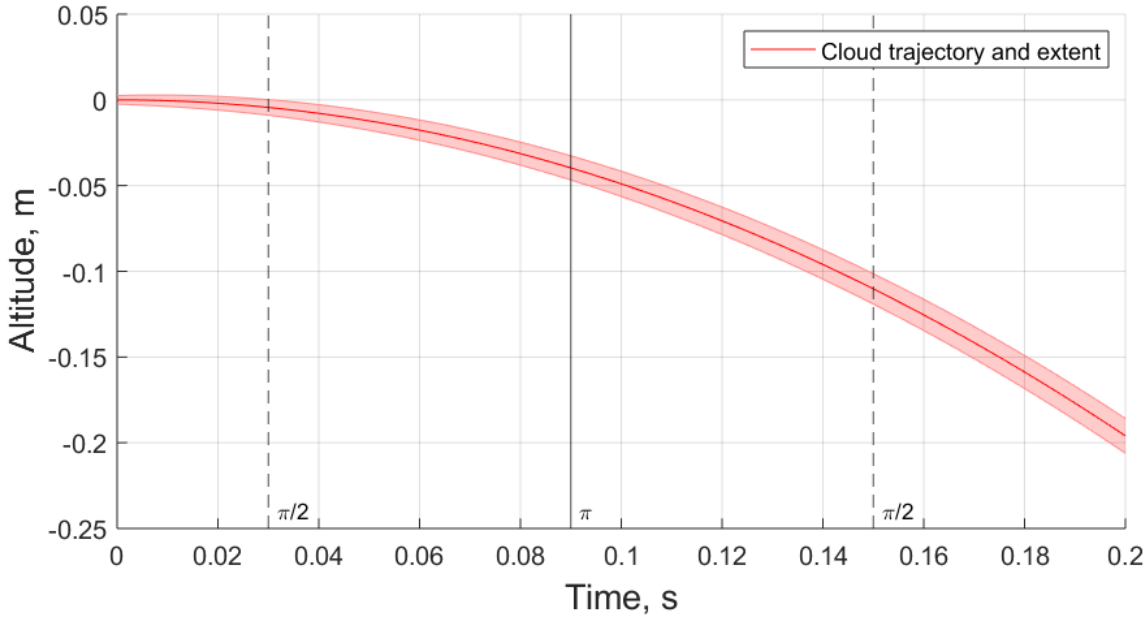

Figure 3.1: A model showing the ballistic path and cloud expansion for a drop gravimeter scheme. The solid red line shows the ballistic trajectory of the cloud and the red area the extent of the cloud assuming a temperature of 20 μK. The dashed and solid lines represent the times of the pulses. The interferometer time, T, is the time between a $\pi/2$ and π pulse, 60 ms.Some time is required at the start for the cloud to develop a velocity and the Raman beams are velocity selective.

An improvement upon the drop gravimeter would be to use a launch gravimeter, as shown in figure 3.2. This will greatly increase the available trajectory and hence the sensitivity (although longer interferometry times can introduce contrast loss). The launching will require an additional atomic physics process. This can either be achieved by a moving molasses where the cooling beams are asymmetrically detuned to produce a resultant force on the atoms or by using a Bloch elevator (section 2.2.4). In general, this potentially doubles the interferometer time for a given vertical height. In this system, the atoms would be launched into a vertical tube, then allowed to fall to the lower detection zone. This is capable of achieving an interferometer time of 120ms and hence a quantum projection noise limited sensitivity of 17 nm $s^{-2}/\sqrt{Hz}$ when using 10^5 atoms. The two gravimeter schemes are summarised in table 3.1.

Table 3.1: Comparison of the projected sensitivity of gravimeters using different schemes given the constraints of this system. A cycle time of 1.5 s is assumed.

Scheme	Atom Number	T Time	Sensitivity
Drop	1×10^5	60 ms	66 nm $s^{-2}/\sqrt{Hz}$
Launch	1×10^5	120 ms	17 nm $s^{-2}/\sqrt{Hz}$

3.2.2 Gravity Gradiometer Schemes

To truly make a useful, portable sensor the capability for gravity gradient measurements is desirable. Traditionally this has been achieved by producing two separate MOT's, separated by a baseline [21]. For this work the size, weight and power required for two atom generation regions is infeasible. Therefore, a scheme for producing two atomic ensembles, separated by a baseline, using only a single cold atom generation site is necessary. Although this has been demonstrated [65], the process must be optimised for small volumes.

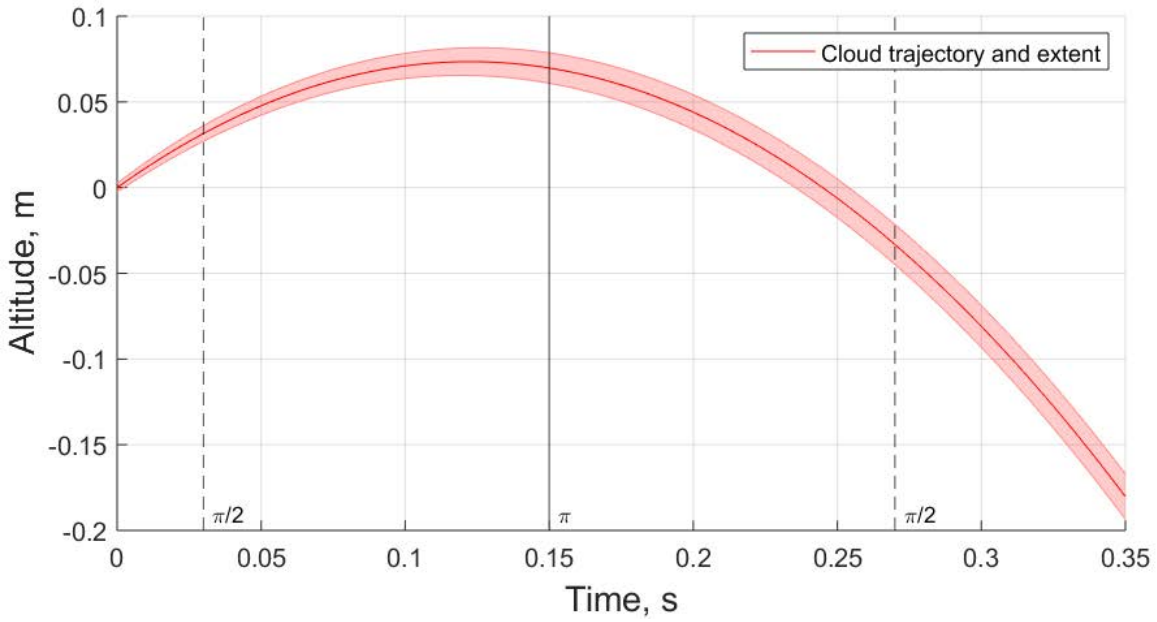

Figure 3.2: A model showing the ballistic path and cloud expansion for a launch gravimeter scheme. The solid red line shows the ballistic trajectory of the cloud and the red area the extent of the cloud assuming a temperature of 20 μK. The dashed and solid lines represent the times of the pulses. The interferometer time, T, is the time between a $\pi/2$ and π pulse, 120 ms.

The simplest way to do this is to drop a first atom cloud and while it is falling generate a second. In this way one can produce two atomic ensembles in free fall separated by a baseline. Two main issues with this method present themselves however. The first is that in a drop configuration the trade-off between vertical space and free-fall time is not optimised. The second is that the second cloud will not have much time to build up a significant atom number. This will drastically affect the statistics of the measurement. An improvement can be made by *juggling* the clouds [66]. This increases the free-fall time significantly, ultimately improving the sensitivity. However, there are still issues with generating a second cloud in the relatively short time the first is in free fall. The scheme is shown in figure 3.3, which allows an atom shot noise limited sensitivity of 2400 10^{-9} $s^{-2}/\sqrt{Hz}$ assuming 10^4 atoms, a

baseline of 0.13 m and a cycle time of 1.5 s.

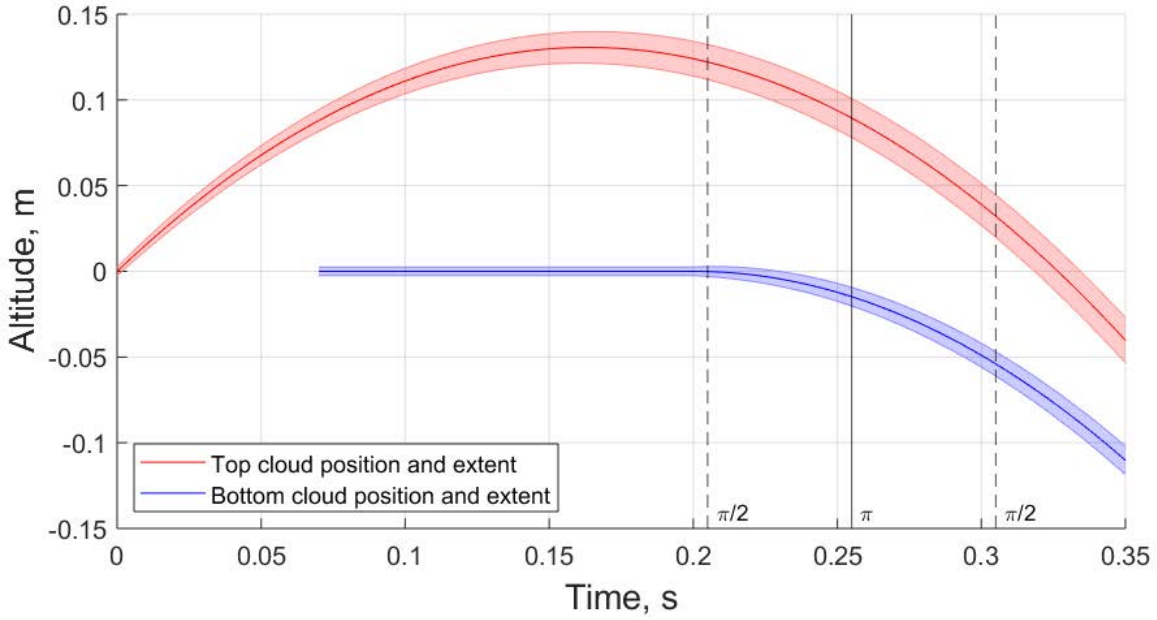

Figure 3.3: A model for the ballistic path and cloud expansion for a scheme enabling a gradiometer measurement from launching a cloud while generating a second. The solid red and blue lines show the ballistic trajectory of the clouds and the respective areas the extent of the cloud assuming a temperature of 20 μK. The dashed and solid lines represent the times of the pulses. The interferometer time, T, is the time between a $\pi/2$ and π pulse, 50 ms.

Another way to produce two clouds separated by a baseline starting from a single cloud is to separate a parent cloud into two child clouds. This can be done by using Bloch oscillations 2.2.4. The basic idea is to use an optical lattice to impart momentum to the parent cloud equally up and down, this will give half the cloud a momentum downwards and half momentum upwards. When the clouds are separated (in both real space and momentum space) the Bloch elevator can be used again to slow down the bottom cloud and give it the same initial velocity as the top cloud, which will set the baseline separation positions. From here the clouds can either be dropped or launched and, while in free-fall, interrogated. This

scheme offers an optimum use of vertical space for the largest baseline possible. The Bloch elevator can also be used to 'catch' a falling cloud of atoms. This can be used to launch a cloud downwards and then a reverse process can be used to catch the cloud, bringing it to rest.

The two daughter clouds will both need to be brought to rest at their desired baseline locations. For the upper cloud, by tuning the launch velocity, the natural resting point of its parabola can be made to coincide with the starting point for interrogation. The lower cloud will need to be caught using a Bloch elevator as it will not naturally come to rest. The catching of the lower cloud will be invisible to the upper cloud as it is momentum selective. This process, along with a drop measurement, is shown in figure 3.4. This allows a gradiometer sensitivity of 1000 10^{-9} $s^{-2}/\sqrt{Hz}$ assuming 5×10^4 atoms.

Splitting the cloud and using a Bloch elevator to position those clouds makes optimum use of the vertical space to create a baseline between two atom clouds. Using the Bloch elevator again to launch these clouds also optimises the height for the interferometer time and hence sensitivity. However, another dynamic of cold atom sensors must also be taken into account for these designs. The atom clouds will have a finite temperature and so over the course of the whole sequence the size of the cloud will ballistically expand (equation 5.3). Firstly, if the size of the cloud expands significantly beyond the width of the interrogation or detection beams, signal from the output of the interferometer will be lost. Similarly, a large cloud size with respect to the beam results in different atoms observing different intensities (and so Rabi frequencies) leading to dephasing. Also, contrast in the interferometer will decrease when atoms observe different intensities of light between pulses as they travel radially. For these reasons it is beneficial to keep the overall sequence time as short as possible. Waiting for the appropriate time for the upper cloud to naturally come to rest could have negative consequences for the signal or contrast of the interferometer.

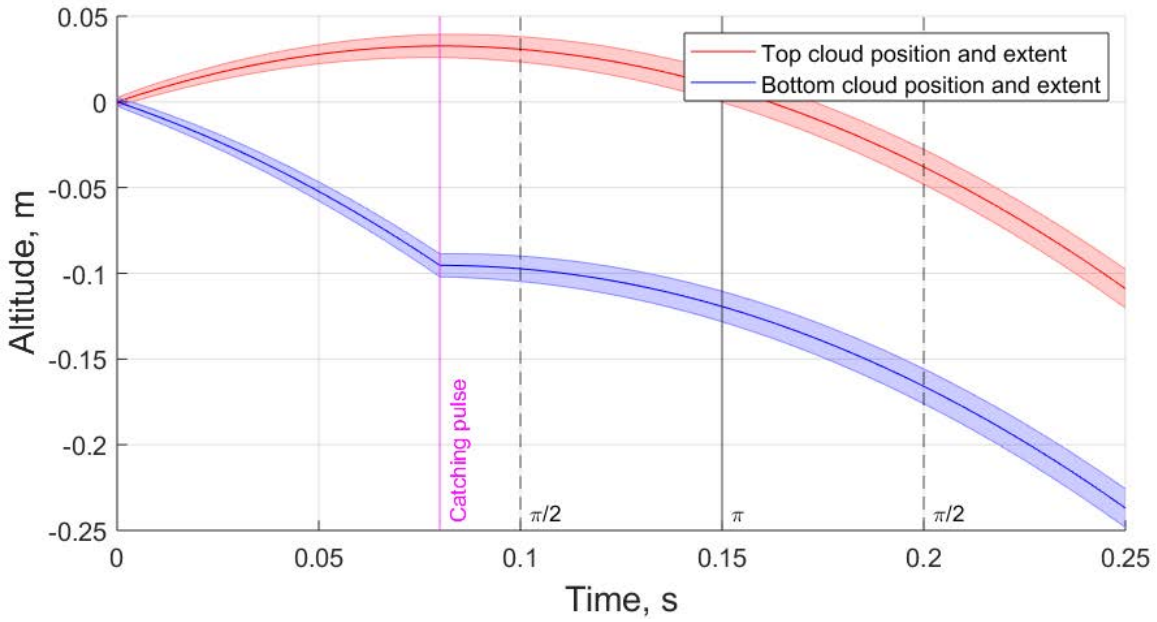

Figure 3.4: A model for the ballistic path and cloud expansion for a scheme enabling a gradiometer measurement from splitting a parent cloud and dropping the daughter clouds. The solid red and blue lines show the ballistic trajectory of the clouds and the respective areas the extent of the cloud assuming a temperature of 20 μK. The dashed and solid lines represent the times of the pulses. The interferometer time, T, is the time between a $\pi/2$ and π pulse, 50 ms.

Another approach is to force the upper cloud into position quicker than a natural parabola would allow. Here, the clouds are split apart at a higher velocity. When the upper cloud is nearly in position it is adiabatically caught to reduce the velocity. The lower cloud then has to be caught. With both clouds are at rest at their baseline separation another Bloch elevator is used to launch them into free-fall. The interferometry pulses are performed, seen in figure 3.5. This overall scheme has been optimised for maximum baseline separation, maximum interferometer time and minimum overall experiment time, allowing a two-fold increase in the gradiometer baseline from 0.13 m to 0.26 m. This enables a sensitivity of 500 10^{-9} $s^{-2}/\sqrt{Hz}$ assuming $5{\times}10^4$ atoms and a 1.5 s cycle time.

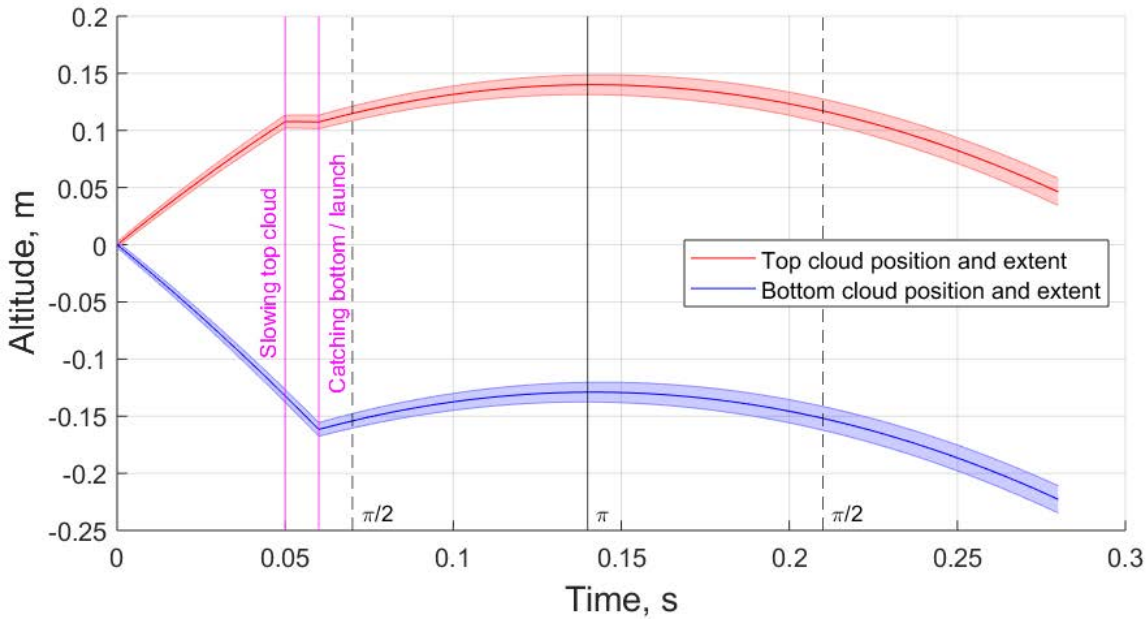

Figure 3.5: A model for the ballistic path and cloud expansion for a scheme enabling a gradiometer measurement from splitting a mother cloud and launching the daughter clouds. The solid red and blue lines show the ballistic trajectory of the clouds and the respective areas the extent of the cloud assuming a temperature of 20 μK. The dashed and solid lines represent the times of the pulses. The interferometer time, T, is the time between a $\pi/2$ and π pulse, 50 ms.

The calculated sensitivity, interferometer time and baseline of the above gradiometer sequences are summarised in table 3.2. Of course, it will be most scientifically interesting and allow for mitigation of risks if the sensor head is capable of performing as many of the above sequences as possible. The design of such a vacuum chamber will be the subject of the following section.

Table 3.2: Comparison of the projected sensitivity of gravity gradiometers using different schemes given the constraints of this system. A cycle time of 1.5 s is assumed.

Scheme	Atom Number	T Time	Baseline	Gradiometer Sensitivity
Launch-Load	1×10^4	50 ms	0.13 m	2400 E/$\sqrt{\text{Hz}}$
Split-Drop	5×10^4	50 ms	0.13 m	1000 E/$\sqrt{\text{Hz}}$
Split-Launch	5×10^4	50 ms	0.26 m	500 E/$\sqrt{\text{Hz}}$

1 E = 10^{-9} s^{-2}

3.3 Vacuum Chamber Design

The aim for this section is to present the design process for the vacuum chamber which will house the experiment. The design of the chamber was an iterative process with the design of the sequence schemes presented in section 3.2, each informing the other. These are all based on a single cold atom generation zone with extensions vertically above and below. The fundamental role of the vacuum chamber is to isolate the atoms from any external environment, namely other background atoms which can remove interrogation atoms from the process. Atoms not taking part in the interrogation sequence can interact with those that are and remove them from the sequence. The more background atoms, the more loss of signal. A desireable level of vacuum to have low loss rates is 10^{-9} mbar, or ultra-high vacuum (UHV).

While the vacuum chamber is the physical housing for the atoms, a vacuum *system* is formed of the chamber and other peripherals which maintain the vacuum. The vacuum peripherals are generally off-the-shelf components which are sealed to the vacuum chamber. The vacuum chamber is monolithically machined from titanium. Titanium has very high strength while remaining relatively lightweight and has good thermal expansion matching

with glass view-ports. For this work, the trade-off between minimising the weight of the system and making that system robust for use as a portable instrument is to be optimised. Any join is going to introduce more risk in the vacuum pressure so as few as possible were used. The use of glass cells was considered as they would be lightweight, however they are inherently less robust a material than titanium and the geometries available would be restrictive.

Again, the MOT region offers a trade-off. This one between the atom number generated in the MOT and the size and weight of the system. There are many processes throughout the sequence where atoms will be lost and it is desireable to have as high a number as possible participating in the measurement to have a high sensitivity. Particularly as the parent MOT is split into two, the potential atom number is at least halved. Increasing the prism size effectively increases the beam size and hence capture volume of the MOT, allowing more atoms to be captured. It also increases the footprint of the MOT region, the necessary size of the input collimator and the laser power required. The beam diameter was chosen to be 2" as this allowed a sufficient cooling intensity for the power projected from the laser system (chapter 4). This sets the diameter of the MOT region to around 2", which sets our prism size to 15 mm base, with a 1" bottom mirror.

As mentioned previously (section 3.1), the vacuum system should be designed to fit inside a cylindrical geometry to accommodate magnetic shields. The cooling beam and interferometry beams are decoupled using different input collimators. The orientation and cleanliness of both beams can be more easily controlled if they use separate collimators. For these reasons, the MOT beam is input from the side of the chamber, but uses a right angle input mirror so the collimator can be inline with the chamber and fit in a cylinder. The crossed prisms should not interfere with the interrogation beam so they are located at 45 degrees to the interrogation axis. The location of these prisms is set to allow a 1/2" (12.7 mm) interrogation beam. This is shown diagrammatically in figure 3.6, matching the

calculated cloud size for a 20 μK cloud after a 200 ms sequence. It is noted that this is a cloud to beam size ratio of one which would cause dephasing.

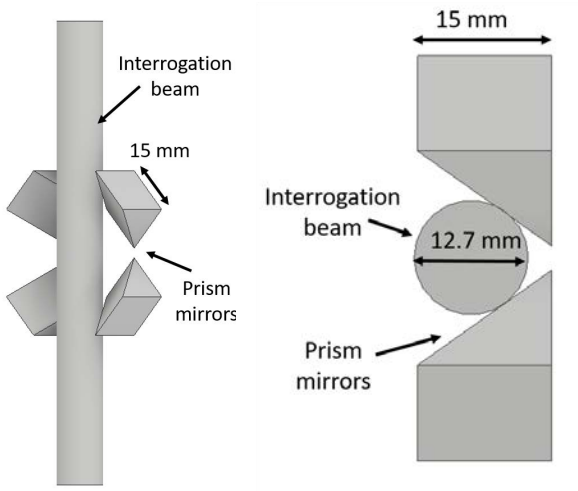

(a) Front view. (b) Top view.

Figure 3.6: A model of how the interrogation beam relates physically to the prisms of the MOT region.

The height of the chamber, particularly the extension above and below the MOT region are set by the modelling of the sequence schemes from section 3.2. The overall height of the system cannot exceed 500 mm. This needs to include the atoms motion, the input windows for the vacuum chamber, a collimator, wave-plate and mirror for the interrogation beams, allowance for the input fibre to bend safely, and finally some outside packaging. To allow for these, the atom motion is set to at maximum occupy 350 mm. The extrusions above and below the MOT chamber are designed to house a sequence of splitting and launching the atoms which occupies this vertical distance. The detection zones are then placed to be able to detect the atoms after a 200 ms free-fall having been launched.

A crucial thing to consider when designing an experiment such as this is the optical access needed. An input window is needed for the cooling beam and windows for the interrogation beams at the top and bottom of the chamber. Some access windows for the

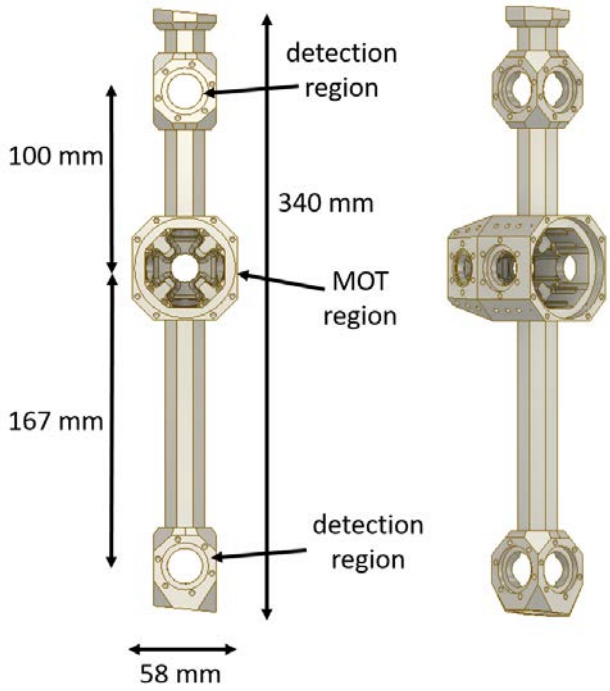

Figure 3.7: A model of the vacuum chamber designed for this work.

detection zones are also necessary, depending on the detection scheme used. Further details are given in section 3.4.2. Additionally, some windows are designed to have access to the MOT region, these are for monitoring MOT atom number, stability and temperature. Two 1" windows for MOT observation. Our design for detection zones allows for optical access through 1" windows on four sides without adding much mass to the system. The windows for interrogation beams are also 1" diameter but are angled at 6 degrees to the vertical in order to prevent any reflection from the surface causing interference. In order to reduce the size and weight, indium sealing of the windows was used rather than flange connections (figure 3.8).

A source of rubidium is required in the vacuum chamber. This is achieved through the use of rubidium dispensers, available from *SAES* [67] and an electrical vacuum feed-through flange. These are thin metal filaments, 35 mm long, which contain rubidium oxide. The

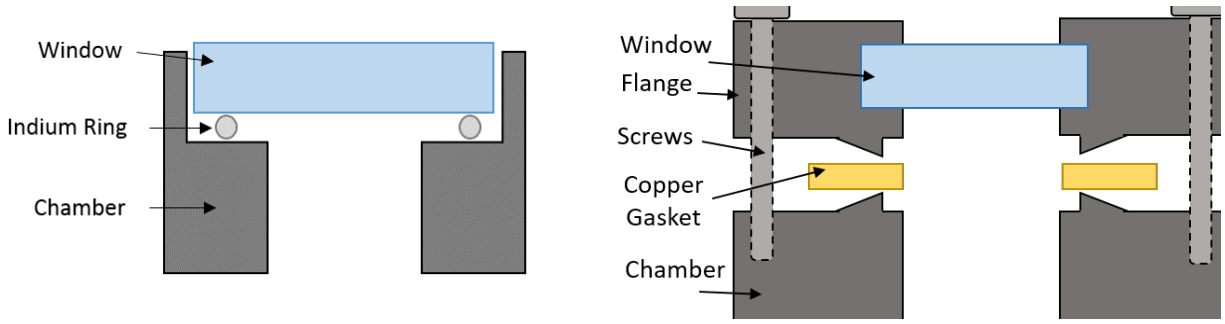

(a) Indium sealed window.

(b) CF flanged window.

Figure 3.8: Diagrams comparing the design and size of Indium sealed windows and ConFlat flanged windows.

filament is heated by passing an electrical current through it, emitting rubidium atoms. From this background vapour atoms are captured in the MOT. This is a very low size, weight and power solution compared to a 2D MOT. A downside to this is that it produces a background of atoms which reduce the lifetime of the atom cloud through collisions. The system is designed to include a microwave antenna, performing microwave (6.8 GHz) transitions for state selection.

The other components which complete the vacuum chamber are those required for the preparation and maintenance of the vacuum. Firstly a valve is needed to connect to a turbo pump used for the initial evacuation of the chamber. This turbo pump will be disconnected after bake-out, but the valve is required to maintain the vacuum and is useful in case the system needs to be reconnected to a pump later on.

An ion pump and a getter are also required to maintain the vacuum. The getter consists of a highly convoluted surface upon which non-ionisable species can be adsorbed [68]. When activated, the getter offers passive pumping so requires no power when in operation. The ion pump is used to remove any ionisable species from the chamber and noble gases not pumped by the getter. It uses a strong magnet to create a long path length for electrons

which scatter with and ionise particles, which are then accelerated by the electric potential to a getter material [69]. As it is highly magnetic it needs to be kept outside of any magnetic shielding. The placement of the vacuum peripherals is shown in figure 3.9. The procedure for the vacuum construction and preparation is given in appendix B.

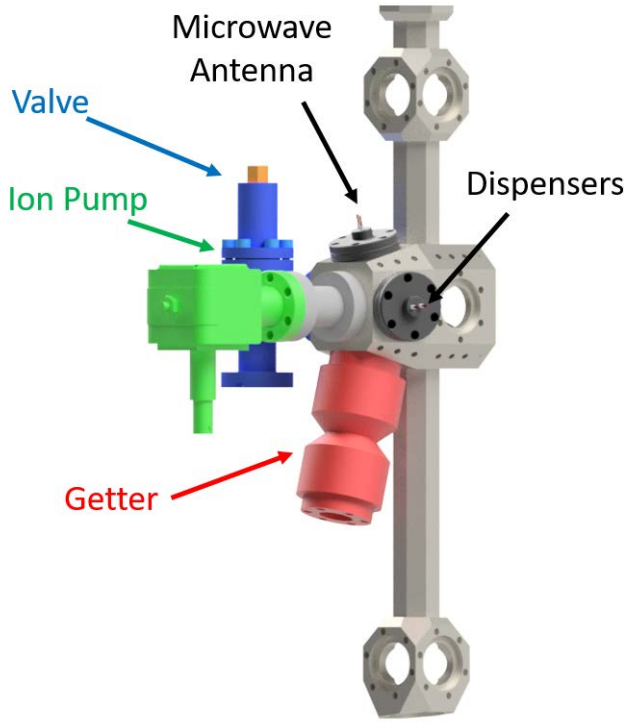

Figure 3.9: A model showing the placement of the different peripherals attached to the vacuum chamber.

3.4 Sensor Head Peripherals

The sensor head does not solely consist of the vacuum chamber. There are several peripheral apparatus which must connect to the chamber in order to produce an operable system. These are all pieces of hardware designed for this sensor head which will be housed inside the magnetic shields. These include the magnetic shields themselves, the mounting structure

to attach everything to, the coils used to produce the necessary magnetic environment and optical systems for cooling, interrogation and detection.

Mounting Structure

The mounting structure is what physically connects the vacuum chamber to the sensor head peripherals. It starts with mounting points on the vacuum chamber itself. These are threaded holes machined into the vacuum chamber when constructed. Care has to be taken not to create leaks in the vacuum when designing their placement. Peripheral structures can be attached to these mounting points. The concept for this structure is to have four rods which span the entire height of the sensor head. Peripherals can be clamped to these rods and the magnetic shields can be held in place by screws which attach to them. The mounting structure is displayed in figure 3.10.

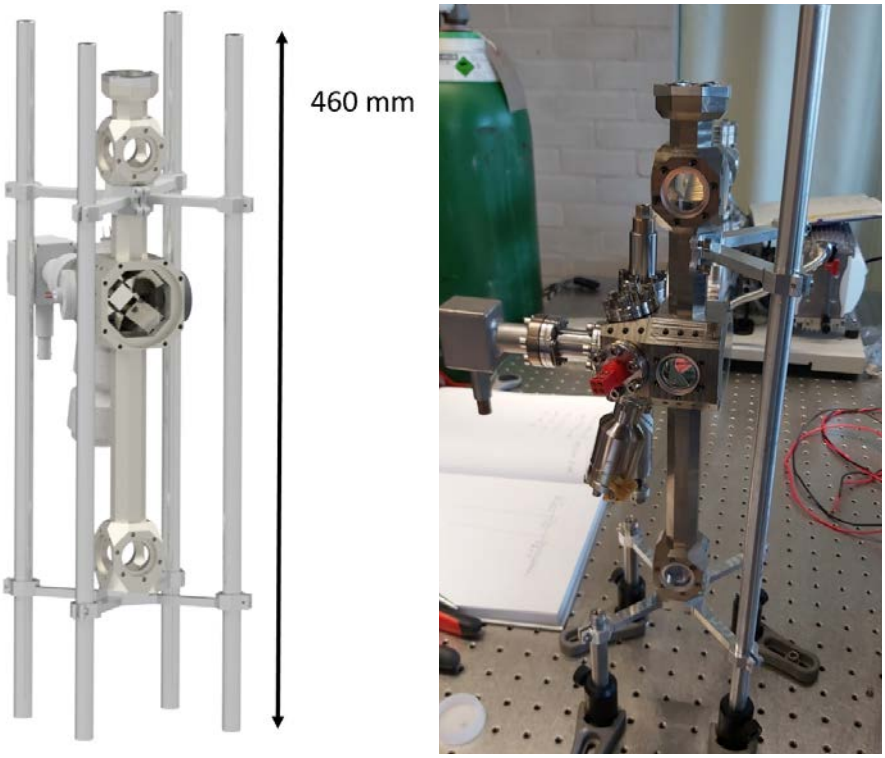

(a) CAD model of the mounting structure.(b) Photograph of the mounting structure being assembled.

Figure 3.10: The mounting structure which connects the vacuum chamber to the peripheral components of the sensor head.

The first mounting points to highlight are those surrounding every optical window. These serve two purposes. Firstly, when doing indium sealing, these are used to fix the compression flange to the chamber (see appendix B). Under normal operation these threaded holes are used to attach optics to the chamber. These could be photodiodes, collimators or mirrors. Mounting joins between the optical elements are made through custom designed mounts either machined from lightweight aluminium or 3D printed from plastic. General mounts for fixing common 1" optics standard threaded elements were created. Examples of these mounts are shown in figure 3.11.

(a) Photograph of a completed window. (b) Photograph of the window adaptor with mirror.

Figure 3.11: Photographs showing how an adaptor is attached to the indium sealed windows for optics components.

3.4.1 Magnetic Field Control

Magnetic Shields

The magnetic shields are a vital aspect of the environmental isolation of the system. For atomic sensors (particularly magnetically sensitive species such as rubidium) it is necessary to nullify any external magnetic fields which, for example, perturb energy levels through the Zeeman effect. In lab based experiments this can be done with compensation coils, Helmholtz coils used to compensate external fields. However, for systems designed for mobile platforms such as in this thesis, a solution for passively nullifying the field is preferable. Magnetic shields greatly reduce magnetic field strength inside the shielded region. Because this is passive it is useful for systems that will be subject to changing magnetic environments.

From simulations performed by *Magnetic Shields Limited* we concluded that the op-

timum geometry for shielding factor is a cylinder with end caps. Ideally several layers with small air gaps between would be used. Due to the constraints of this work (namely the weight and the geometry of the system) some compromises have to be made. Firstly, only a single layer of 0.5mm thick shield is used to reduce the weight as much as possible. This is the minimum thickness for mechanical robustness of the shield. Secondly, the shield was produced in two parts to allow the shield to be easily removed. Also, some holes were designed into the shield to allow access for cables and for the ion pump to sit outside of the shield. The placement and size of these holes was optimised for as little disruption to interferometry regions as possible while allowing necessary access. The holes were placed in line with the MOT region, the least magnetically sensitive region of the experiment. The simulations (performed by *Magnetic Shields Limited*) for the shield can be seen in appendix C.

The magnetic shields have to fit with the size and weight constraints of the sensor head budget. The shields were designed to take up 460 mm, nearly the height of the complete system. The diameter was chosen to be 20 mm in order to minimise size and weight but allow internal space for peripherals. The weight of both shields is 1.3 kg which is a significant portion of the weight budget, though much lower than typical magnetic shields. The holes in the top are positioned to match with the mounting posts. The central axis of the vacuum chamber is slightly offset from the central axis of the magnetic shields. This allows more room for the two inch optics needed for the cooling collimator.

The shields were tested by placing a magnetometer (*fluxgate magnetometer*) inside the shields when the shields were placed inside a solenoid producing a field of 5 G. The shielding factor was great enough that we could not distinguish on the magnetometer between the solenoid being turned off and on. Given the resolution of the sensor (0.1 Gauss) the shielding factor is determined to be at least 50.

(a) CAD models of how the magnetic shields fit on the system.

(b) Photograph of the vacuum system housed in one of the shield halves.

Figure 3.12: How the two halves of the magnetic shield fit with the vacuum chamber.

MOT coils

The coils used for enabling the spatially dependent force in the MOT are integral to a producing a cloud of cold atoms. Although the optimum for ^{87}Rb was experimentally found to be 11 G/cm, it is necessary to be able to produce a field gradient of 15 G/cm for testing and optimisation. The magnetic field produced by the coils can be simulated using the Biot-Savart law. Typically the geometry (separation and radius) is set by the vacuum chamber. To keep heating and electrical inductance low, a current through the 1mm diameter copper wire should be kept to less than four amps. The field was simulated with a separation of 39 mm and a coil radius of 50 mm (roughly Helmholtz geometry). The geometry is shown in figure 3.13 and the simulation is shown in figure 3.14. With a current of 3 Amps, the number of turns required to produce 15 G/cm is 140.

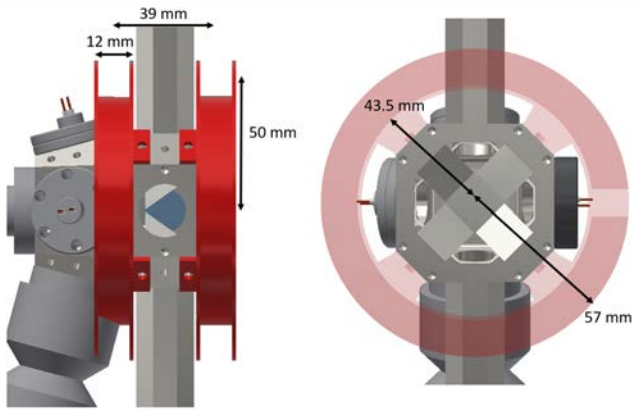

Figure 3.13: A model of how the MOT coils are designed to fit with the vacuum chamber and the key dimensions.

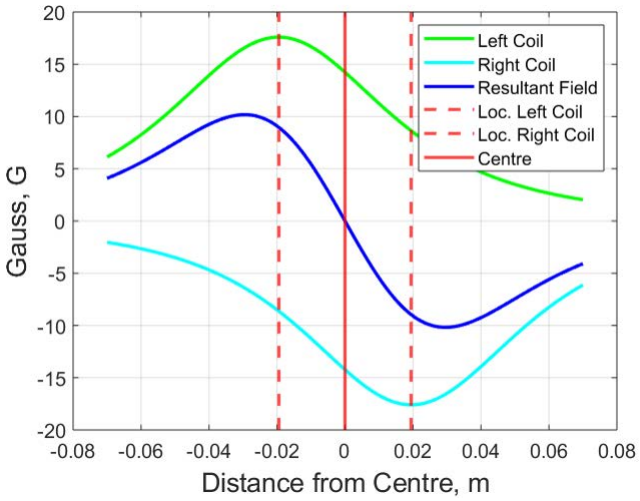

Figure 3.14: A simulation of the magnetic field strength from the MOT coils. The field gradient in the central region with the simulated 1 A current is 5 G/cm.

Bias Coils

In order to drive transitions between specific magnetic sub-levels it is necessary to define a magnetic quantisation axis. Due to the Zeeman effect the magnetic sub-levels will be

perturbed by this field. To ensure the desired transitions can be driven by the interrogation beams this quantisation axis needs to be the same as the interrogation axis (vertical). A bias field is often produced by a solenoid which encompasses the sensor head. Here, owing to the geometry of the system, several coils are to be placed along the sensor head (see figure 3.15. These coils can be used to create a constant bias through the whole sensor head or tuned to produce different bias fields in the interrogation regions for the top and bottom clouds.

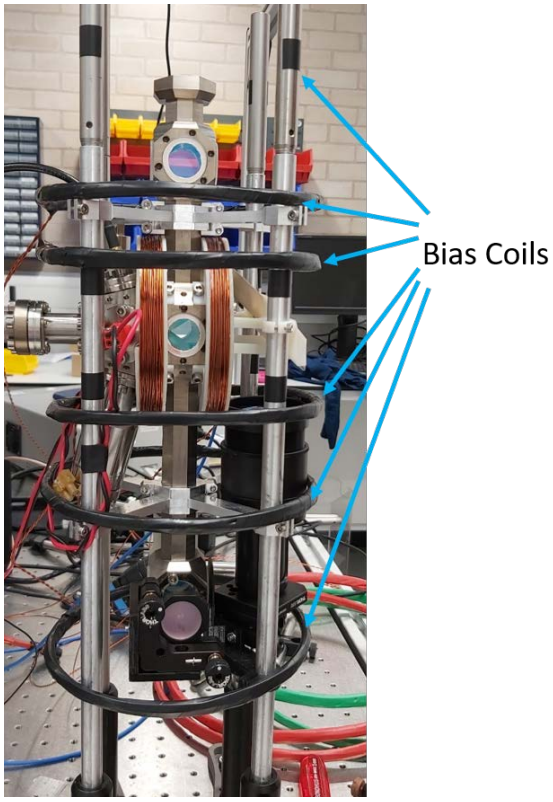

Figure 3.15: A photograph of the bias coils mounted to the structure. Black tape marks the position of the missing top coil.

This set of coils can also be used to compensate external fields (typically when the magnetic shields are not installed). The compensation field approximated from the separate coils is modelled in figure 3.16. While the resultant field is not constant throughout the chamber, the flexibility afforded by the separate coils is beneficial. Particularly as this

compensation field is only required for the cooling stage over a small region (∼10 mm) when shields are not installed, the field variation over this region is relatively small (∼0.01 G).

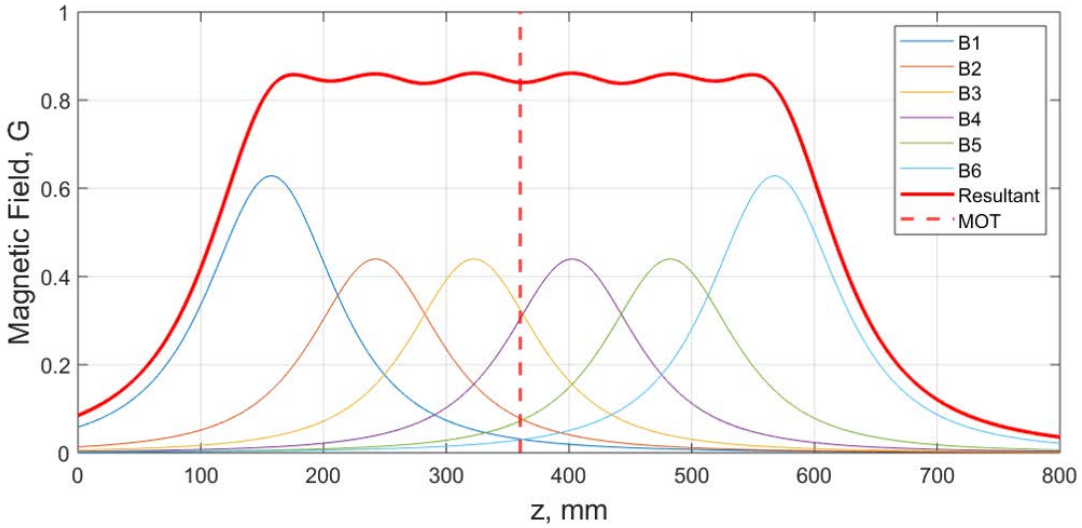

Figure 3.16: A model of how the bias coils can be tuned to create a close approximation of a uniform field.

Microwave Antenna

A microwave antenna can be used to drive transitions between the two ground states of the D2 line in ^{87}Rb, separated by ∼6.8 GHz. This can be used to drive transitions between the relevant hyperfine ground states, such as for state preparation. Microwaves can be used to transfer the population between the magnetically insensitive $m_F = 0$ states. If a strong bias field is applied this will separate the magnetic sub-levels and allow a transition to be tuned to drive a single transition. Through the use of this and blow-away pulses a very clean state of atoms in a single magnetic sub-level can be prepared.

The chamber has been designed to include a microwave antenna into the vacuum environment to be able to do this state selection. The microwave antenna is produced from

a rigid SMA cable by stripping the outer (ground) layer off at a quarter of the wavelength (11 mm) from the end. This is inside vacuum and is connected to the outside through an SMA connecting flange. The antenna is placed directly behind the mirror in the MOT region.

3.4.2 Optical Delivery

Cooling Collimator

The cooling collimator is necessary to deliver the cooling light into the chamber at the correct size and polarisation. The light is delivered into the sensor head from an optical fibre. The final size of the beam is required to be two inches for the MOT chamber. The light needs to be circularly polarised to drive the sigma transitions required for MOT trapping. A linear polariser is used to prevent polarisation fluctuations, this is aligned to the axis of the polarisation maintaining fibre for maximum power transmission. A quarter wave-plate is aligned to create a circularly polarised beam. The collimating optics are based on a simple two lens set-up to realise the desired beam size.

The whole optical system needs to be in line with the sensor head to have the smallest volume footprint possible, enabling it to fit inside the magnetic shields. To achieve this a 45 degree mirror is used to direct the collimated beam into the chamber. The mirror is fixed to the chamber and the support bars. The collimator is fixed to the chamber via an opto-mechanic mount. The design and realisation are displayed in figure 3.17.

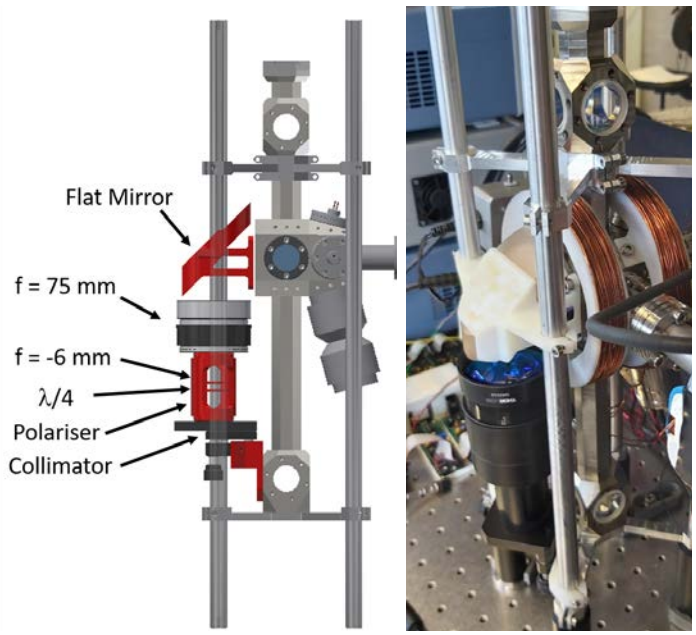

(a) A CAD model. (b) A photograph.

Figure 3.17: Design and realisation of how the cooling collimator fits in the wider sensor head design.

Interrogation Beams

Similarly to the cooling beam, the interrogation beam needs to be delivered to the chamber at the correct size and polarisation. A conversion piece is used as the chamber is angled by six degrees for the top and bottom windows (to minimise reflections). An adaptor for optical components is used to allow for use of off-the-shelf optics. A beam size of 11mm diameter is needed, this can either be achieved by buying a collimator of the correct size or by using an oversized one with an iris (reducing optical power but giving a more homogeneous intensity). Different polarisations can be used for different schemes (co-propagating or counter-propagating). A rotation mount for this beam is included to be able to adjust polarisation, the polarisation of the input being set by the fibre delivery. A model of this system is shown in figure 3.18a.

A mirror on the bottom of the chamber can be installed easily for counter-propagating schemes. For this a similar adaptor is used. This also includes a custom designed, low volume translation mount, photograph in figure 3.18b.

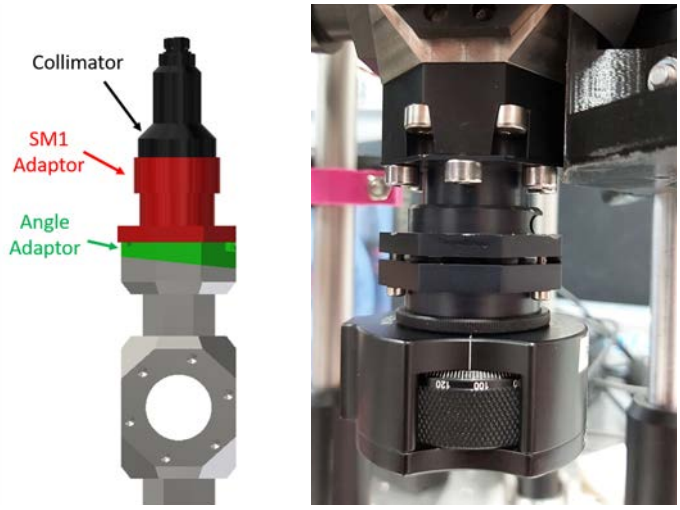

(a) Optical delivery. (b) Mirror mounting.

Figure 3.18: The optical system for the interrogation, showing the design for the delivery and a photograph of the mounting for the retro-reflecting mirror.

Detection

The final peripheral part to mention is the detection optics. This includes input collimator, mirror and photodiodes. The input collimator follows a very similar concept to the cooling beam in that it is angled to be inline with the chamber and reflected from a right angle mirror. An off-the-shelf collimator is used, producing an 18 mm diameter beam. The mirror (used to balance the scattering forces) is attached to the chamber using the standard adaptor part for optics components that was designed. The design can be seen in figure 3.19.

Two detection schemes are used in the process of this work. First, when measuring cloud temperature, a light sheet is used. A 0.5 mm horizontal slit is placed in the centre of

a blocked beam. When the atom cloud passes through this light sheet, the atoms fluoresce, allowing a measurement of the vertical extent of the cloud (see section 5.1.2). The other scheme involves an unblocked and un-reflected beam of 18 mm diameter that can be used for differential state detection (see section 5.1.3). The detection light is pulsed on, with frequencies corresponding to the two ground states, to measure the atom population in the corresponding states through fluorescence (see section 5.1.3).

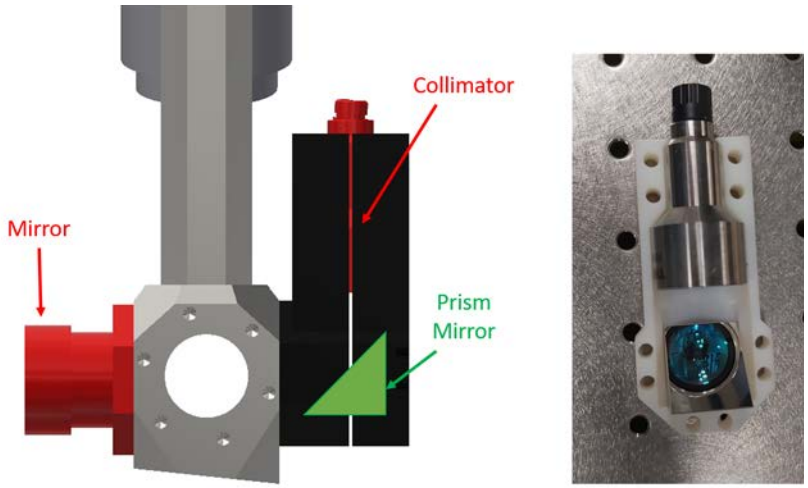

Figure 3.19: The detection system designed for use in the sensor head.

3.5 Summary

This chapter has presented the design process of the sensor head sub-system for a compact and portable atom interferometry system. Novel measurement sequences to create a sensitive gravity gradiometer measurement from a single atomic cloud have been presented, one of which has been filed for patent [70]. This is necessary for the desired compactness of the system as a whole. The design and construction of the vacuum system and peripherals to house this atomic scheme have also been described. In order to meet size and weight

constraints much of this has been custom designed.

The sensor head as a whole has a size of 14.1 Litres and 7 Kg. The power consumption is calculated as part of the supplying sub-systems. The vacuum system maintains a level of 8×10^{-11} mbar with the atomic dispenser off. An interrogation beam of 11 mm diameter is used. With a novel sequence allowing a baseline of 260 mm between atom interferometers (and assuming $5{\times}10^4$ atoms with a cycle time of 1.5 s), a designed shot-noise limited sensitivity of 500 E/$\sqrt{\text{Hz}}$ is projected.

Chapter Four

Compact Laser System

This chapter will describe the conception and construction of the laser and microwave chain sub-systems which drives the atomic processes. These are designed to have all of the functionality to enable the measurement sequences described in section 3.2. The sub-systems must also fit within the size, weight and power supply constraints of the whole system. To achieve this, a novel approach has been taken, resulting in an agile, single source laser system.

The laser system has to be able to produce the necessary frequencies for cold atom preparation, interrogation and detection, plus the Bloch elevator (details in chapter 2). Through frequency modulation it is straightforward to drive pairs of frequencies [71, 72], for rubidium 87 all of the required transitions can be achieved with only a pair of frequencies present at any one time. These pairs of frequencies need to be present in the same beam at once. The frequency, linewidth and power requirements for these frequency pairs are summarised in table 4.1.

These frequencies all drive transitions in the D_2 line in ^{87}Rb. The relevance of the transitions driven and hence the frequencies is described in chapter 2. The frequency pairs

Table 4.1: Requirements for each of the optical frequencies and the microwave frequencies to drive them, organised into their respective pairs. The frequency detuning from the upper optical transition as well as the microwave tuning range used to drive these are displayed. Also, the optical linewidth and power are given. Detail on the atomic processes driven by these frequencies is given in chapter 2.

Laser	Detuning	Frequency Range	Linewidth	Power
Cooling	15-121 MHz	613-673 MHz	<1 MHz	>100 mW
Repump	0 MHz	6.568-6.689 GHz	<1 MHz	>1 mW
Raman 1	750 MHz	1.2 GHz	<100 kHz	>50 mW
Raman 2	0-5 MHz	6.831-6.835 GHz	<100 kHz	>50 mW
Bloch 1	50 GHz	25 GHz	<200 kHz	>100 mW
Bloch 2	0-3 MHz	0-3 MHz	<200 kHz	>100 mW

are displayed on the energy level diagram of the ^{87}Rb D_2 line in figure 4.1a. It is also instructive to picture these frequency pairs with respect to a rubidium absorption spectrum. This allows a better relative view of the frequencies involved. This is shown in figure 4.1b along with the locking frequency used.

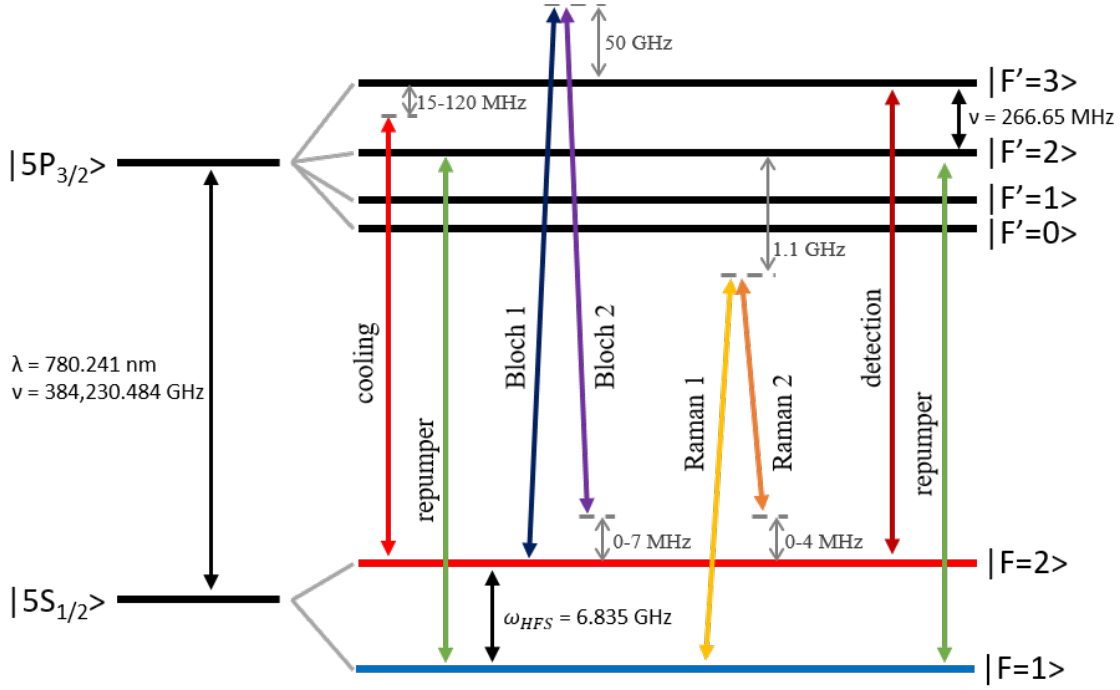

(a) A level diagram for the $D2$ line in ^{87}Rb [55]. The frequency pairs used in this work are displayed.

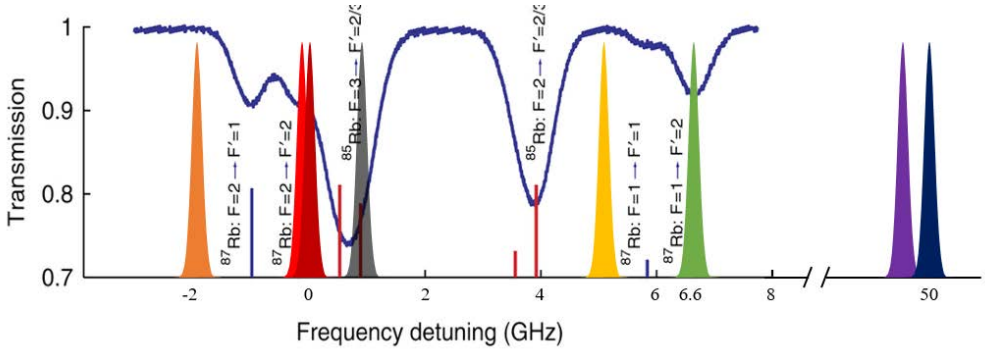

(b) Showing the frequency pairs against the absorption spectrum of rubidium (mixed species). The locking frequency is shown in grey.

Figure 4.1: Displaying how the frequency pairs required relate to the level diagram and frequency spectrum of rubidium.

As well as being able to produce the correct frequencies, this system has to be able to tune between these frequencies fast enough for the experimental parameters. An interferometry sequence can take 100-200 ms so any frequency shift will have to occur at the millisecond level. It is necessary to be able to ramp the frequency of the laser output, most importantly at ∼25 MHz/s to compensate the Doppler shift due to free fall and at ∼70 MHz/ms for optical molasses.

The laser must also be able to supply sufficient power to drive the transitions at sufficient rate. For laser cooling, typically an intensity of 2-3 times the saturation intensity is required, which for the beam size determined in chapter 3 would require ∼100 mW. The linewidth of the laser must also be narrow. Particularly for the Raman transitions, the linewidth of the laser can limit the sensitivity of the instrument [73].

The dual frequency system developed must have the ability to independently tune each individual frequency. Frequency 1 will be used as Cooling (C), Raman 2 (R2) and Bloch 2 (B2). Frequency 2 will generate the Repump (Rp), Raman 1 (R1) and Bloch 1 (B1) frequencies. This is to keep the second frequency always with a higher frequency with respect to the first. With these frequencies, all necessary transitions for the techniques described in chapter 2 are possible. The particular frequencies can be seen in figure 4.1.

Finally, the whole laser system has to meet the size, weight and power constraints imposed by the project outline. Additionally, it is beneficial for the laser system to be easily modifiable while also being compact. A novel solution for this will be presented later in section 4.4. The full requirements list for the laser sub-system is given in table 4.2.

To produce the two frequencies while maintaining as small a system as possible, a single arm laser system was designed. Through the use of a state of the art component, the *in-phase quadrature modulator* (IQM), it is possible to produce two independently tuneable frequencies. The rest of this chapter will describe the use of this component for an agile

Table 4.2: Summary of the requirements of the single-arm laser sub-system.

Property	Requirement
Laser Linewidth	<100 kHz
Laser Power	>100 mW
Frequency 1 (C,R2,B2) relative to locking point	0.6-1.2 GHz, 25 GHz
Frequency 2 (Rp,R1,B1) relative to Frequency 1	6.5 GHz, 6.8 GHz
Laser switch on/off time	<100 ns
Frequency 2 attenuation	>60 dB
Outputs	3 fibred outputs
Size	<20 L
Weight	<8 kg
Power	<100 W

atom interferometry laser, the design and construction of a single-arm laser system and the microwave chain used to drive it. The design philosophy and procedure to put these sub-systems into low volume and weight packaging will also be described.

4.1 In-Phase Quadrature Modulators

The use of this state of the art technology allowed the production of an agile, single arm laser. By using two connected in series a hugely agile two-frequency spectrum with broad scanning range is achieved. This component has been utilised in atom interferometry experiments to suppress parasitic transitions as it can be used to create only a single side-band [74, 75]. In this work however, the use of this component is expanded by use of two in sequence to allow the full tuning of two frequencies independently.

The IQM's operate in a similar way to an *electro-optical modulator* (EOM). An EOM adds frequency side-bands at the driving frequency above and below the carrier. An IQM essentially forms an interferometer with each arm containing an EOM in a nested interferometer. The phase relationship between arms of the nested interferometers and the arms of the larger interferometer can be adjusted (figure 4.2). This allows the IQM to be operated in many modes, such as adding only a single side-band (OSSB) or suppressing the carrier (SCOSSB) [74] (figure 4.3a). The IQM's used in this work are the *MXIQER-LN-30* from *iXblue* [76].

To produce the frequency output necessary for the experiment, the first IQM is operated in suppressed carrier, optical single side-band (SCOSSB) mode. This shifts the central frequency from the locking point to that of frequency 1 (e.g.cooling). The second IQM is operated in optical single side-band (OSSB) mode, adding a single side-band into the spectrum. Both of these frequencies can be independently controlled by changing the input RF

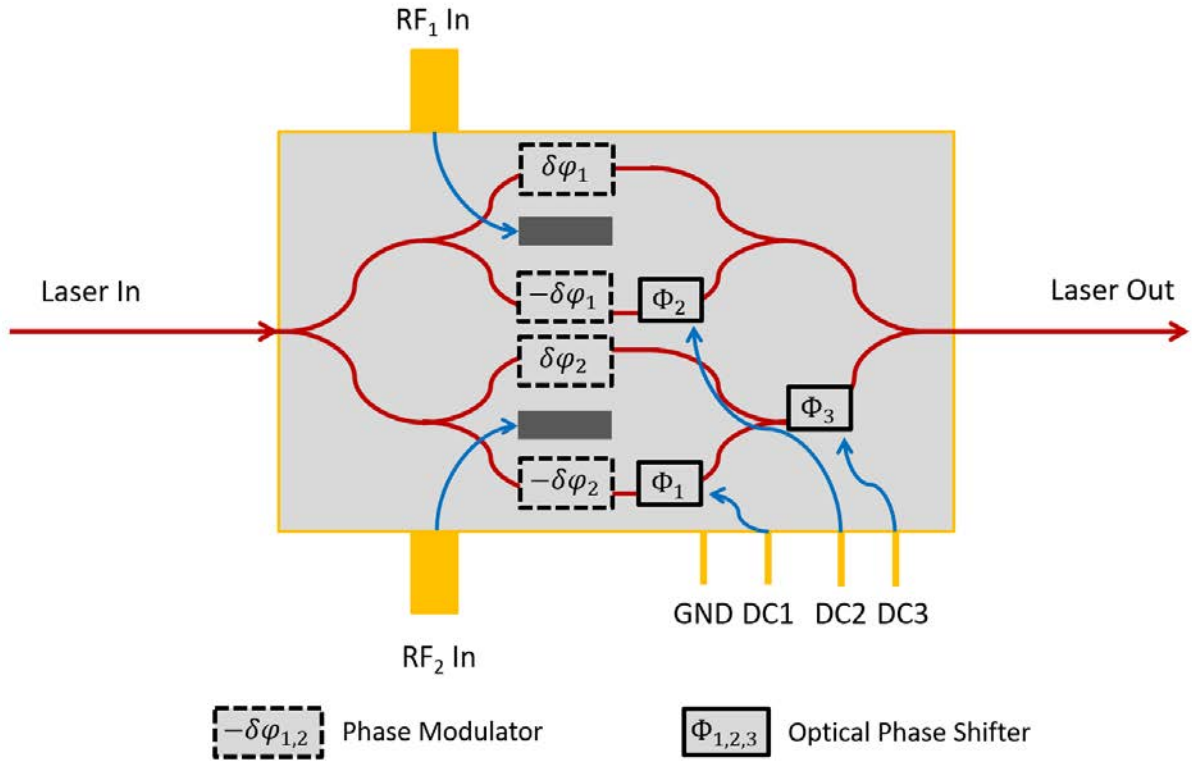

Figure 4.2: A diagram showing the internal function of an IQM. The RF inputs are used to control the internal EOM's and the DC inputs to change the phase of the nested interferometers. More detail can be found in [76, 74].

frequency to the IQM's.

To achieve the primary large frequency sweeps required for Frequency 1, IQM1 is in SCOSSB mode. In this operation, a single side-band frequency is added into the spectrum at the driving frequency away from the carrier, while the carrier frequency is suppressed and carries negligible optical power. This effectively shifts the central frequency away from the locking frequency and allows control of this frequency. The IQM can be locked into this mode using monitoring diodes and control software. The process is inefficient, only retaining ∼10% of the seed optical power. The spectrum after the first IQM is shown in figure 4.4.

The light is then passed through IQM2. This is operated in OSSB mode. This

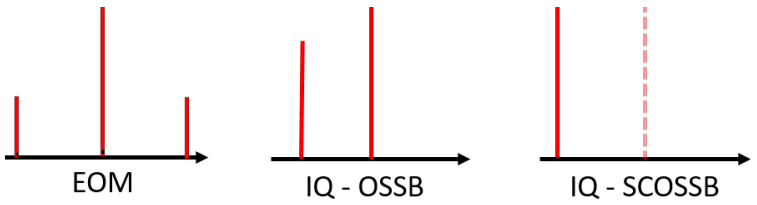

(a) Examples of the operating modes used with the IQM's compared to an EOM. plotted on a frequency axis.

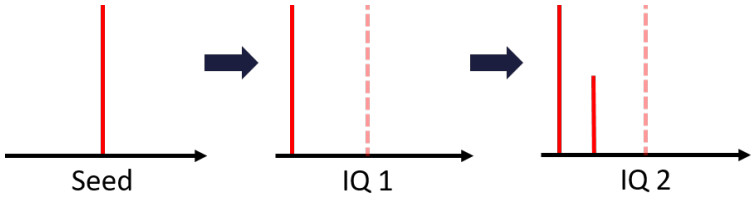

(b) A diagram showing how two IQM's are used in series to produce two independent frequencies. The first operates in SCOSSB mode and the second in OSSB mode.

Figure 4.3: Diagrams showing the operation of IQM's in frequency space and how they are combined in this work.

produces a single side-band at the driving frequency away from the carrier (from IQM1), along with the carrier. The relative power between the carrier and side-band can be tuned. The side-band (SCOSSB) from IQM1 acts as the carrier for the second IQM. The complete spectrum after both IQM's can be seen in figure 4.5.

Using the configuration from figure 4.5 all of the frequency pairs necessary for our atomic processes are produced using a single seed (summarised in table 4.1). The frequency produced by the first IQM is the one used for Cooling, Raman 2 and Bloch 2 beams. The side-band on this produced by the second IQM is used for the Repump, Raman 1 and Bloch 1 beams. The complexity of how these frequencies are generated is in the microwave chain, described in section 4.3.

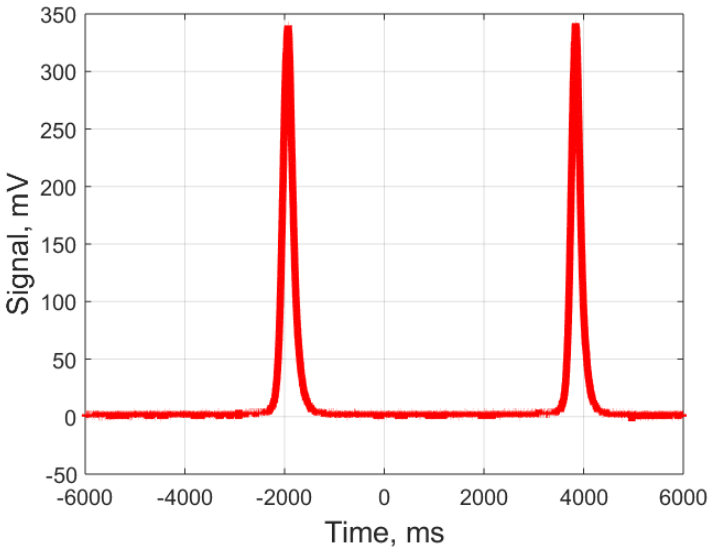

Figure 4.4: Optical spectrum after a single IQM locked to produce a single side-band with no carrier. Seen at 1560 nm on a Fabry-Pérot cavity. Light is injected into the cavity, whose length is scanned. Two peaks are seen, though they represent the same feature, the free spectral range of the cavity apart. This is used to convert the time scale of the oscilloscope to frequency. The leftmost peak is shifted from the locking, carrier, frequency which is suppressed.

4.2 Single Arm Laser

In this section the design, construction and testing of the single arm laser system will be presented. The individual components and their affect on the laser output will be described. The microwave chain used to generate the control frequencies will then be described in section 4.3.

The design of this compact and robust laser system is based on a few core principles. Firstly, using as few components as possible will minimise the size and weight. This principle has been developed in other work [77, 78, 80, 79], but not to the extent presented here.

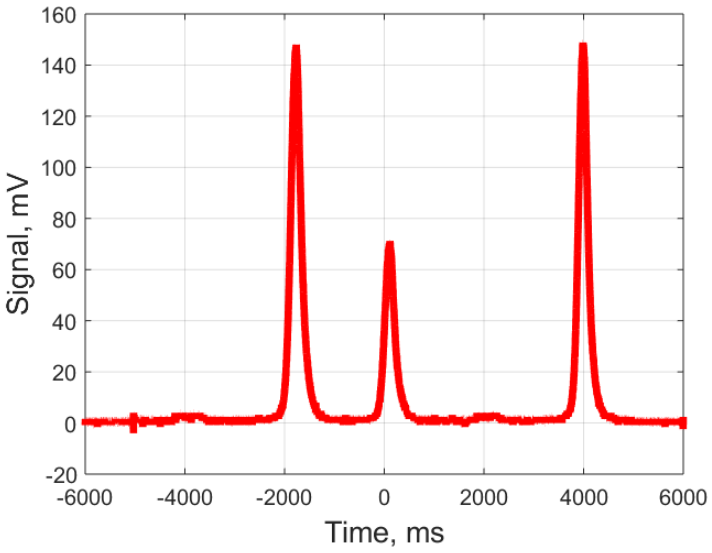

Figure 4.5: Optical spectrum after two IQ modulators in series, locked to produce a spectrum with two frequencies. Seen at 1560 nm on a Fabry-Perot cavity. The carrier spectrum is that from IQM1 in figure 4.4, now with the side-band at around the origin.

Secondly, the use of fibred components makes for a more robust and portable system. And finally that using telecommunications components (at 1560 nm) and frequency doubling (to 780 nm) makes use of a mature and cost effective technology. Much work has been done previously on telecom fibred laser systems [71, 78, 81].

The laser system is based on telecommunications components at 1560 nm. This technology is mature, making the components generally more robust, reliable and cheaper. All manipulation of the laser frequency and power is done at 1560 nm. Towards the end of the chain, a frequency doubling crystal converts the frequency spectrum into the 780 nm necessary for ^{87}Rb experiments. The single arm laser chain is shown in figure 4.6.

The first component in the chain is the Seed laser. A *Rio Grande* laser is used, capable of outputting 2 W of 1560 nm with a linewidth below 10 kHz [82]. This particular seed is used as it has a narrow linewidth, robust manufacture and, most importantly, a high output

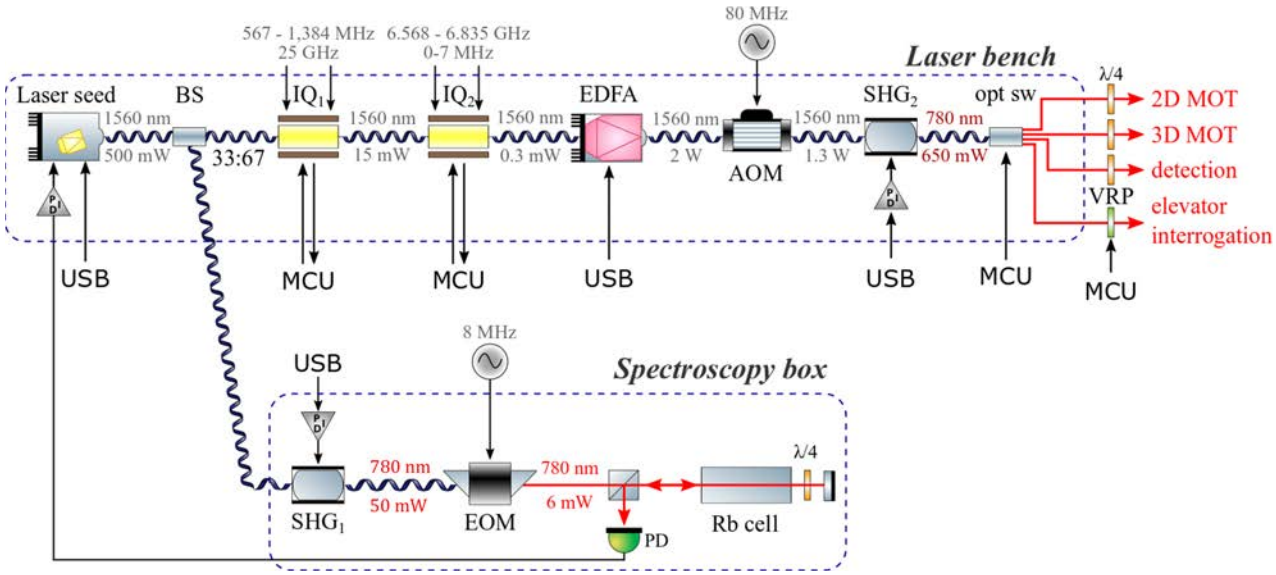

Figure 4.6: A schematic of the single arm laser system designed and produced for this work. The laser seed outputs light at 1560 nm, with a spectroscopy system used to discipline the seed frequency. IQM's in series are used to control the frequency spectrum, an EDFA and an AOM are used to control the power. A PPLN crystal is used for frequency conversion and finally an optical switch is used to deliver light to different ports in the sensor head. The MCU refers to an optical multiplexer and the VRP to a variable retarder plate to control polarisation.

power. High seed power is necessary as the IQM's in the chain are inefficient and after losses from these enough power is required to seed the amplifier (EDFA).

After the two IQM's in series (section 4.1), the next element in the chain is an optical intensity amplifier, an *erbium-doped fibre amplifier* (EDFA). The EDFA used is a *CEFA-C-PB* from *Keopsys* [83]. This element is capable of amplifying the intensity out of the IQM's (-5 dBm) up to 1W (30 dBm).

To precisely and quickly control the intensity of light, an *acousto-optic modulator* (AOM) is used. Specifically, the fibre coupled *MT80-IIR30* from *AA Opto-Electronic* [84].

The power output is controlled by a *voltage variable attenuator* VVA. The response of the optical power output for the AOM to the input RF power is non-linear. The relationship was characterised, shown in figure 4.7a. The dependence of the AOM on input RF frequency is shown in figure 4.7b.

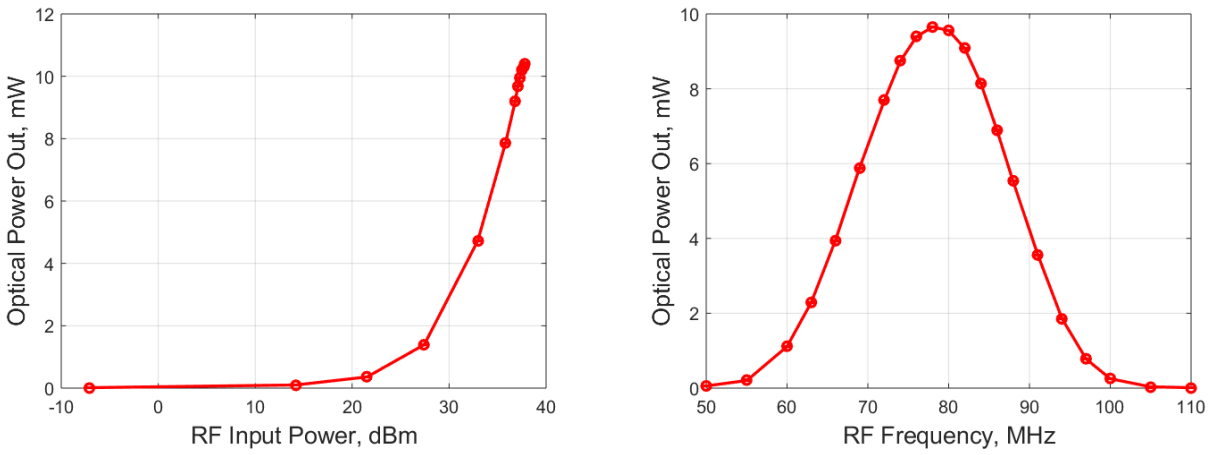

(a) (b)

Figure 4.7: Characterisation of the AOM's optical output power with respect to (a) the input RF power and (b) the driving RF frequency. From this, the AOM is driven at 80 MHz.

A *second harmonic generation* (SHG) crystal is used to convert the wavelength from the telecom components previously in the chain (1560 nm) to that necessary for the experiment (780 nm). The SHG used is a *periodically poled lithium niobate* (PPLN) wave-guide, the *WH-0780* from *NTT Electronics* [85]. The optical conversion efficiency of the PPLN is highly dependant on the crystal temperature due to phase matching. The temperature of the crystal in controlled using a Peltier element. The relationship between temperature and efficiency is shown in figure 4.8a. The second harmonic generation process slightly alters the optical spectrum when using the IQM's [74]. The spectrum after frequency doubling can be seen in figure 4.9. The maximum output power we have achieved at the experiment is ∼200 mW which is more than sufficient for the requirements (table 4.2).

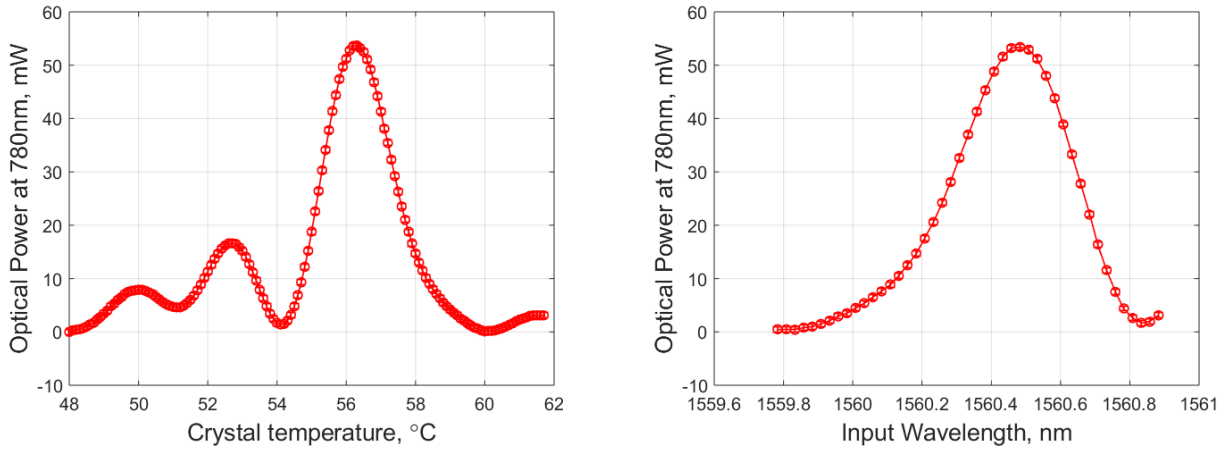

(a) (b)

Figure 4.8: Characterisation of the SHG's optical output power with respect to (a) the crystal temperature and (b) the input wavelength. The optical power input was 100 mW, the SHG is $\sim 55\%$ efficient at its peak.

Finally, an optical switch is used to direct this light into the different input ports of the chamber – cooling, interrogation, detection and a dump channel. A splitter is used to have a small amount of light to monitor on a Fabry-Pérot cavity. The four-way switch used was the *EOL 1×4 NIR* from *Laser Components* [86]. The switching time for this is shown in figure 4.10. Although the optical switch switches in $\sim$7 ms, the AOM is used to switch the light on and off in less than 100 ns.

4.2.1 Lock Box

To have a consistent frequency reference for the laser system, it is disciplined by spectroscopy. This involves identifying a frequency standard from an atomic species and using control electronics to lock the seed laser to this. This mitigates the drift of the seed frequency associated with ambient temperature changes. As with the rest of this work, the spectroscopy

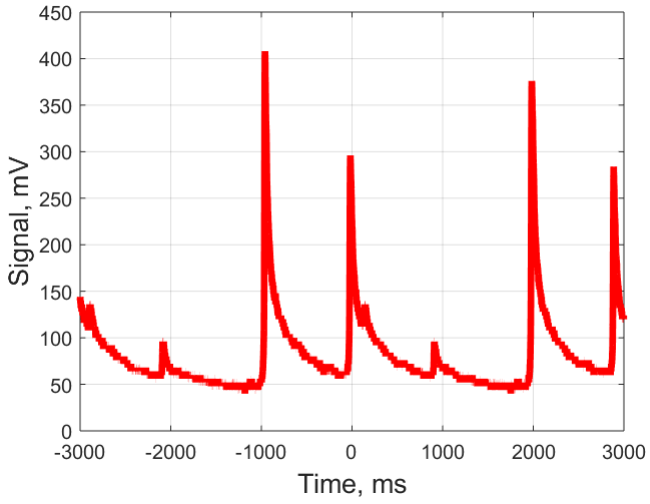

Figure 4.9: Example optical spectrum after both IQM's in series, locked to produce a spectrum with two frequencies. The first IQM is in SCOSSB mode and the second in OSSB mode. Seen at 780 nm on a Fapry-Pérot cavity. The resolution of this cavity is lower than the one at 1560 nm.

has to be compact and robust. This section will outline the compact spectroscopy and locking electronics developed.

The locking scheme used is *frequency modulation* (FM) spectroscopy [87, 88, 89]. This is an optical heterodyne spectroscopy formed from the absorption signal through an atomic vapour. As a counter-propagating pump and probe beam are used, the signal is Doppler-free. This allows a significant improvement in the linewidth of the laser when locked as there is no thermal broadening present. The probe beam is frequency modulated and the beat signal measured on the photodiode is demodulated and used for locking. An oscillator is used to modulate the frequency of light and then demodulate the observed signal.

Adding frequency modulation to *saturated absorption* spectroscopy is beneficial over using only saturated absorption spectroscopy. Although Doppler-free, saturated absorption spectroscopy returns an absorption signal which is symmetric around the central value.

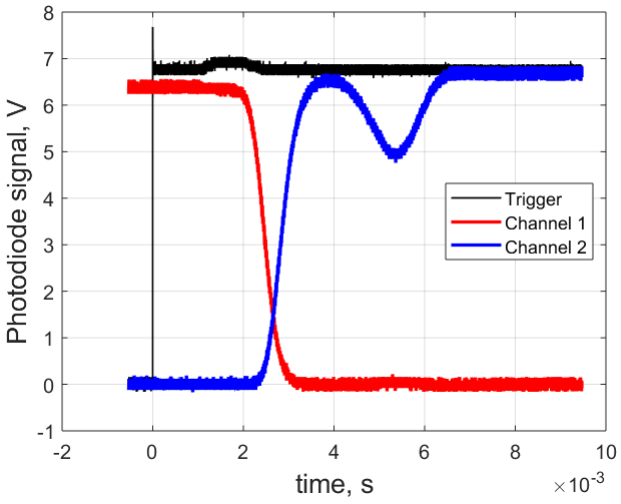

Figure 4.10: Characterisation of the optical switch. This is a typical profile of switching between two of four channels. This is used to determine a 7 ms delay between triggering and the light fully switching.

This makes defining in which direction the frequency has drifted difficult. An edge of the absorption signal can be used for locking,however this couples intensity and frequency noise. Through modulation, FM spectroscopy is like taking the derivative of the absorption signal. This returns a narrow linear slope centred on the central value which is robust against intensity changes.

The laser locking hardware as a whole is made of three distinct parts. The first is the optical system used to generate the spectroscopy signal. This constitutes a single aluminium plate upon which all optical elements are rigidly fixed. The second part is for the modulation signal generation and demodulation of the photodiode signal. The final part is the locking electronics. This is a home-built PID (*proportional-integral-derivative*) PCB using analogue signals. The complete system can be packed into a 2.4 L, 1.3 kg box.

The optical system comprises of a PPLN crystal to convert the frequency from the seed, an EOM to frequency modulate the beam, a cell containing rubidium vapour and a

photodiode to measure the absorption signal. The modulated beam initially passes through the polarising beam splitter (PBS) and the rubidium cell. The quarter-wave plate and mirror produce a counter-propagating beam with orthogonal polarisation. At the PBS this beam is directed into the photodiode. The setup is shown in figure 4.11.

The chain for generating the modulation signals (RF) is first generated by the oscillator in the *microwave chain* (section 4.3). This produces an 8 MHz signal. This is split, one part going to produce the modulation on the EOM and the other phase shifted and mixed with the photodiode signal to demodulate. The schematic for this is shown in the lower section of figure 4.12.

The locking electronics are based on the PID technique. This feedback loop is ubiquitous in control systems and provides a method for adjusting an output to reach a set-point value. This is done through continual calculation of an *error value* which is the residual of the previous output and the set-point. The *proportional*, *integral* and *derivative* parts each individually control aspects of the output through manipulation of the error signal.

The three parts of the locking system, optics, RF chain and locking electronics can each fit in a footprint of 100 mm $\times$ 200 mm. All of the parts are thin, none having height greater than 40 mm. These sub-systems can be assembled on top of each other, being packaged in a 2.4 L, 1.3 kg box.

4.3 Microwave Chain

In minimising the size, weight and power consumption of the laser by using only a single arm, the complexity of the RF electronics system has been increased. Overall this has made the system as a whole more lightweight and portable. Electronic components are generally lower

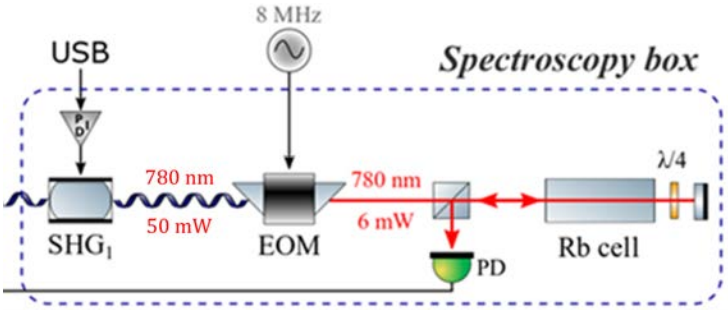

(a) A diagram of the spectroscopy system, taken from 4.6.

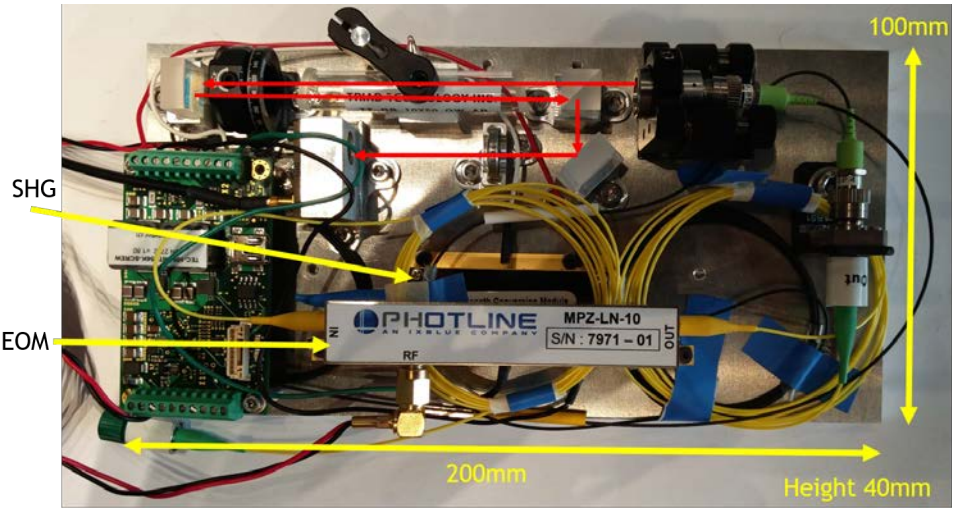

(b) Photograph of the assembled spectroscopy system. The fibred parts are labelled, the free space optical path is shown in red.

Figure 4.11: The compact spectroscopy system designed and produced.

SWaP than optical and in places the complexity can be in software rather than hardware. In this section, the design, testing and construction of the microwave chain used to drive the laser is presented. The full microwave chain is shown in figure 4.12.

The most crucial frequency necessary for atom interferometry experiments using ^{87}Rb is the 6.8 GHz for the Raman process. To generate this frequency a 7 GHz source is mixed with a ∼200 MHz signal for subtraction. The whole microwave chain is seeded from from a phase locked dielectric resonator (OCXO), the *NXPLOS-I-0700* from *Nexyn*.

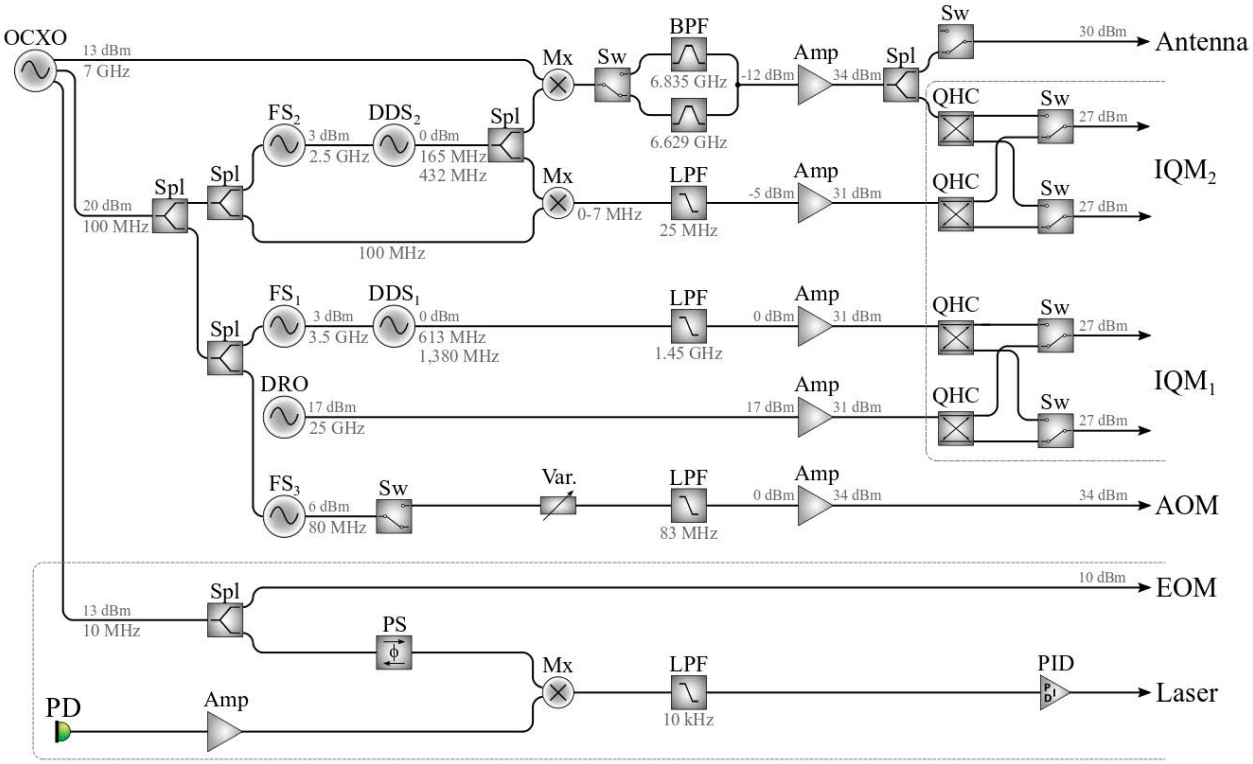

Figure 4.12: A schematic of the microwave chain designed and produced for this work. Acronyms: OCXO - Oven Controlled Crystal Oscillator, Spl - Power Splitter, FS - Frequency Synthesiser, DDS - Direct Digital Synthesiser, Sw - Switch, BPF - Band Pass Filter, Amp - Amplifier, LPF - Low Pass Filter, DRO - Dielectric Resonator Oscillator, Var - Variable Attenuator, PS - Phase Shifter, Mx - Mixer, PD - Photo Detector, PID - Proportional Integral Derivative Feedback.

The microwave chain used to drive the laser is responsible for generating the inputs to the two IQM's. One part of the microwave chain is the delivery to the first IQM. This creates the frequency to shift the laser seed from the locking frequency in SCOSSB. It produces a side band frequency at the driving frequency away from the locked frequency. This frequency goes between ∼600 MHz for cooling/detection to ∼1.3 GHz for Raman interrogation. It rapidly tunes the frequency when performing optical molasses, 70 MHz/ms.

To produce these frequencies a *direct digital synthesiser* (DDS) clocked by a *frequency synthesiser* is used. The frequency synthesiser is an *LMX2594* from *Texas Instruments* and the DDS is an *AD9914* from *Analog Devices*. A look-up table of outputs for the DDS was created to trigger through the frequency states.

A low pass filter is used to suppress harmonics past 1,400 MHz. The characterisation of this is shown in figures 4.13. An amplifier is used to deliver the signal to both inputs of the first IQM at 19 dBm. A separate 25 GHz source, a *dielectric resonator oscillator* (DRO), the *NXPLOS-I-2500* form *Nexyn*, is to be used for the Bloch operations. A *quality hybrid coupler* (QHC) is used to match the RF input to both ports of the IQM.

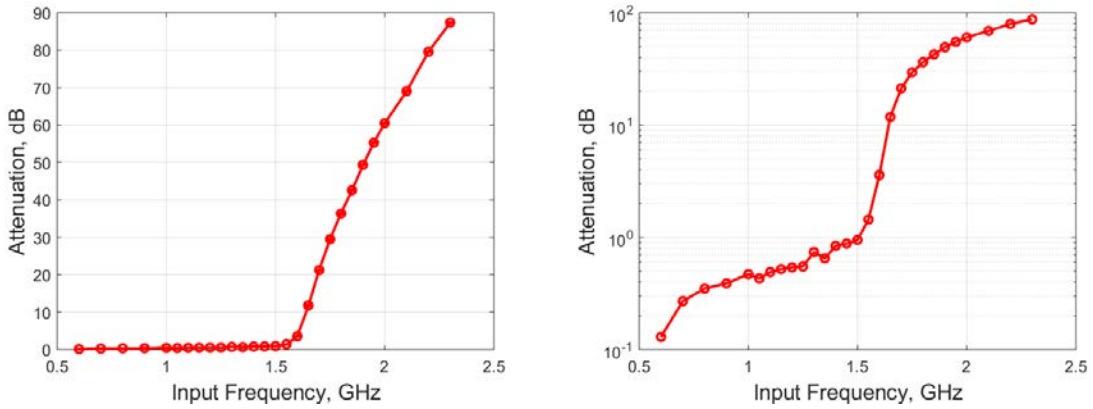

(a) Linear scale.

(b) Logarithmic scale.

Figure 4.13: Characterisation of the low pass filter used to attenuate higher harmonics of the desired frequencies.

The frequency generation for the second IQM requires subtraction from the 7 GHz source. This part of the chain is responsible for generating the repump and the two-photon detuning for the Raman process. Both of these, but especially for Raman Interrogation, require a very clean signal. Similar to the chain for the first IQM, the frequencies are generated through a frequency synthesiser and a DDS. The output of this is mixed with the 7 GHz source to produce the 6.629 GHz and 6.835 GHz for repump and interrogation

respectively. A switch is used to transfer between these two states, with band pass filters removing unwanted frequency components. The characterisation of these filters is shown in figure 4.14.

A second switch is used to be able to put the interrogation frequency into the microwave antenna for driving the transition directly. Another part of this chain is used to generate MHz frequency ramps for the Bloch process. Again, the power is balanced into the IQM and QHC's are used to provide a phase shift between inputs.

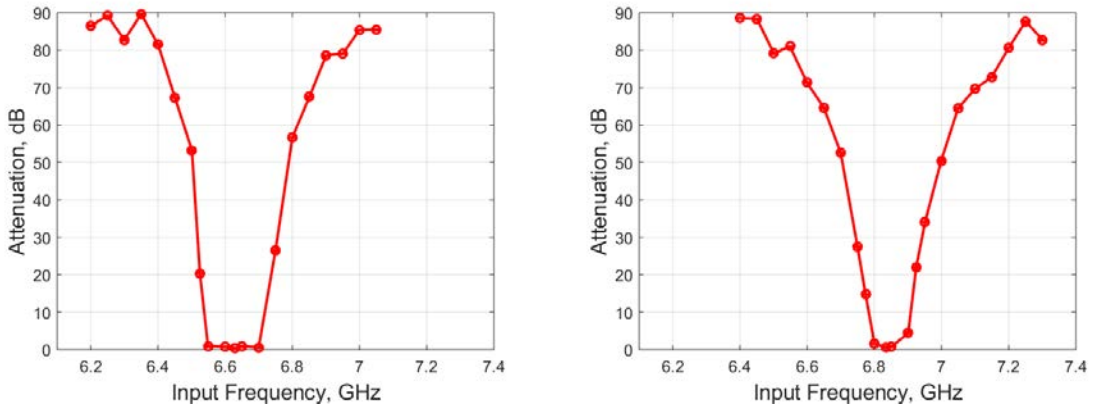

(a) Band pass filter, central frequency 6.629 GHz. (b) Band pass filter, central frequency 6.835 GHz.

Figure 4.14: Characterisation of the band pass filters used to attenuate any frequencies that are undesired.

A frequency synthesiser is used to generate the 80 MHz for driving the AOM. This passes through a VVA to control the amplitude of the optical power of the AOM, while a switch is used to realise fast switching on and off. The response of the VVA to input voltage is non-linear, the characterisation is shown in figure 4.15a. The VVA input is controlled by a DAC output of a FPGA. To understand the function of the system as a whole, the response of the AOM to the command given to the FPGA is characterised. This is shown in figure 4.15.

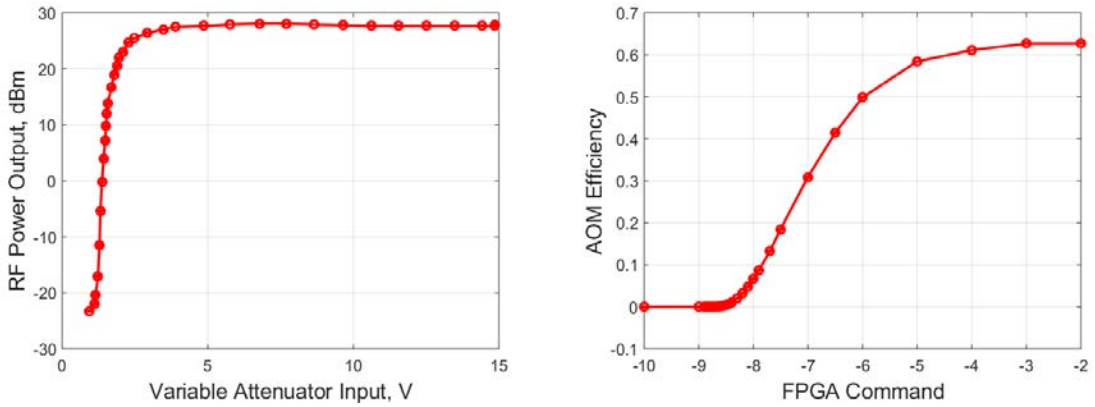

(a) Response of the VVA to the input voltage. (b) Response of the AOM to FPGA command.

Figure 4.15: Response of the whole system consisting of the FPGA controller, DAC, VVA and AOM. We characterise the behaviour of the AOM with different commands sent to the FPGA. There is a software interface to the FPGA where values between 0 and -10 can be input which correspond to the voltage into the variable attenuator.

The pulses for interrogation are on the order of microseconds long. The light needs to be able to be switched on and off on this timescale, ideally at 0.1 μs. To achieve this a *ZASWA-2-50DR* RF switch from *mini circuits* is used in the chain of the AOM. This is capable of switching in 30 ns, as can be seen in figure 4.16.

With the system described in this section a microwave chain capable of driving the necessary frequency pairs for cooling, interrogation, Bloch oscillations and detection in a single arm laser is possible. In the following section the design principles and processes to package the laser and microwave chains into low SWaP forms is presented.

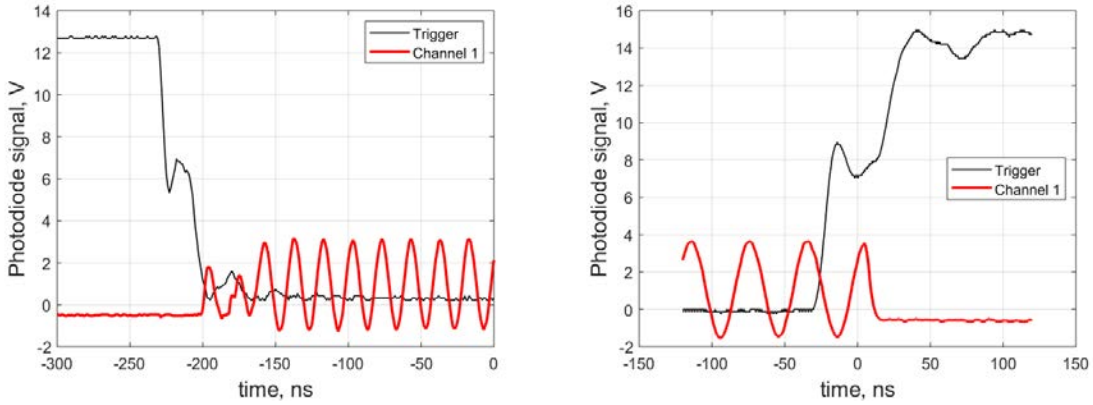

(a) Switching on.

(b) Switching off.

Figure 4.16: Characterisation of the RF switch used to quickly turn on and off the AOM (*ZASWA-2-50DR*). The red trace shows the 80 MHz oscillation being switched on and off respectively.

4.4 Compact Packaging

To ensure the sub-systems described above fit into the overall SWaP criteria of the system, some work was put into designing low volume but practical packaging. The design criteria for the packaging was to keep everything below the height constraint of 460 mm. Each box was specified to have a volume less than 10 L and weight less than 5 kg, yet still be accessible for maintenance and testing.

The approach taken for this packaging is to have separate boxes for the optical (fibred) chain and the microwave chain. This is to separate and manage the heat load effectively. All of the fibres are in one package and isolated from the RF amplifiers which are the largest heat source. The changing of ambient temperature this would cause in the laser system could result in frequency and polarisation changes. In order to have very few interfaces between boxes, only three SMA connections are used (for the IQMs and the AOM).

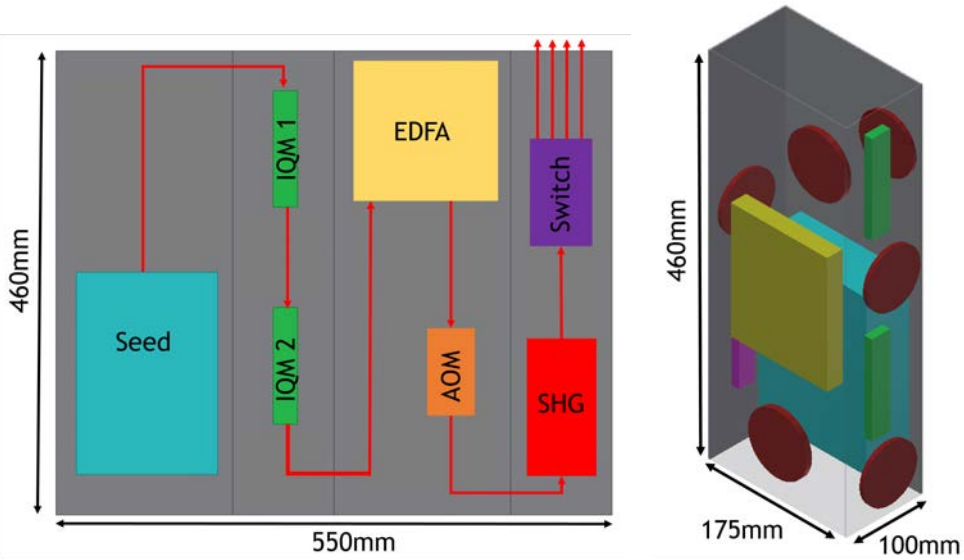

(a) Layout when open.

(b) Layout when closed.

Figure 4.17: Diagrams of how the components will be laid out in the laser box. Also shown is how the laser box can fold for a more convenient volume footprint.

When working with fibred systems, it is useful to have everything laid out flat to work on. It is important to be able to clearly see the fibre connections and take care when handling fibres, a clearly laid out "plate" is very useful for this. To set up the optical box the components were laid out in a linear fashion, following the path of the light. This made the most sense in terms of fibre management. However, a single flat plate is not easily packaged into a small form factor. Therefore, the concept of a folding box was used. When being worked on, the box can be unfolded into a plate. When folded up, the package can be very spatially efficient. This concept can be seen in figure 4.17 and the implementation in figures 4.18, 4.19.

The RF box was set up to allow the best use of the available volume, with all of the components that need thermal management on the same wall. The electrical wires in this box are more rugged than optical fibres; the greater consideration is placement of connections and thermal management. The construction of the microwave chain package can be seen in

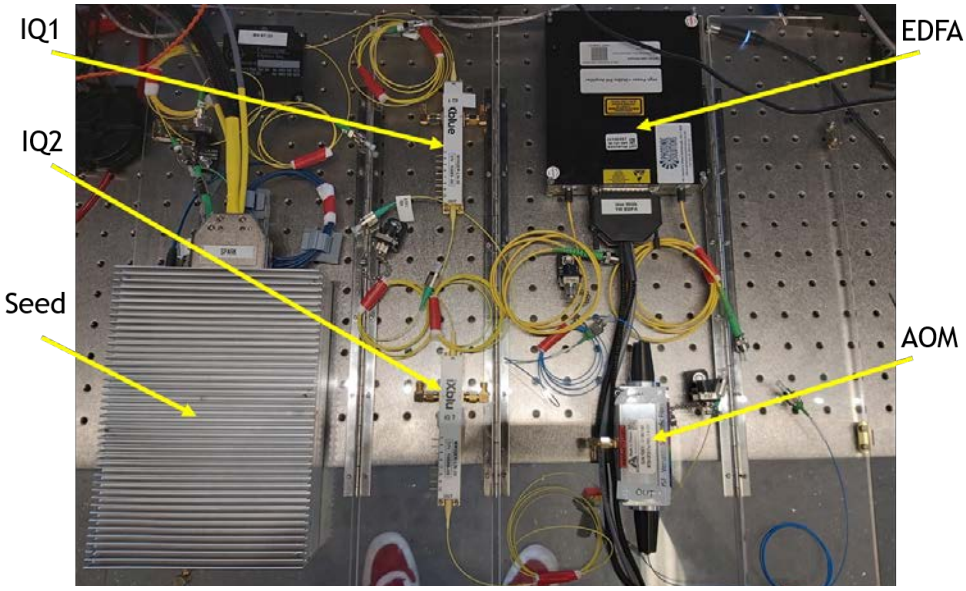

Figure 4.18: Photograph of laser box during assembly. Not all components are present.

figures 4.20, 4.21.

4.5 Summary

A complete laser system including a single arm laser, frequency generation and locking has been designed and produced. This is capable of performing full atom interferometry experiments being agile and easily reconfigurable. This system has been filed for patent [90]. It meets the requirements set out in table 4.2. Such a system could be easily adapted to work with a multitude of cold atom experiments that require portability and compactness. The system fits in a volume of 18.4 L, weighs 10.2 kg, and consumes 97 W. The budget and sub-system break-down are given in table 4.3. With a uniquely compact, robust and practical design, this laser system and microwave chain provide a direction for future generations of portable cold atom experiments and quantum sensors.

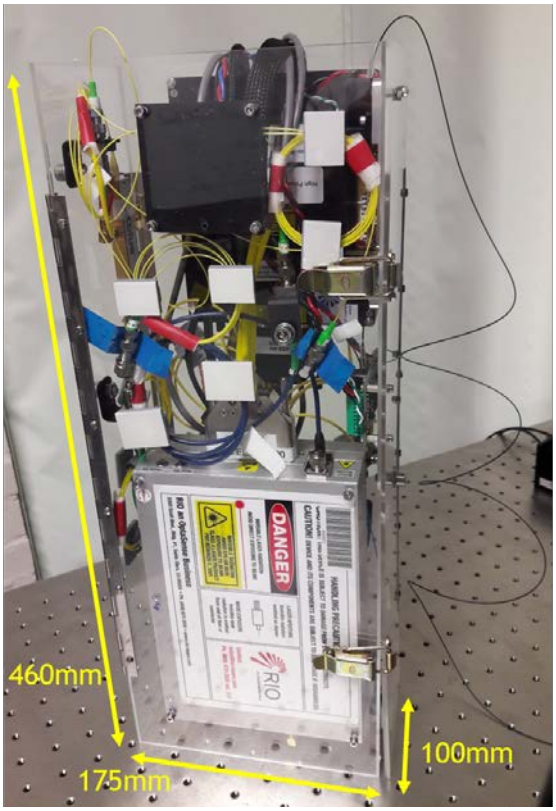

Figure 4.19: Photograph of laser box when closed for optimum volume. The system has a volume of 9 L, weight of 4.5 kg and total power consumption of 30 W.

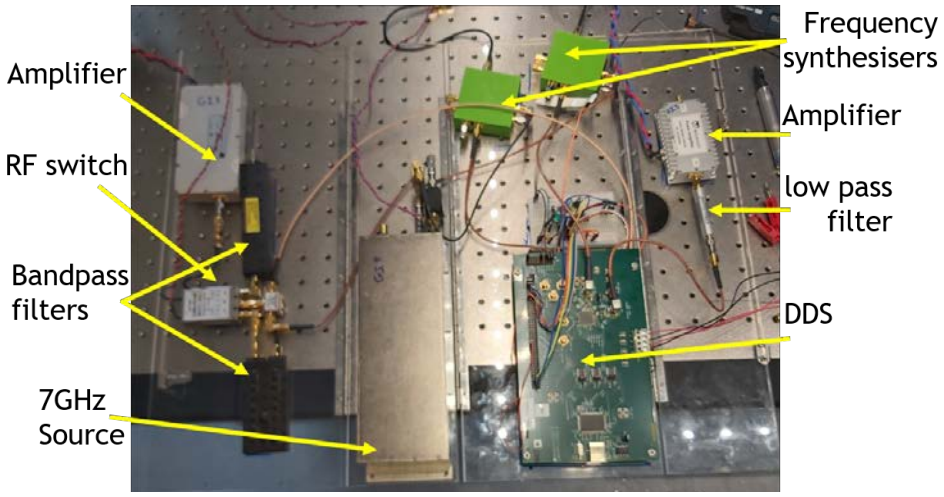

Figure 4.20: Photograph of RF box during construction.

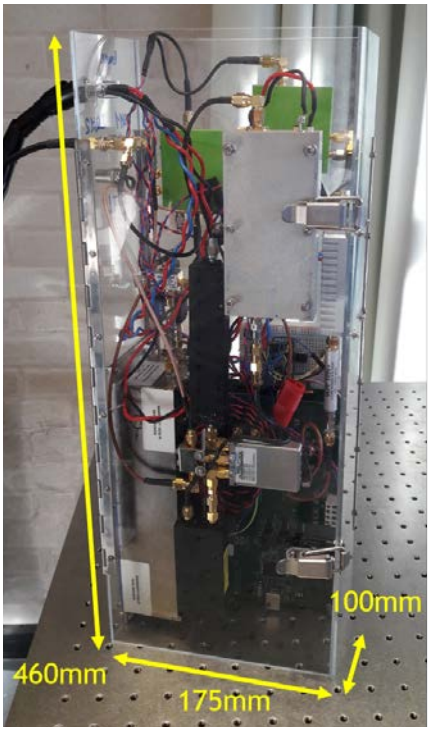

Figure 4.21: Photograph of RF box when closed for optimum volume. The system has a volume of 9 L, weight of 4.4 kg and total power consumption of 67 W.

Table 4.3: A breakdown of the size, weight and power (SWaP) budget for the laser system and how the sub-systems contribute to this.

	Size	Weight	Power
Total Budgeted	<20 L	<8 kg	<100 W
Total Current	18.4 L	10.2 kg	97 W
Laser Box	8 L	4.5 kg	30 W
RF Box	8 L	4.4 kg	67 W
Lock Box	2.4 L	1.3 kg	N/A

Chapter Five

Atom Optics

The work of this thesis aims to demonstrate the principles of a person portable gravity sensor based on atom interferometry techniques. Chapters 3 and 4 detail the design and construction of sub systems which make this goal achievable. This chapter will cover the procedures and experiments performed to show the successful demonstration of the system as a gravity sensor. These experiments use the atomic physics techniques outlined in chapter 2.

Specifically, this chapter will first outline the method for measuring and optimising the MOT characteristics. The key parameters are the number of atoms present in the MOT and the characteristic temperature of the ensemble. The procedure for an optical molasses (2.2.2) will be described, as well as two techniques for determining the temperature. Additionally, a method for a single shot, comparative measurement of both ground state populations will be presented. This improves the measurement process for atom interferometry. Characterisation of the affect of the microwave pulse will be presented, for future use as a state selection tool. Finally, characterisation and results will be presented for different atom interferometry schemes.

5.1 Atom Preparation

5.1.1 MOT Characterisation

The successful production of a MOT and characterisation of it demonstrates the success of the vacuum chamber, the stability and the frequency control of the laser. Without all of the subsystems working correctly, it would be impossible to produce and characterise the MOT. The precision of any atom interferometry measurements performed will depend on the signal to noise ratio of the atoms detected. This is based on the Poissonian statistics of the atom number. Generally, the higher the atom number the better the signal to noise ratio and hence, measurement precision.

Another aspect to consider is the lifetime of the MOT. The ultimate aim of the atom preparation is to produce as many atoms at a sufficiently cold temperature as possible. The more atoms released from the dispenser, the more atoms able to be captured in the MOT. However with more atoms released, the higher probability that atoms not in the MOT will interact and eject MOT atoms, reducing the lifetime of the MOT. Therefore a trade-off is presented between the MOT atom number and the lifetime of atoms in the MOT.

Atom Number Measurement

The atom number present in the MOT can be calculated from the light collected from the fluorescence of the MOT atoms. The light is detected by a photodiode sensitive to the correct wavelength (780 nm), observing the MOT region. The atom number is measured while the cooling light and trapping magnetic field are on. The atoms in the MOT scatter photons from the cooling beam. This light passes through a viewport and is focused onto the photodiode using a lens. The apparatus is shown in figure 5.1.

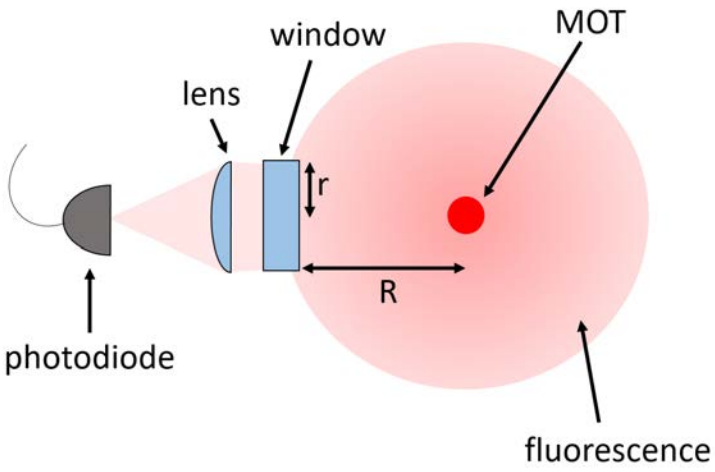

Figure 5.1: A diagram showing how MOT number measurements were performed. With the cooling light and trapping magnetic field on, the MOT atoms scatter cooling beam photons. This fluorescence is collected by use of a lens onto a photodiode.

The signal produced on a photodiode can be related to the number of atoms through the scattering rate and some optical and electrical signal conversion coefficients. By knowledge of the relationship between the number of incident photons and the voltage signal, the fraction of photons being detected of the the total emitted, and how many photons each atom scatters, the number of atoms can be calculated. The calculation follows that summarised by Steck [55]. The scattering rate is calculated from the transition linewidth, Γ, the detuning from the transition, δ, and the cooling light intensity, I:

$$R_s = \frac{\Gamma}{2} \frac{\frac{I}{I_{sat}}}{1 + \frac{I}{I_{sat}} + (\frac{2\delta}{\Gamma})^2} \ , \tag{5.1}$$

where I_{sat} is the saturation intensity ($I_{sat} = 1.67$ mW cm^{-2}). The cooling intensity used during the measurements was $I = 8.43$ mW cm^{-2} (averaged over the beam). The linewidth of the D2 cooling transition is $\Gamma = 6.066$ MHz and the detuning $\delta = 2.5 \times \Gamma$.

The fraction of photons which reach the photodiode out of the total produced is

calculated using the solid angle. As the scattering of photons from the MOT is isotropic, it is convenient to reference the geometry to a sphere. The total sphere of emission is 4π *steradians*. The amount of light incident on the viewport is given by the solid angle $\Omega = \pi r^2/R^2$ where $r = 6.35$ mm and $R = 35$ mm are the radius of the viewport and the distance from the MOT to the viewport respectively. Hence, the fraction of light collected is $\alpha = r^2/4R^2 = 0.8\%$.

Finally, the detector efficiency must be considered. The *responsivity* of a photodetector links the photo-current produced to the incident power. For the detector used (*Thorlabs DET36A/M*) the responsivity at 780 nm is $R_e = 0.47$ A W^{-1}. By multiplying by the energy carried by each photon, $E = hc/\lambda$, a measure of the photo-current produced per photon per second is obtained. It is convenient to convert the current to a voltage by multiplying by the resistive load used, a 1 MΩ oscilloscope (Ω in equation 5.2). The photon to voltage efficiency of the detector is thus $Q = R_e hc/\lambda$. With all of the elements a conversion between the voltage signal measured by the photodiode, V, and the atom number, N, is obtained:

$$N = \frac{1}{R_s \alpha Q \Omega} V \ . \tag{5.2}$$

MOT Loading Characterisation

The following measurements use the atom number detection and conversion method described in section 5.1.1. The measurements concern the loading of atoms into the MOT. The MOT is loaded by switching on the trapping coils. The *loading curves* are taken while varying first the dispenser current and then the current through the trapping coils. This is done to optimise the trade-off between the atom number trapped and the lifetime of the MOT. A long MOT lifetime is indicated by a longer loading time, the time taken to reach the maximal atom number [91]. A well optimised MOT will push to the optimal loading time

for a given interferometer time and free-fall distance. This will put the maximum amount of atoms through the sequence per unit time. More background pressure will lead to losses in the interferometer part of the sequence, less will lead to loading fewer atoms in the first place.

First, the relationship of the MOT loading to the dispenser current is investigated. This is shown in figure 5.2. The maximal atom number is achieved with high dispenser currents (3.4 A). However, the higher the dispenser current, the shorter the MOT lifetime. Another feature seen in figure 5.2 is that the higher current values saturate the atom number scale. To balance a long lifetime and high number, a dispenser current of 3.0 A is used. This gives a loading time of 5 s and an atom number of $\sim 4.4 \pm 0.5 \times 10^8$.

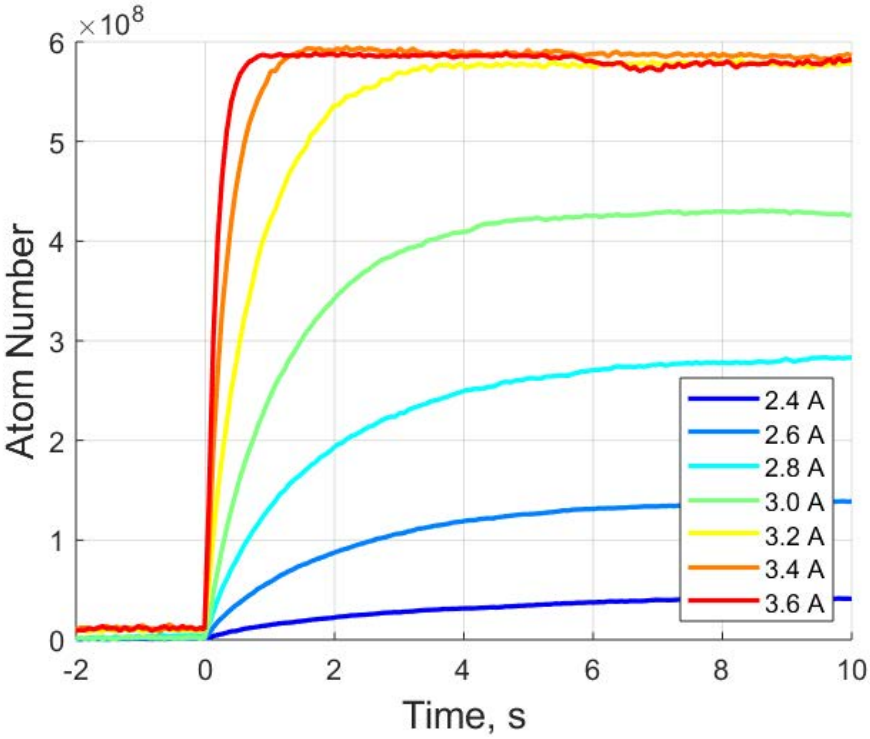

Figure 5.2: MOT loading curves with varying dispenser current.

Next, the relationship of the MOT loading to the trapping coil current is investigated. This is shown in figure 5.3. This shows that at both sub-optimal and super-optimal current

values the atom number is low. The loading time is generally unaffected however. At low current values, the trapping force is insufficient to maintain high atom numbers. At high current values the *trapping volume*, the volume in which atoms can be trapped, is too small to have a high atom number. Therefore, a coil current of 2.0 A is used as it produces an optimised atom number of $\sim 4.5 \pm 0.5 \times 10^8$. The measured atom numbers and loading times for the MOT are sufficient for this work. After state and velocity selection (to produce a well defined, low temperature ensemble), a significant number of atoms ($\sim 10^5$) will contribute to the interferometer.

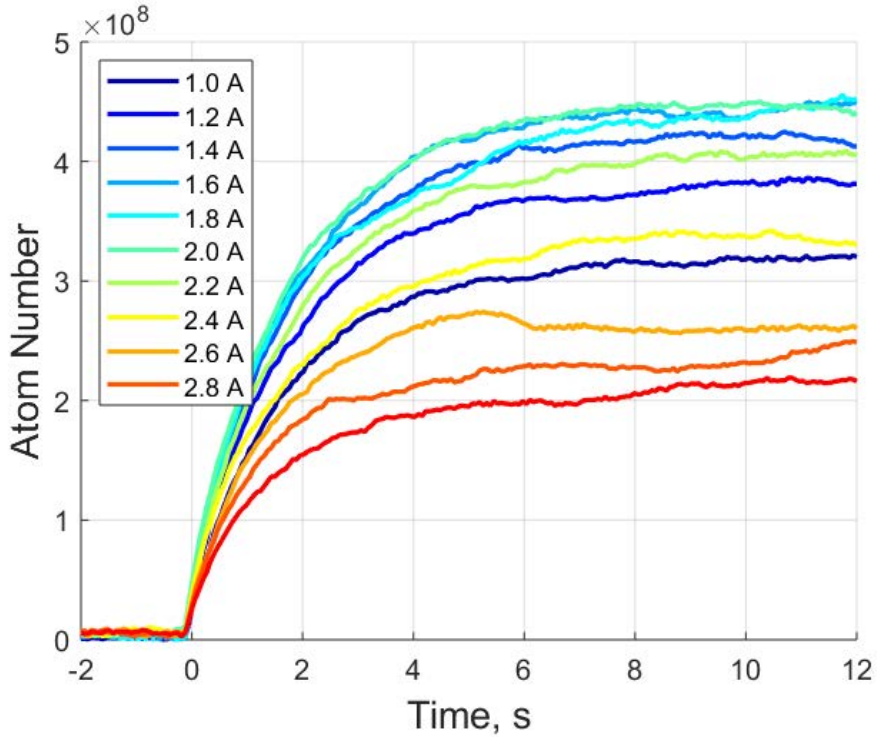

Figure 5.3: MOT loading curves with varying coil current.

5.1.2 Optical Molasses

Sub-Doppler Cooling Sequence

As described in section 2.2.2, in order to have a low temperature atomic ensemble, sub-Doppler cooling processes must be used. For this the trapping magnetic field is switched off, the optical friction force is known as optical molasses. In this process the damping coefficient is independent of optical power but the capture velocity is proportional to power [54]. Hence, the cooling intensity is gradually reduced. This is to match the capture velocity to the reducing temperature of the cloud. Simultaneously the detuning is reduced as at large detuning the equilibrium temperature depends inversely on detuning.

The exact parameters are optimised in the experiment. The sequence used in this work, along with the key parameters, are shown in figure 5.4. The cooling light is completely switched off for a few milliseconds after the MOT coil is switched off. This is to avoid eddy currents in the coil giving rise to unwanted forces on the atoms. While optimised, the sensor head was not inside the magnetic shields. Compensation coils were used to provide a null magnetic environment. The repumper can be switched before the end of the process to allow the atoms to populate the $F = 1$ ground state.

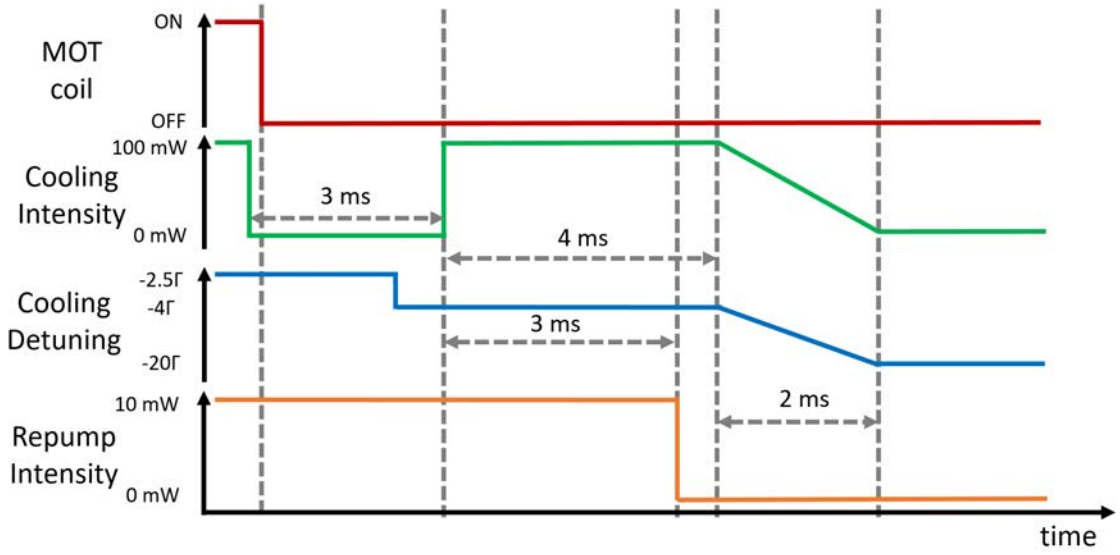

Figure 5.4: Diagram of the control sequence used in the optical molasses stage. The MOT coil is off to allow the optical sub-Doppler cooling process. The cooling intensity and detuning are gradually reduced to adiabatically cool and release the ensemble.

Expansion Capture Temperature Measurement

A method for measuring the temperature of the cloud is to image the cloud as it expands and fit the extent to a Gaussian ballistic expansion. The cloud is imaged using a triggerable camera. A short (100 μs) pulse of the interrogation beam is used to cause the cloud to fluoresce while minimising heating and changes in cloud size. The camera is triggered to capture the cloud extent at various times after the end of the optical molasses stage. Examples of these images are shown in figure 5.5.

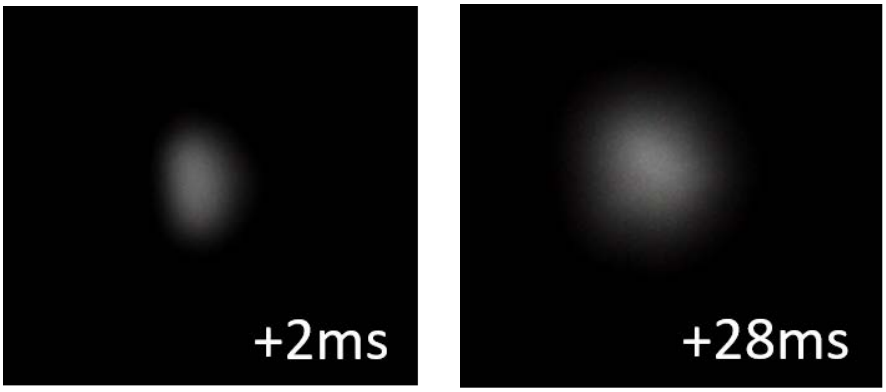

(a) Cloud extent after 2 ms. (b) Cloud extent after 28 ms.

Figure 5.5: Fluorescence images of the MOT after a free expansion time.

A vertical slice through the intensity values of these images was taken. The vertical temperature is most important as the interrogation is vertical. The *full width at half maximum* (FWHM) of a Gaussian fit of these slices is used to measure the extent of the cloud at each snap shot. The temperature of the cloud can be determined by fitting the extent of the cloud to equation 5.3. The size of the cloud, σ_f, at time t is found from the initial size, σ_i, and the velocity of the atoms, σ_v,

$$\sigma_f = \sqrt{\sigma_i^2 + \sigma_v^2 \times t^2} \tag{5.3}$$

$$= \sqrt{\sigma_i^2 + \frac{k_B.T}{m_{Rb}} \times t^2}\ . \tag{5.4}$$

The velocity spread of the atoms is related to their temperature, T, through the atomic mass, m_{Rb}, and the Boltzmann constant, k_B. The sizes of the cloud (from the FWHM) at certain times are plotted in figure 5.6, along with a fit of equation 5.3. From this fit a measurement of the cloud temperature is obtained to be $T = 7\ \pm\ 2\ \mu$K.

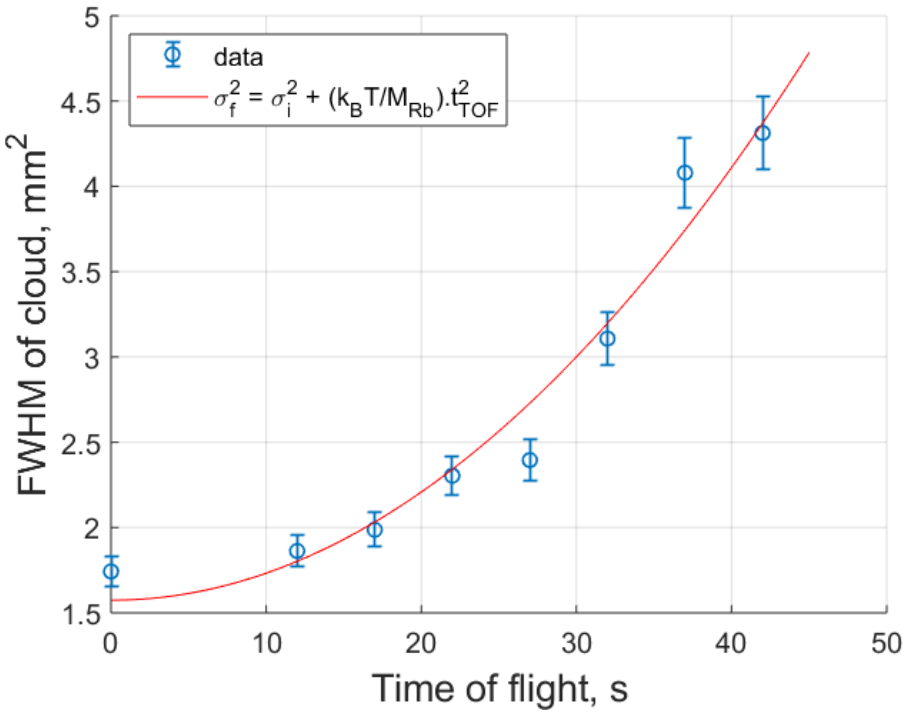

Figure 5.6: Measurement of the atomic ensemble extent with free expansion time. Each data point represents a single shot measurements of the FWHM of the cloud extent taken from fluorescence images (figure 5.5). The error bars come from uncertainty in fitting a Gaussian to the fluorescence image. The fit to the data points is for equation 5.3, from which the cloud temperature can be determined as $T = 7 \pm\ 2\ \mu$K.

Light Sheet Temperature Measurement

Another method for calculating the temperature of the cloud is to measure its extent using a *light sheet*. A light sheet is a thin plane of retro-reflected light. When the atom cloud falls through this sheet, the atoms will fluoresce. A photodiode can be used to detect this fluorescence. The Gaussian distribution of atoms in the cloud will be projected onto the time domain as the cloud falls through the sheet. The principle is shown in figure 5.7. The light sheet is created by placing a mask in front of a collimator, with a 0.5 mm slit.

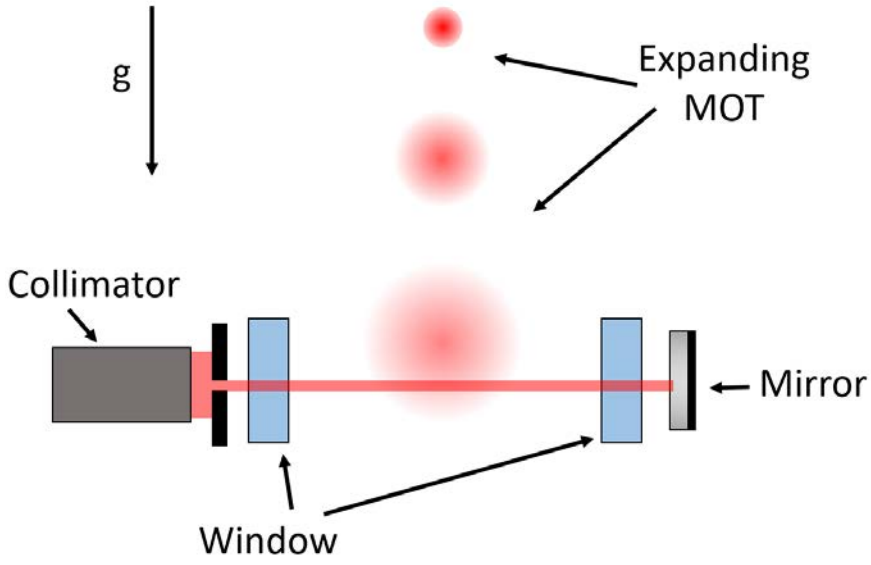

Figure 5.7: Diagram of how light sheet measurements were performed. The light sheet is created by placing a mask with a 0.5 mm slit in front of a collimator, which is then retro-reflected by a mirror. The reflection reduces the effect of the atoms being blown away. The spatial Gaussian distribution of the atoms is projected onto the time domain as the cloud falls through the sheet. The photo diode for detection is out of the page.

A Gaussian fit can be made to the detection peak, seen in figure 5.8. From this the FWHM of the signal is found and converted to the spatial domain using the velocity of atoms at the light sheet. The final extent of the cloud is calculated as 9.2 ± 0.2 mm. Using equation 5.3 and taking the initial cloud size from the image capture, the temperature is calculated as $T = 5 \pm 2$ μK. This result is in good corroboration with the image capture method. Further, the light sheet signal can be summed to calculate the atom number. The detection and conversion from a photodiode is very similar to that described in section 5.1.1, but now also including the time each atom spends in the light sheet. Through this method, the atom number is calculated as $3.6 \pm 1.0 \times 10^8$, which is good agreement with the initial MOT atom number measurements (section 5.1.1). The temperature measured in both ways

is lower than the target of 10 μK, this enables a low velocity class of atoms to be selected for participation in the interferometer.

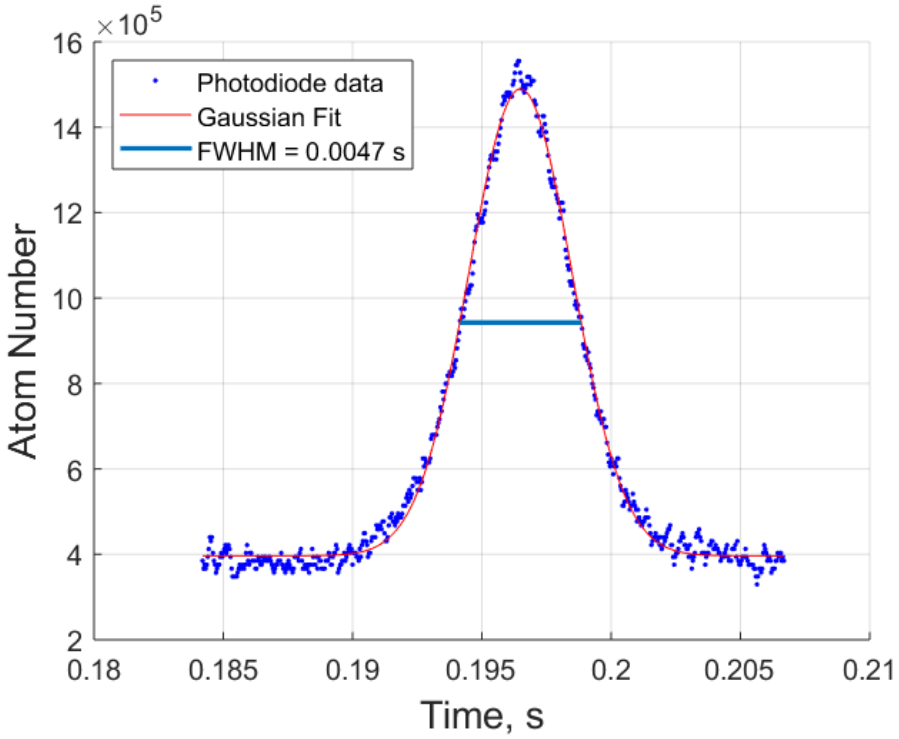

Figure 5.8: Measurement of the atomic ensemble through a light sheet. This measurement is from a single shot.

5.1.3 Bi-State Detection

While the light sheet detection method is suitable for temperature and atom number measurements, only a single state can be detected per shot (with the apparatus as described in section 5.1.2). For atom interferometry measurements, where the relative population between the two ground states is significant, a different technique is used. This *bi-state* detection method allows the relative populations of both ground states to be measured in each shot. Due to the setup of the laser system (chapter 4), it is possible to probe the $F = 2$

state singularly and the combined total of $F = 1$ and $F = 2$ states. By comparison of the population measured in $F = 2$ and that measured in the total of both a comparative measure of the population, independent of starting atom number, is possible. To achieve this, a broad (18 mm diameter) beam is used to probe the falling cloud, with the frequencies changing between multiple short (20 μs) pulses. A beam block is used to allow blow-away of the atoms and obtain a signal of just the detection light, the schematic can be seen in figure 5.9.

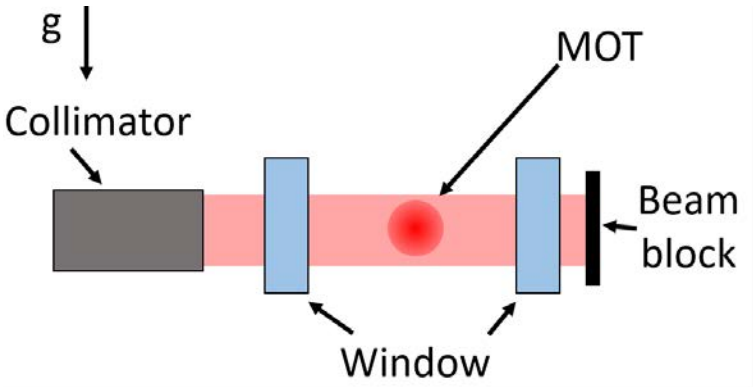

Figure 5.9: Diagram of how bi-state detection measurements were performed. An 18 mm diameter beam is used to probe the falling cloud. Multiple short (20 μs) pulses with different frequency components are used to interrogate different states. The beam block is used to allow blow-away of atoms. The detector is out of the page.

The pulse sequence used allows subtraction of the light pulses from the atom contribution to the signal. The first pulse (20 μs) addresses the $F = 2$ state atoms only. The second pulse (also 20 μs) addresses both $F = 2$ and $F = 1$ populated atoms through inclusion of the repump side-band. The third pulse is used to blow-away all the atoms, addressing both states. Finally, the last two pulses copy the first two and are used to subtract the light contribution to the signal. The blow-away is used to remove atoms from the measurement in order to subtract the light signal. An idealised example of the measurement, with annotation

of the pulses is shown in figure 5.9. Examples of measurements taken using this detection scheme are given in figures 5.11 and 5.12. Figure 5.11 depicts the atomic populations at the end of a drop after being prepared at the molasses stage in state $F = 2$ by continual use of the repump.

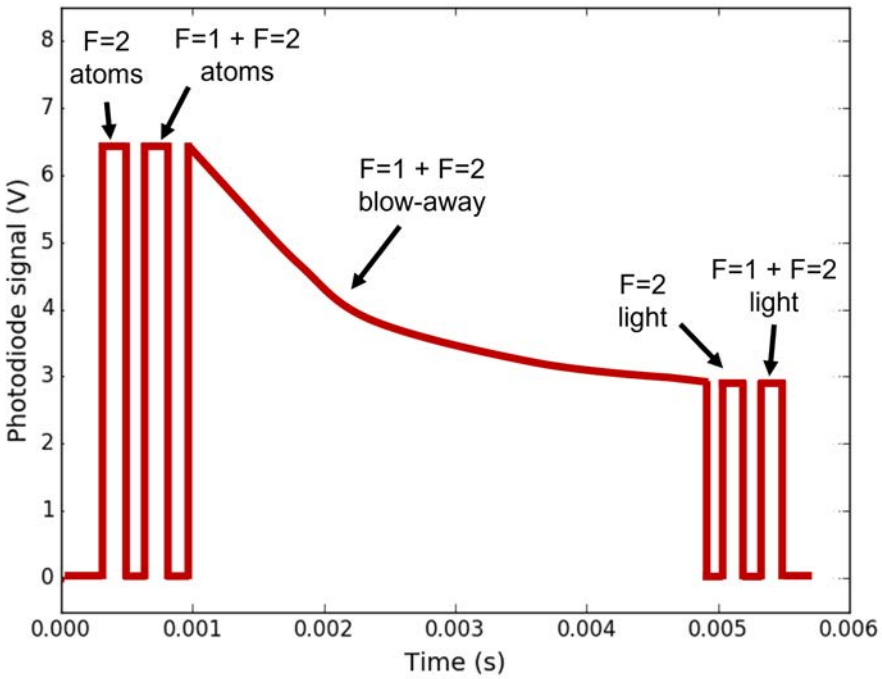

Figure 5.10: Idealised diagram of bi-state detection, with annotations of the pulses.

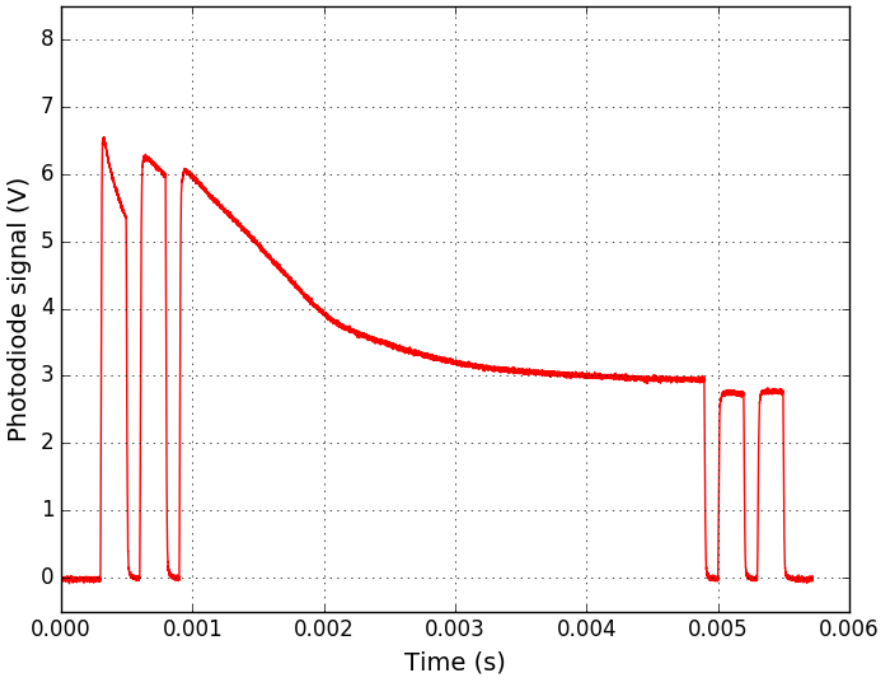

Figure 5.11: Measurement of the atom population using bi-state detection. The first peak contains the contribution of $F = 2$ atoms while the second peak contains that of both $F = 1$ and $F = 2$ atoms. Here the repump is left on, hence nearly all the population is in $F = 2$. During the first detection pulse, as the repump is off, atoms will depopulate to the $F = 1$ state. These are then detected again in peak two where the repump is on again.

Figure 5.12 depicts the detection peaks observed when the atoms are prepared at the molasses stage with the repump off for 3 ms before the end. This drives most of the population into the $F = 1$ state as they are no longer pumped out into the cooling cycle, as described in section 2.2.1. Finally, a blow-away pulse is used for atom preparation. This is a short (100 μs) pulse of $F = 2$ light directly after the molasses stage. This is used to remove any $F = 2$ atoms from the ensemble. Having a pure state is crucial to detecting atomic transfer between states. Any presence of unwanted states in the initial ensemble will result in a loss of contrast.

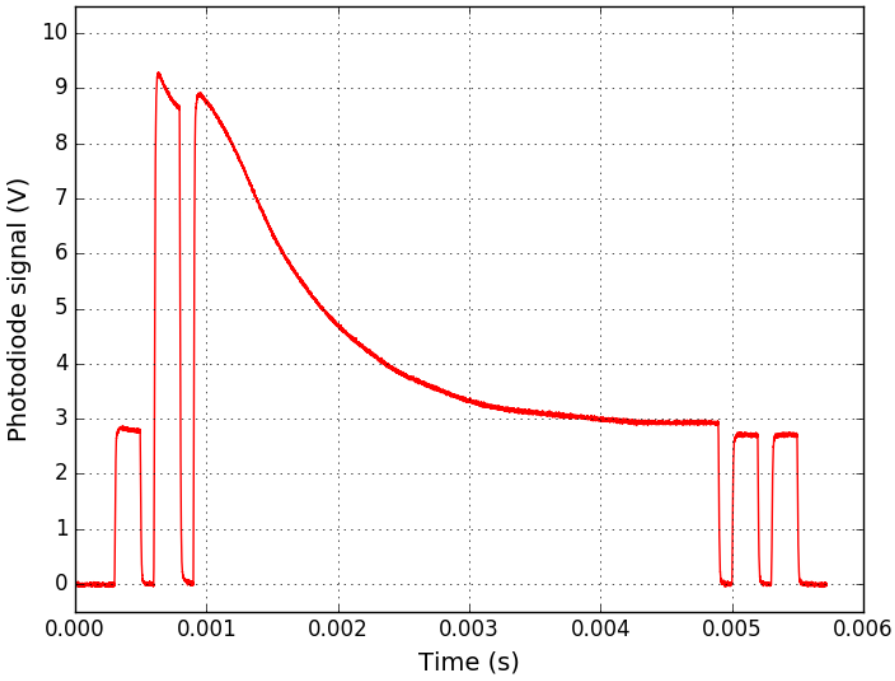

Figure 5.12: Measurement of the atom population using bi-state detection. The first peak contains the contribution of $F = 2$ atoms while the second peak contains that of both $F = 1$ and $F = 2$ atoms. Here the repump is turned off before the end of the sequence, transferring nearly all the population to $F = 1$ so nearly no atoms are detected in the first peak.

5.1.4 Magnetic Sub-Level Selection

Beyond the initial atom state preparation, the atoms can be prepared in a particular magnetic sub-level. The predominant reason for this is to cleanly select a magnetically insensitive sub-level, $m_F = 0$. By only transferring atoms in this sub-level, the contrast of the interference fringes will be better. In this work, a microwave pulse is used to directly transfer the atomic population while a bias magnetic field is used to lift the magnetic degeneracy. Details on the bias field used can be found in section 3.15. Directly after the molasses stage (where the

coils are in a compensation configuration) the vertical coils are switched to provide a bias field which extends the vertical height of the vacuum chamber. The atoms will naturally populate all sub-levels. Through combination of the bias field, the microwave pulse and a blow-away, there can be atoms only populating the $F = 1, m_F = 0$ state. This however does remove either $2/3$ or $4/5$ of the atoms from the process, depending on initial state. The sub-levels, magnetic perturbation and microwave transition are all displayed in figure 5.13.

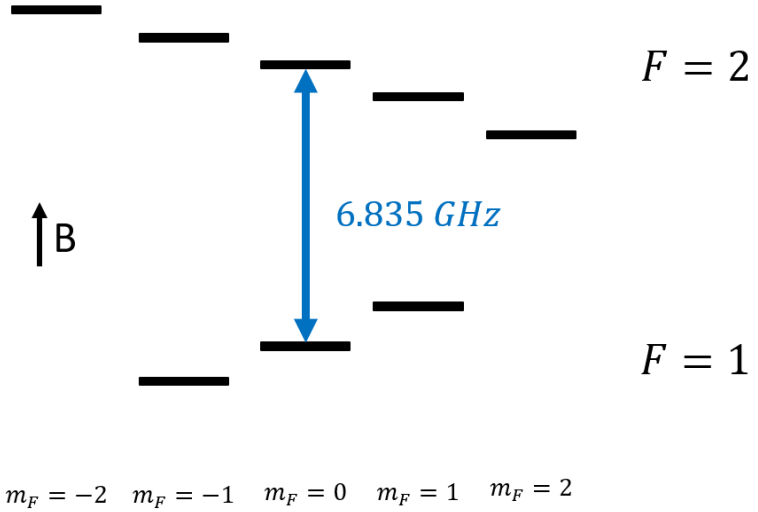

Figure 5.13: Diagram of the degeneracy lifting of the magnetic sub-levels of the ground states in the D_2 line of ^{87}Rb and the transition driven by the microwave pulse.

The microwave pulse is characterised for future use. The atoms are initially prepared in the $F = 1$ state as in figure 5.12. The microwave is then applied for varying amounts of time to produce a Rabi oscillation measurement. In figure 5.14 each data point is a single shot with a different pulse time. The population is transferred from state $F = 1$ to $F = 2$, reaching a maximum transfer at 0.13 ms pulse duration (the π time). It is noted that the maximum population fraction is 0.2. The atoms initially populate the three sub-levels of the $F = 1$ state equally so only $1/3$ will be addressed by the microwave pulse when the bias field is applied.

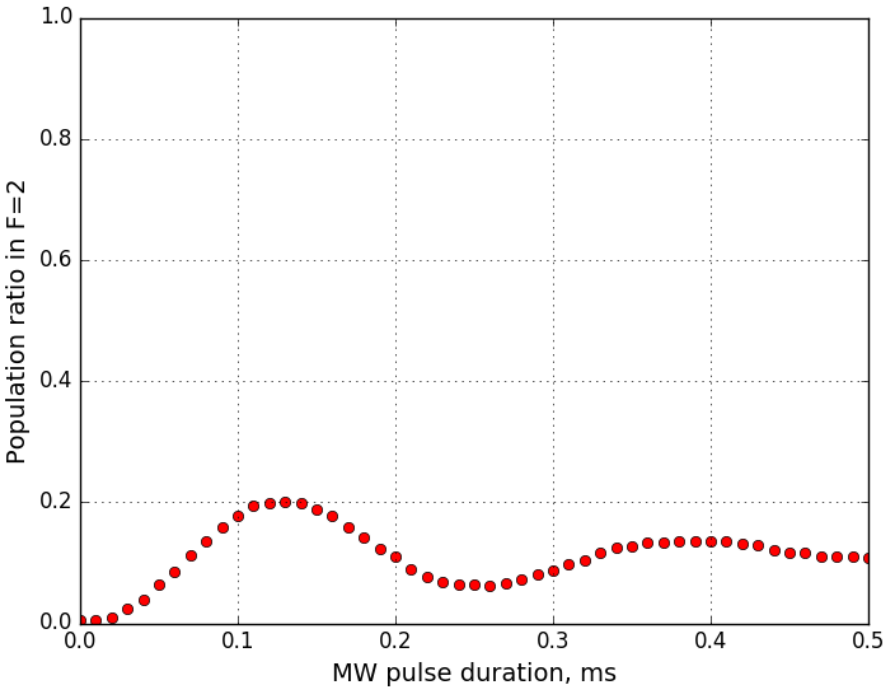

Figure 5.14: Measurement of a Rabi oscillation with a microwave pulse. The π pulse length is 0.13 $\pm$ 0.01 ms.

5.2 Optical Transitions

5.2.1 Rabi Oscillation

The operation of optical Raman transitions demonstrates that the system is capable of performing everything necessary for atom interferometry measurements. In this experiment the vertical laser beam is used to coherently transfer population between the two ground states. This is very similar to the microwave Rabi oscillation described in section 5.1.4, however the transition is a two-photon Raman transition (see section 2.2.3). The two frequency components are both present in the laser beam incident vertically from the top of the chamber (section 3.4.2). The beam is blocked at the bottom of the chamber meaning

only co-propagating transitions are driven. Although less momentum is transferred, this technique is less velocity-selective so is useful for initial frequency optimisation. An example of an optical Rabi oscillation using Raman transitions is shown in figure 5.15.

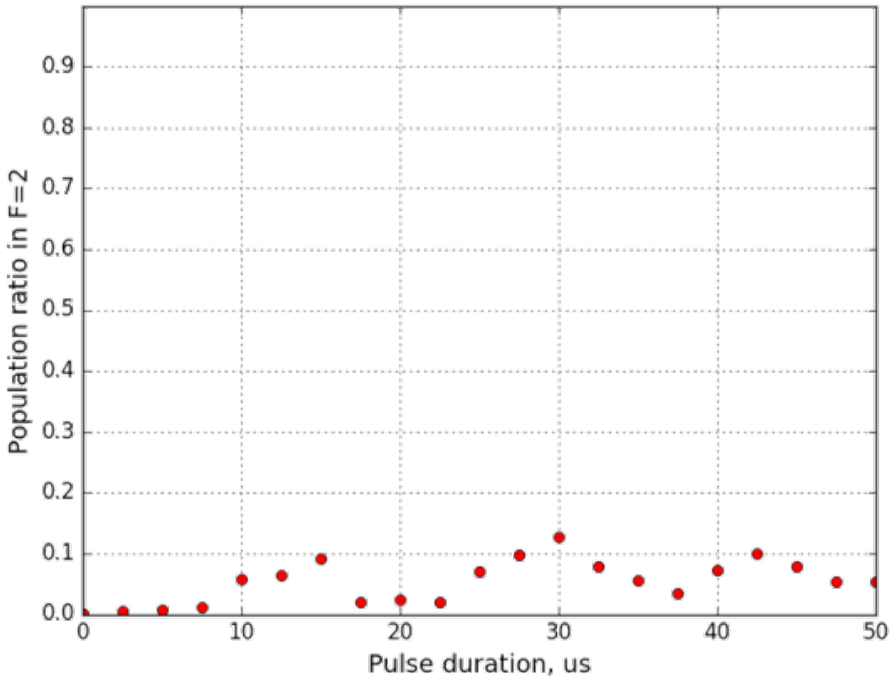

Figure 5.15: Measurement of a Rabi oscillation using an optical Raman transition. The beams are in co-propagating configuration. Each measurement point corresponds to a single shot. While the ensemble is in free-fall, the laser is pulsed on for a time, each shot corresponding to a different pulse length. It should be noted this is an initial measurement and the process needs to be optimised. The π pulse length is $\sim$ 8 $\pm$ 3 μs, measured from the first trough to the second peak. There seems to be an artefact at the start of measurement which could be due to a switch delay.

5.3 Summary

This chapter described some initial experiments to verify the operation of the system produced. Through demonstration, characterisation and analysis of atomic physics processes, the sub-systems and system integration is shown to work as designed. Firstly, a magneto-optical trap is produced and characterised. Measurements of the atom number and temperature demonstrate the success of the vacuum chamber and the laser system. Without a stable and tuneable laser, a cloud of $T = 7 \pm 2\ \mu$K would not be possible.

Next, coherent transfer between the two ground states of the $^2S_{1/2}$ level in rubidium 87 was shown. This was achieved with both microwaves and a two-photon Raman transition. The operation of the microwaves demonstrates the bi-state detection method as well as the ability to perform state preparation. The operation of the optical Rabi oscillation shows that the laser system is capable of Raman transitions as well as cooling and detection. The next steps would be to optimise the optical Rabi oscillations, then demonstrate an interferometry sequence.

Chapter Six

Conclusion

6.1 Summary

The work presented in this thesis aimed to demonstrate the feasibility of a sensor based on quantum technologies for use in a field environment. Atom interferometry has enabled some of the most precise inertial measurements to date [12, 13], although these are typically bound to a laboratory. To make an impact in surveying, this technology has to be developed to work in a smaller package. An easily portable and sensitive gravity sensor could revolutionise sub-surface mapping of utilities pipes, sink-holes, mineral exploration and archaeology.

Already, much work has been performed to develop portable gravity sensors (detailed in section 1.3). Among these, there have been some promising examples of portable sensors using atom interferometry [1, 32, 35, 36, 38]. However, these are mostly aimed at moving platforms such as ships, planes and trucks. A common surveying sensor, the *Scintrex CG-6* [24], is popular largely due to it being easily person portable with a volume of 10 L and weight of 5 kg. The work of this thesis aims to push the limits of a portable gravity sensor using

atom interferometry to being comparable to the *CG-6*. This will allow the improvements offered by atom interferometry to be brought to end-users in an appropriate form factor. Not only this, the development of low SWaP sub-systems will enable other quantum technologies to be developed in robust and portable packages.

The work of this thesis in terms of developing low SWaP sub-systems for quantum technologies is summarised in table 6.1. The systems which require the most attention from a quantum technologies perspective are the sensor head and the laser system. In both instances this work has significantly improved the SWaP characteristics over current state-of-the-art experiments (summarised in section 1.2). In addition, a path towards quantum technologies being comparable with incumbent classical devices for field surveying has been demonstrated. Not only does atom interferometry show improvements over classical devices for gravity mapping, this work shows those systematic improvements can be developed in compact and robust packaging.

Table 6.1: A breakdown of the size, weight and power (SWaP) budget for the sensor and how the sub-systems contribute to this.

	Size	Weight	Power
Total Budgeted	<88 L	<20 kg	<100 W
Total Used	36.1 L*	17.6 kg	97 W
Sensor Head	14.1 L	7 kg	-
Laser Box	8.0 L	4.5 kg	30 W
RF Box	8.0 L	4.4 kg	67 W
Lock Box	2.4 L	1.3 kg	-
Power Supply	1.1 L	0.2 kg	97W
Control Computer	2.5 L	0.2 kg	-

Chapter 3 details the design process of the sensor head which enables gravity gradiometry measurements using atom interferometry in a total volume of 14.1 L. To achieve this, novel techniques were developed and combined. Of particular note is the design of a scheme using the Bloch elevator to create two test masses from a single cold atom generation region (figure 3.5), allowing a projected sensitivity of 500 $\mathrm{E}/\sqrt{\mathrm{Hz}}$ in a short timescale and low SWaP package. The gravity gradient measurement is of interest, especially using atom interferometry, as it allows removal of sensor acceleration noise. This is beneficial for portable sensors in the field (see section 1.1.2).

The novel laser system developed for this work was outlined in chapter 4. This scheme utilises state-of-the-art opto-electronic components to enable a system with only a single arm capable of driving all relevant transitions for a rubidium-87 experiment. The use of two sequential in-phase quadrature modulators (IQM's) allows a dual frequency laser with both being independently adjustable. Together with a supporting signal generation system to drive the necessary frequencies, this constitutes an agile laser system which is packaged into two boxes of 4.5 kg and 8.0 L.

To date, the sub-systems described have been integrated into a whole system capable of atom interferometry measurements. In total, this system weighs 17.6 kg and has a volume of 80 L (the sub-systems cannot be trivially combined, they are packaged together into a weight distributive cylinder). Atom preparation techniques have been implemented and is capable of producing an ensemble of $\sim 1 \times 10^8$ ^{87}Rb atoms at 8 μK, in a magnetically insensitive $F = 1, m_F = 0$ ground state.

6.2 Future Work

While the initial design and construction of a low SWaP sensor has been realised in this work, there is huge potential to improve the sensitivity. This is both via optimisation of the sensor and introduction of new techniques. A key aspect of the design of the sensor head and sub-systems was the flexibility to incorporate new techniques and measurement schemes over the entire life-cycle. This is primarily observed in the agile laser system and the vacuum chamber with its myriad of measurement schemes.

A further step to improve the sensitivity of this and future devices would be to use large momentum transfer schemes [92]. This technique would not require any hardware changes to the sensor but could drastically improve the sensitivity by increasing the momentum splitting during interferometry sequences. As atom interferometry is a constantly evolving and dynamic field, new inventions are constantly being developed. For example, dephasing of the interferometer is a limit on sensitivity and implementing new techniques to minimise this is a key consideration. Over the life-time of this sensor, it is expected that new developments can be included to improve the sensitivity and maintain relevance.

Another potential improvement would be to implement a compact 2D MOT. This is a loading method which enables virtually no background gas in the primary chamber by feeding a thin flux of atoms directly into the MOT. Traditionally these are high SWaP so did not meet the design requirements for this work. However, if a novel design could be made to fit with the particular constraints of this system, it could provide a route to further improve the lifetime of the atomic ensemble.

Also, as mentioned in section 1.3.1, a likely use case for a portable quantum sensor is in conjunction with many small relative accelerometers. The atom interferometer would provide discipline for this network of higher measurement rate sensors. These low SWaP

devices, in a network with a portable atom interferometer, could combine the best of a precise, absolute sensor and the higher data rate of other sensors. A promising companion technology for this is the MEMS sensors [30].

No matter the potential improvements to be made over the course of this sensors life, the next important step will be the demonstration of operation in a field environment. Firstly, this will aim to perform operation outside of the laboratory and display ease of portability. Next will be the detection of a relevant target in the field. This will likely require the measurement of a gravity signal difference between a sub-surface feature and its' surroundings. This will both demonstrate the sensitivity of the sensor but also its portability. Ultimately, this will show the technologies maturity as a device for sub-surface mapping.

A final potential for this sensor is its use on moving platforms. So far, it has been assumed that the sensor will be manually moved between points to measure while stationary. It is feasible, however, for the sensor to be continually measuring while on a moving platform such as a train, plane, boat or unmanned aerial vehicle (UAV). It is likely for these applications that different measurement schemes would have to be implemented. This is both as the potential targets would be different but also that the motion of the platform could necessitate shorter measurement times.

The field of atom interferometry is rapidly growing, with new potential applications being uncovered frequently. It truly has the potential to revolutionise precision measurement, both in the laboratory and, increasingly, in the field. The utilisation of such precise sensors for sub-surface mapping could drastically change how we make use of the space beneath our feet. This work has demonstrated the design and production of a sensor which translates the techniques of atom interferometry into a person portable package.

Appendix One

Bloch Sphere Approach

The description of an atom interferometer given in section 2.3.1 treats the process as semi-classical. Most notably the atoms are treated as an ensemble and when a state splitting interaction occurs, it is assumed half of the atoms change state and half do not. This is valid if at any point throughout the sequence the population in either arm is *observed*. When discussing these state changing interactions, it is more precise to talk about *probabilities* of transfer.

In a separate but equally valid view, each atom is put into a *super-position* of both states. The *Bloch sphere* is a method for formulating and visualising super-positions of a quantum two-state system. The descriptions given in this section will follow from the presentation in [93]. The Bloch sphere is a unitary sphere with one of the two states at either pole (north pole $|1\rangle$, south pole $|2\rangle$). The *state* is shown by the *Bloch vector*, $\boldsymbol{R}$, which points to the complex state on the surface of the sphere. It is defined by amplitudes along Cartesian coordinates,

$$\boldsymbol{R} = u\hat{\boldsymbol{x}} + v\hat{\boldsymbol{y}} + w\hat{\boldsymbol{z}} \ . \tag{A.1}$$

Of particular interest is how the Bloch vector changes with a light field. Similarly to the Bloch vector, a *field vector* $\mathbf{\Omega}$ is defined which is unitary on the Bloch sphere and shares a coordinate system,

$$\mathbf{\Omega} = \Omega_R cos(\phi_L)\hat{\boldsymbol{x}} + \Omega_R sin(\phi_L)\hat{\boldsymbol{y}} + \delta\hat{\boldsymbol{z}} \ , \tag{A.2}$$

where Ω_R is the two-photon generalised Rabi frequency, ϕ_L is the phase of the light and δ the single-photon detuning.

The time evolution of the Bloch vector can be shown to be a *torque* on the Bloch vector caused by the field vector,

$$\frac{d\boldsymbol{R}}{dt} = \boldsymbol{R} \times \mathbf{\Omega} \ . \tag{A.3}$$

The Bloch (state) vector $\boldsymbol{R}$ rotates *around* the axis defined by the field vector $\mathbf{\Omega}$. With no detuning, the field vector will naturally be in the $x-y$ plane. The laser phase ϕ_L defines the rotation of the field vector around the z axis. The detuning δ defines the lifting of the field vector from the $x-y$ plane. An on-resonant pulse with $\phi_L = 0$ provides a field vector along the x-axis. This causes a rotation of the state vector around this, in the $y-z$ plane. The situation is shown in figure A.1, equivalent to the Rabi oscillations discussed in section 2.2.3.

The Bloch sphere picture provides an incredibly powerful tool for easily visualising coherent pulses. Familiar transitions such as the π pulse and $\pi/2$ pulse can be visualised as rotations of a simple field vector, but only for the correct time to rotate the state vector 180° or 90°. Another important building block of understanding experimental sequences is the *free evolution*. This is how the state vector evolves without the presence of a field

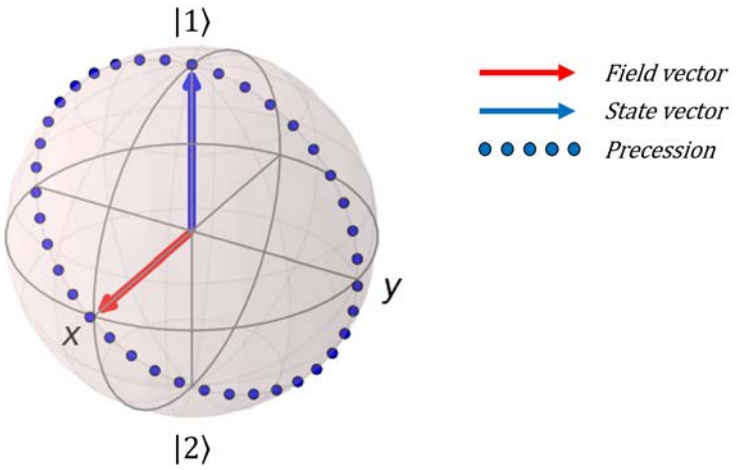

Figure A.1: A model of a Bloch sphere displaying how the time evolution of the state vector is a rotation around the field vector. For an on-resonance pulse, the state vector precesses around the vector, sketching out a Rabi oscillation.

vector. The state vector can be shown to precess around the z-axis in whatever plane it was previously in. The above situations are displayed in figure A.2.

The Bloch sphere picture is also very instructive when examining the effect of light fields that are off-resonant. As can be seen in equation A.2, a detuning δ will lift the field vector off the $x - y$ plane. The state vector will still rotate around the field vector. With an off-resonant pulse, the state vector will not be able to reach the other pure state. This is shown in figure A.3. The effect can be compared to the results in figure 2.9 where the Rabi oscillations cannot reach the second pure state.

As can be seen in equation A.2, a phase change in the laser ϕ_L rotates the field vector about the z-axis. The effect this has on the state vector is shown in figure A.4. For a Rabi oscillation, this does not change the output (the observed state populations). However, in combination, a phase change can have a measured affect in a sequence.

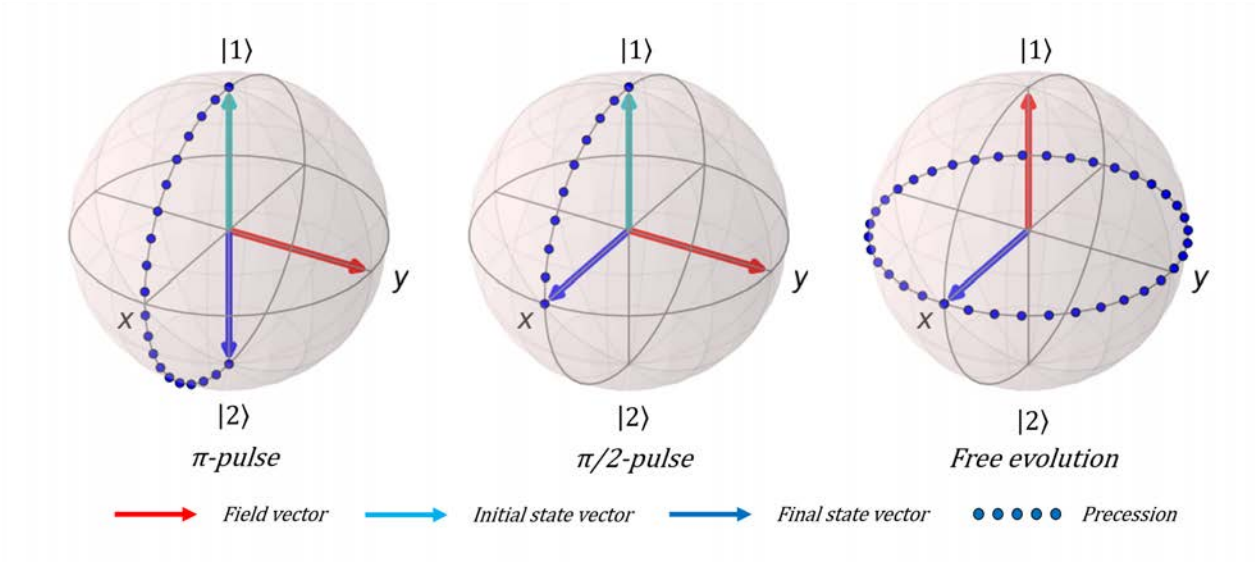

Figure A.2: A model of a Bloch sphere displaying the common building blocks of atom interferometry experiments. The π pulse is understood as a pulse of sufficient time to fully transfer the population from one state to another. Similarly a $\pi/2$ pulse will transfer the population from a pure into a super-position of both states. Finally, free evolution is the precession of the state vector around the z-axis in the absence of a light field.

By combination of the coherent pulses and control of the laser parameters, sequences can be constructed. A simple sequence is the Ramsey interferometer. The sequence consists of two $\pi/2$ pulses separated by a free evolution time T. The phase of the first pulse is arbitrary as it defines the axes used. The first pulse transitions the atoms from state $|1\rangle$ into a super-position state ($z = 0$). In the free evolution the state vector will precess around the z-axis. At any multiple of 2π the state vector will arrive back at it's starting point. The second pulse will then cause the state vector to rotate around the field vector. Given an idealised sequence where $T = 2n\pi$ and the laser is on resonance with no phase shift, the state will be transferred to state $|2\rangle$.

If the free evolution time is not a multiple of 2π the state vector will not be orthogonal to the field vector for the second pulse. This will mean the state vector does not end up in

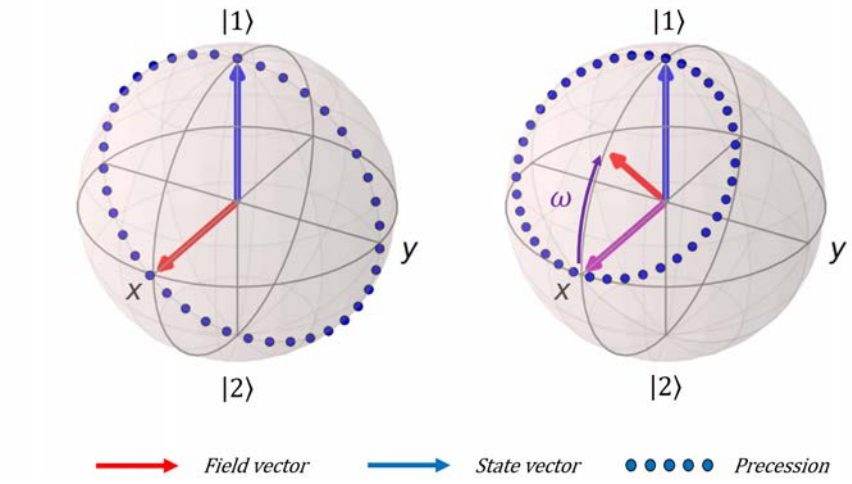

Figure A.3: A model showing the effect of detuning on a Rabi oscillation. Detuning the pulse from resonance lifts the field vector out of the $x - y$ plane. The state vector rotates around the field vector, but can now not reach the second pure state.

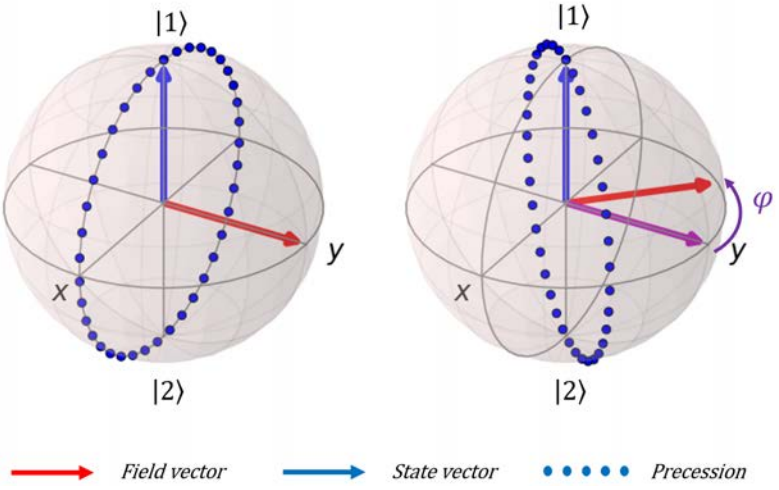

Figure A.4: A model showing the effect of laser phase on a Rabi oscillation. Changing the phase of the laser only changes the complex path the state vector precesses around, not the observable state populations.

a pure $|2\rangle$ state. This situation is shown in the first case of figure A.5. If the second pulse is off-resonant or has experienced a phase shift (assuming $T = 2n\pi$), the atom will also be

unable to reach a pure state. Through scanning any one of these parameters (ΔT, $\Delta\delta$, $\Delta\phi_L$) between $0 \rightarrow 2\pi$, any state vector between $|1\rangle$ and $|2\rangle$ can be obtained.

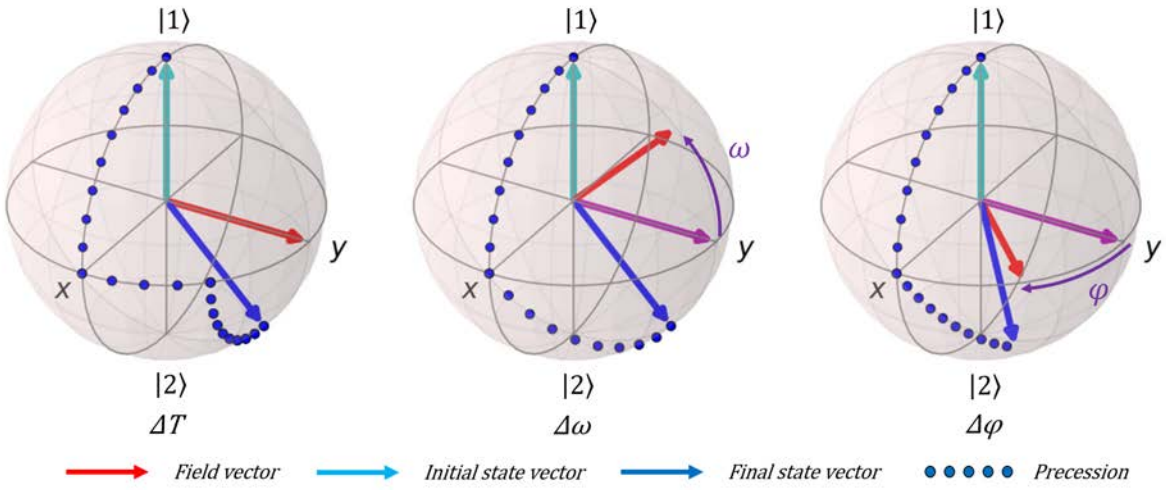

Figure A.5: A model showing a Ramsey sequence and the effect of the tuning parameters. The tuning of either the free evolution time, detuning or laser phase can scan out any state between and including the pure states $|1\rangle$ and $|2\rangle$.

The Bloch sphere and the tools thus far examined can give some valuable insight in the Mach-Zehnder style atom interferometry sequence described in section 2.3.1. This sequence is also referred to as the Ramsey-Bordé sequence ($\pi/2 - \pi - \pi/2$). Again, the first pulse defines the phase axis and puts the atoms in a super-position state. The middle π pulse is flanked by periods of free evolution. It is important that these periods are equal, otherwise the symmetry of the sequence is broken. Assuming the laser is on-resonance throughout and the phase does not change, the free evolution time will not affect the ability to return to the starting state. As the two periods of free evolution are equal, it has no affect on the states reached. The sequence and the contribution of free evolution can be seen in figure A.6.

In section 2.3.1 and particularly by inspection of equation 2.64 it can be seen that changing either the detuning through the sequence (changing α) or the phase of the final

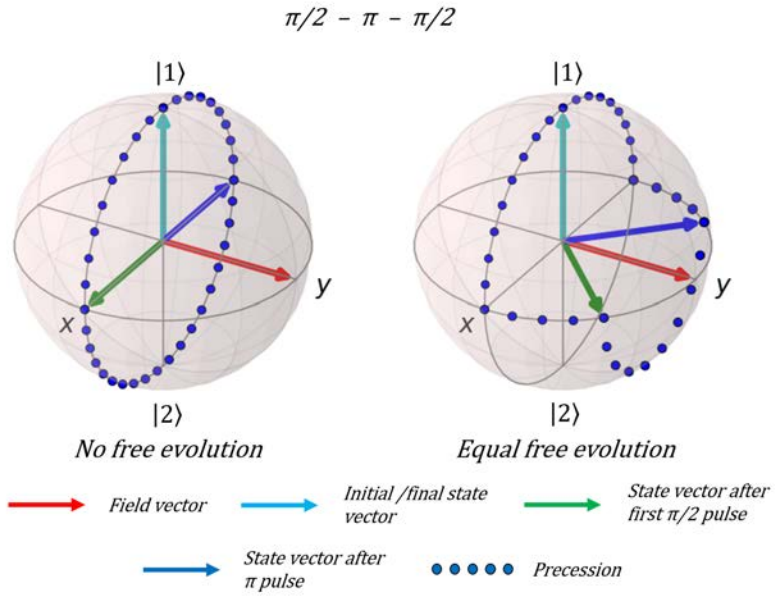

Figure A.6: A model showing a $\pi/2 - \pi - \pi/2$ sequence and the effect of the free evolution. As the free evolution times are equal, the symmetry cancels out the effect and it does not affect the ability to reach the original pure state.

pulse (ϕ_{III}) can be used to control the state. Either of these parameters can be used to control an experiment and scan over fringes. The case for detuning is displayed in figure A.7, only showing a detuned final pulse for clarity. The case for phase is shown in figure A.8, similarly only with the phase of the final pulse shown. With both cases it can be seen that by scanning either parameter through 2π any state between and including pure states $|1\rangle$ and $|2\rangle$ can be reached.

The Bloch sphere picture, with simple understanding of the physics, allows an instructive picture to be built of the processes involved. The mathematics produces the same observable results as the *path integral approach* (section 2.3.1) [93]. The Bloch sphere can also be a useful tool in interpreting the gravity measurement, as well as the atom interferometry sequence.

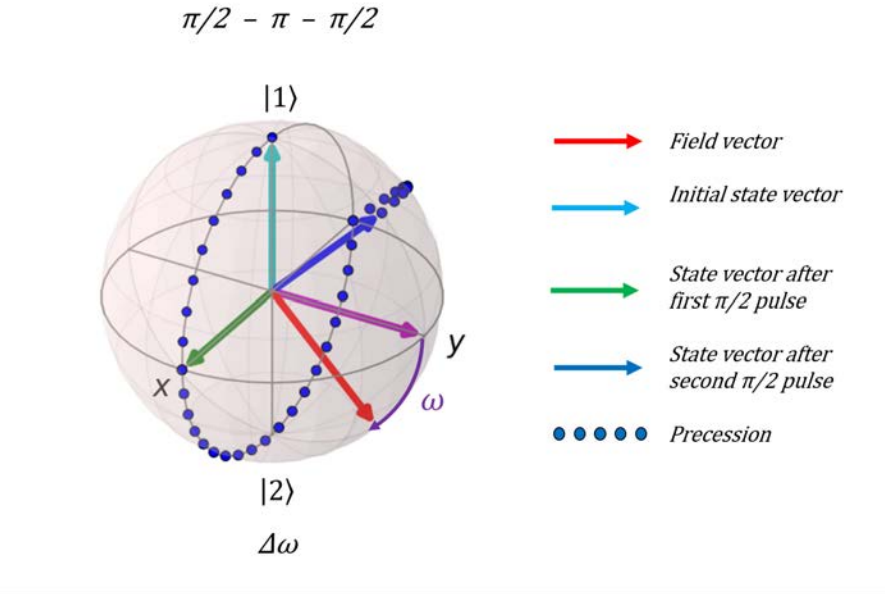

Figure A.7: A model showing a $\pi/2 - \pi - \pi/2$ sequence and the effect of detuning the final pulse. By scanning the detuning through 2π, any arbitrary final state can be obtained.

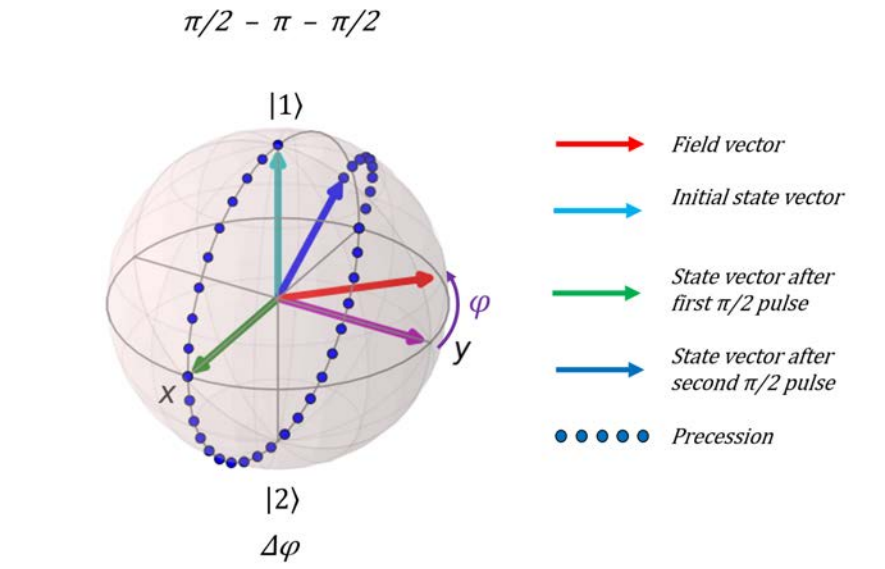

Figure A.8: A model showing a $\pi/2 - \pi - \pi/2$ sequence and the effect of changing the phase of the final pulse. By scanning the phase through 2π, any arbitrary final state can be obtained.

Appendix Two

Vacuum Construction and Preparation

B.1 Vacuum Construction

The monolithic titanium chamber was machined (detail in figure B.1) and cleaned according to the following routine:

1. Manually cleaned of machining grease using isopropanol and acetone, including scrubbing the inside.
2. Pre-baked in a vacuum oven for several days at 200 °C
3. Cleaned in an ultrasonic bath of isopropanol for 1hr at 40 °C
4. Rinsed with de-ionised water
5. Cleaned in an ultrasonic bath with detergent for 1hr at 40 °C
6. Rinsed with de-ionised water
7. Cleaned in an ultrasonic bath of acetone for 1hr at 40 °C

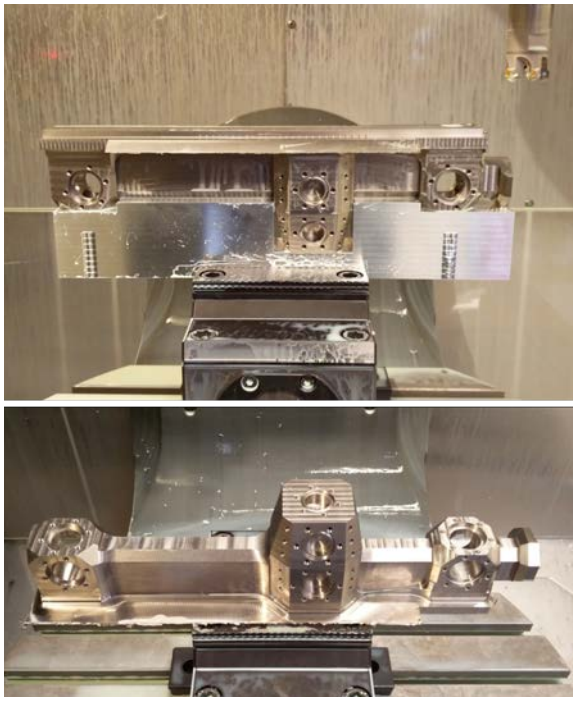

Figure B.1: Photographs of the machining of the vacuum chamber.

The internal optics were fixed with adhesive into the chamber using *TorrSeal*, a two part epoxy with very low out-gassing rates. Firstly, the bottom 1" mirror was glued in. A quarter wave plate was glued on top of the bottom mirror. The prisms were then each individually glued in.

Next, the indium sealed windows were attached to the chamber (shown in figure B.3). The surface of the chamber is inspected for any burrs of scratches. Next, the indium ring is formed. A forming circle was produced and the ring made around this. The two ends of the ring are cut diagonally and overlaid, making sure the pressure of the window will press the two ends together. The ring is the placed centrally on the chamber surface and the window on top of this. A piece of lens tissue is placed in the window to protect it. An annulus of PTFE is then placed on top to provide a medium between the compression flange and the window. This is an annulus as the pressure needs to be supported on the chamber side or the window will crack in the middle. Finally the compression flange is placed on top and

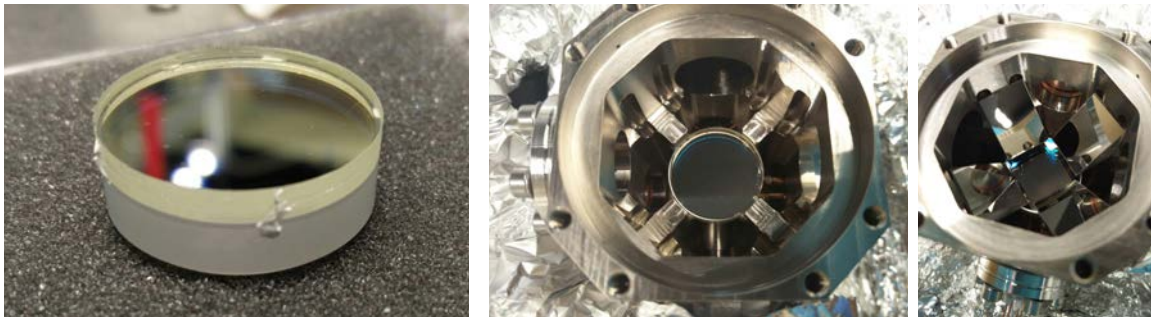

(a) Mirror and 1/4 wave-plate for the MOT.

(b) Mirror glued in the chamber.

(c) Prisms glued in the chamber.

Figure B.2: Photographs of the bottom mirror, 1/4 wave-plate and prisms gluing into the vacuum chamber.

pressure is slowly added to the attaching bolts to evenly apply pressure. A torque wrench was used to increase the torque on each bolt by 0.2 Nm at a time up to 2.0 Nm.

The feed-through for the dispensers and microwave antenna were then attached. These are Conflat flanges. A similar process as for the indium seals is used (shown in figure B.4). A knife edge is machined into both sides of the flange. A copper gasket is then placed between the two sides of the flange. When pressure is applied to the flange by tightening the attaching bolts, the knife edges bite into the copper gasket, forming a seal. Again, the bolts are tightened gradually in order to form an even seal all the way around the gasket.

Next, the vacuum peripherals (ion pump, getter and valve) were attached to the chamber using CF flanges. The chamber was rigidly mounted and connected to the bellows of the turbo pump. The sealed chamber ready for vacuum preparation is shown in figure B.5.

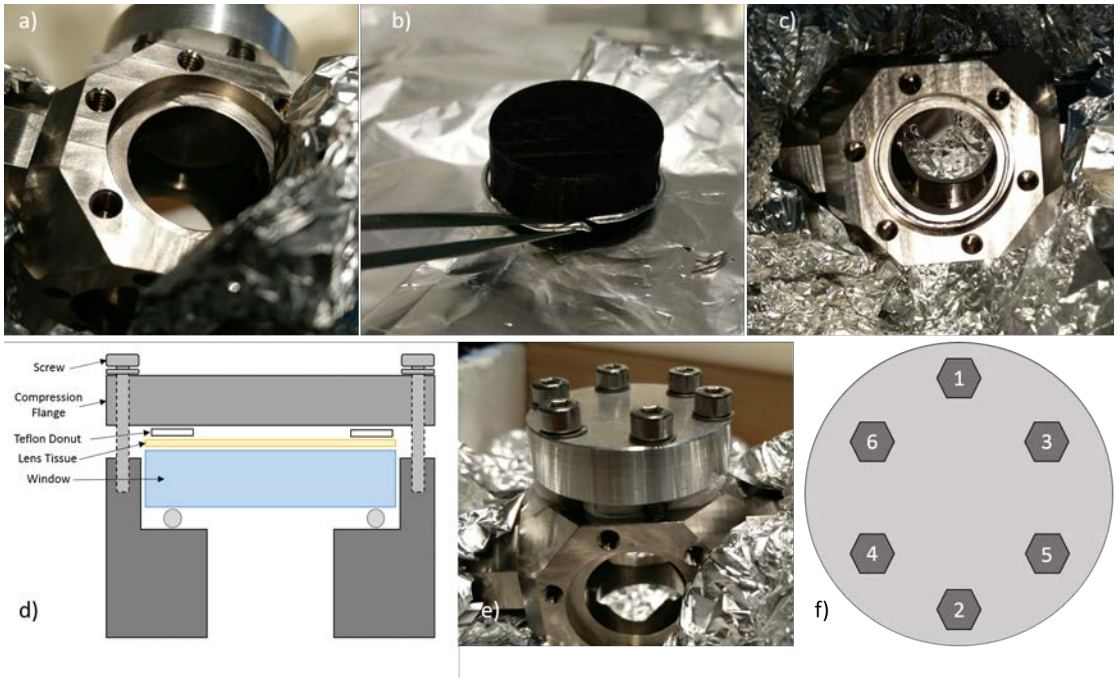

Figure B.3: Process for attaching windows to the vacuum chamber via indium sealing. **a)** Check the chamber surface for burrs and scratches. **b)** Form the indium ring. **c)** Place the indium ring on the chamber. **d)** Place tissue, PTFE ring and compression flange on window. **e)** Place the screws through the compression flange into the chamber. **f)** Tighten the screws in this pattern, 0.2 Nm at a time until roughly 2.0 Nm.

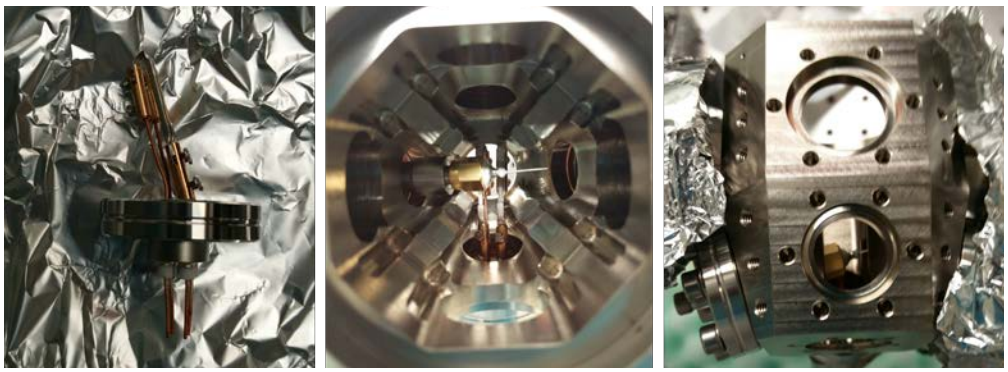

Figure B.4: Photographs showing the mounting of the dispensers and microwave antenna in the volume behind the MOT region.

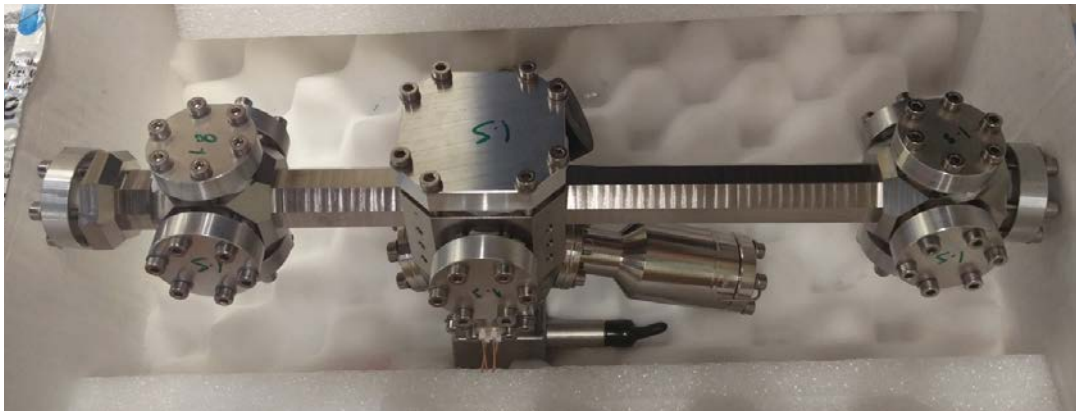

Figure B.5: Photographs of the vacuum system with the Indium seals on and ready for vacuum preparation.

B.2 Vacuum Preparation

The turbo pump is used to remove the air from the chamber. Over the first few hours of operation this should reach a pressure of 10^{-6} mbar and being left overnight should reach 10^{-8} mbar. If this does not occur, some join may have a macroscopic or microscopic leak. Leaks in CF flanges can be tested by applying a small amount of acetone to the join. If the pressure spikes, it indicates that there is a leak which the acetone can enter through and vaporise.

If the initial pumping is successful and no leaks are detected, the system is baked. This is a process of heating the whole system to vaporise any residual water which will be evacuated through the turbo pump. Temperature sensors are installed around the chamber, taking care of the temperature around glass to monitor any temperature gradients. The whole chamber is then wrapped in many layers of aluminium foil to create a good heat conductance. Heating strips are wrapped around the chamber and further foil around this. Finally the system is placed in heat proof material to prevent danger and keep the heat in.

The temperature of the heating tapes is slowly increased, aiming for 110 °C but

not increasing by more than a couple of degrees per minute. The temperature must be kept above the boiling point of water (100 °C) but below the softening point of indium (∼130 °C). The temperature was kept at this level for two weeks. Initially during heating the pressure increases as the gas load increases. Gradually the pressure reading will drop and plateau, roughly an order of magnitude lower than previously.

While the chamber is still hot the dispensers can be de-gassed. This process involves gently heating the dispensers to remove dirt. After this the getter can be activated and the ion pump turned on. If the pressure reading here is low enough ($< 10^{-8}$ mbar) the chamber can be cooled and unwrapped. When cool the pressure should drop by roughly another order of magnitude.

The pressure should read in the 10^{-10} mbar, at this pressure the contribution to the gas load from unwanted species will be several orders of magnitude lower than that of rubidium. The final step is to activate the dispensers. With resonant light in the chamber (a thin beam works best) the current through the dispensers can be slowly increased. The pressure should be allowed to spike and resettle between increasing. After reaching ∼5 A the dispenser should open and rubidium atoms should be seen fluorescing in the beam. Now the valve can be closed and the chamber removed from the turbo pump.

For the chamber produced as part of this work, the final pressure reads in the 10^{-11} mbar on the ion pump under normal load. When the dispensers are being heated, the ion pump reads low 10^{-10} mbar.

Appendix Three

Magnetic Shield Simulations

The following are simulations for the magnetic shielding of the system, performed by *Magnetic Shields Limited*.

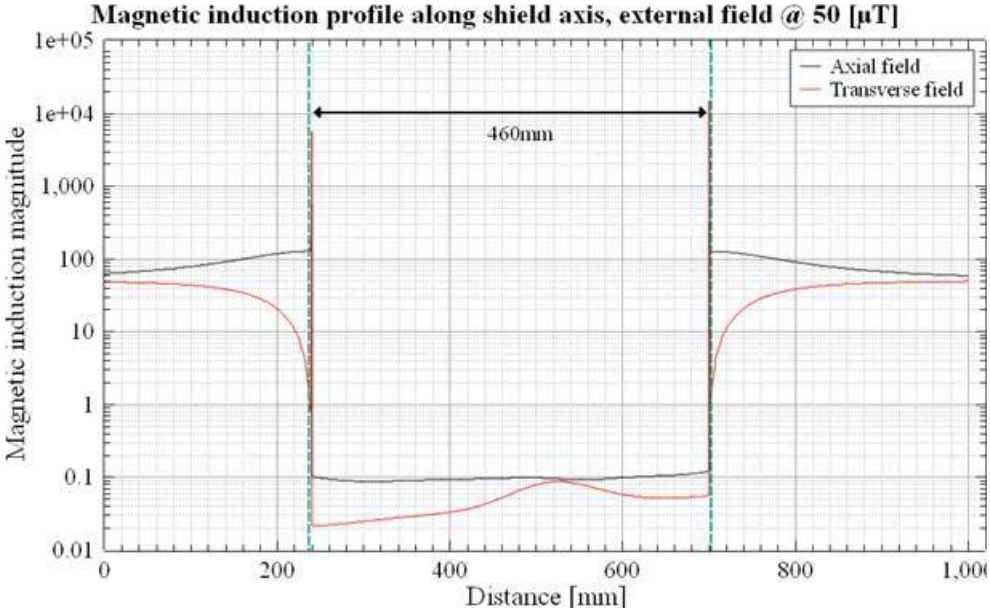

Figure C.1: Magnetic field induction magnitude profile along the shield's longitudinal axis, under an external field of 50 μT. Each curve corresponds to a different external field orientation. The green dash-lines indicate the boundaries of the shield. Performed by *Magnetic Shields Limited*.

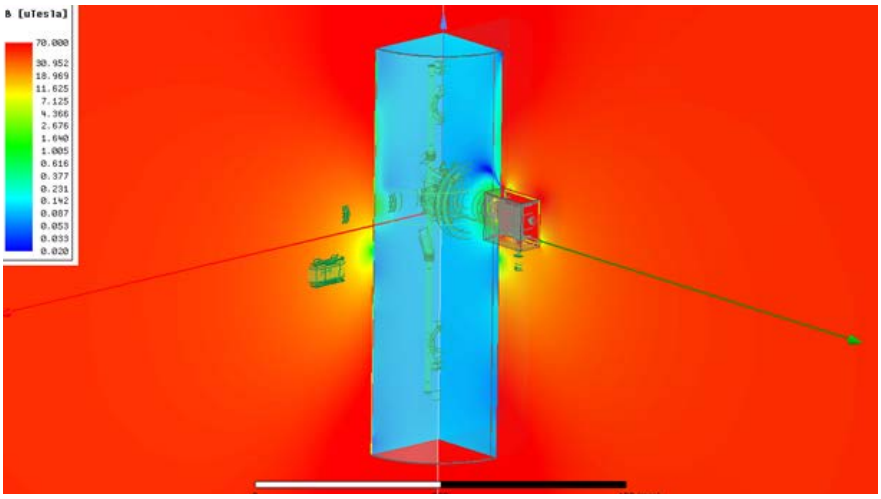

(a) Colourmap plot, illustrating the distribution of the magnetic field induction magnitude over the x- and y- planes for the axial external field case.

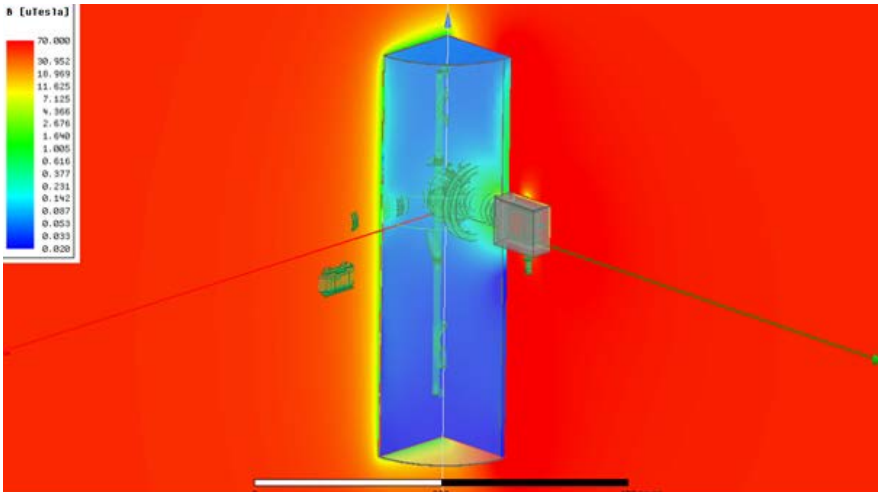

(b) Colourmap plot, illustrating the distribution of the magnetic field induction magnitude over the x- and y- planes for the transverse external field case.

Figure C.2: Simulations conducted by *Magnetic Shields Limited* for the magnetic shields designed.

References

[1] C. Freier et al. "Mobile quantum gravity sensor with unprecedented stability". In: *Journal of Physics: Conference Series* 723 (2016), p. 012050. DOI: 10.1088/1742-6596/723/1/012050. URL: https://doi.org/10.1088%5C%2F1742-6596%5C%2F723%5C%2F1%5C%2F012050.

[2] United States Geological Survey. *USGS, How much does sinkhole damage cost each year in the United States?* 2020. URL: usgs.gov/faqs/how-much-does-sinkhole-damage-cost-each-year-united-states?qt-news_science_products=3#qt-news_science_products.

[3] Subsurface Instruments inc. ***ML-1M*** *All-inclusive magnetic locator with simple, one-handed operation.* 2020. URL: ssilocators.com/products/ML-1M.

[4] Sensors & Software. *Sensors & Software, Ground Penetrating Radar.* 2020. URL: sensoft.ca/ground-penetrating-radar/.

[5] British Geological Survey. *BGS, GB Land Gravity Survey.* 2020. URL: bgs.ac.uk/products/geophysics/landGravity.

[6] Micro-g LaCoste. *FG5-X Absolute Gravity Meters.* 2020. URL: microglacoste.com/product/fg5-x-absolute-gravimeter/.

[7] GWR Instruments. *Superconducting Gravity Meter.* 2020. URL: gwrinstruments.com/pdf/principles-of-operation.pdf.

[8] Tang S., Liu H., and Yan S. et al. "A high-sensitivity MEMS gravimeter with a large dynamic range". In: *Microsyst Nanoeng* 5.45 (2019). DOI: https://doi.org/10.1038/s41378-019-0089-7.

[9] University of Glasgow. *Wee-g: Glasgows Gravimeter*. 2020. URL: gla.ac.uk/research/beacons/nanoquantum/wee-gglasgowsgravimeter/.

[10] Scintrex. *Scintrex, CG-5 Autograv*. 2020. URL: scintrexltd.com/wp-content/uploads/2017/02/CG-5-Manual-Ver_8.pdf.

[11] M. Kasevich and S. Chu. "Atomic interferometry using stimulated Raman transitions". In: *Phys. Rev. Lett.* 67 (2 1991), pp. 181–184. DOI: 10.1103/PhysRevLett.67.181. URL: https://link.aps.org/doi/10.1103/PhysRevLett.67.181.

[12] D. Schlippert et al. "Quantum Test of the Universality of Free Fall". In: *Phys. Rev. Lett.* 112 (20 2014), p. 203002. DOI: 10.1103/PhysRevLett.112.203002. URL: https://link.aps.org/doi/10.1103/PhysRevLett.112.203002.

[13] G. Rosi, F. Sorrentino, and L. Cacciapuoti. "Precision measurement of the Newtonian gravitational constant using cold atoms". In: *Nature* 510 (2014), pp. 518–521. DOI: https://doi.org/10.1038/nature13433.

[14] C. Jönsson. "Electron diffraction at multiple slits". In: *American Journal of Physics* 42 (1974), pp. 4–11.

[15] A. Tonomura et al. "Demonstration of single-electron build-up of an interference". In: *American Journal of Physics* 57 (1989), pp. 117–120.

[16] O. Carnal and J. Mlynek. "Young's double-slit experiment with atoms: a simple atom interferometer". In: *Physical Review Letters* 66 (1991), pp. 2689–2692.

[17] D.W. Keith et al. "An interferometer for atoms". In: *Physical Review Letters* 66 (1991), pp. 2693–2696.

[18] M.W. Noel and C.R. Stroud Jr. "Young's double-slit interferometry within an atom". In: *Physical Review Letters* 75 (1995), pp. 1252–1255.

[19] TMD. *TMD, Quantum Products*. 2020. URL: www.tmd.co.uk/products/quantum-products/.

[20] N.J. Cooper et al. "Additively manufactured ultra-high vacuum chamber below 10^{-10} mbar". In: (1991). URL: https://arxiv.org/pdf/1903.07708.pdf.

[21] A. Lamb. "Cold Atom Gravity Gradiometer for Field Applications". PhD thesis. University of Birmingham, 2018.

[22] Brynle Barrett et al. "Dual matter-wave inertial sensors in weightlessness". In: *Nat Commun* 7.13786 (2016). DOI: https://doi.org/10.1038/ncomms13786.

[23] Hinton A. et al. "A portable magneto-optical trap with prospects for atom interferometry in civil engineering". In: *Phil. Trans. R. Soc. A.* 375 (2016). DOI: http://doi.org/10.1098/rsta.2016.0238.

[24] Scintrex. *Scintrex, CG-6 Autograv*. 2020. URL: scintrexltd.com/wp-content/uploads/2018/04/CG-6-Operations-Manual-RevB.pdf.

[25] U. Riccardi, S. Rosat, and J. Hinderer. "On the Accuracy of the Calibration of Superconducting Gravimeters Using Absolute and Spring Sensors: A Critical Comparison". In: *Pure and Applied Geophysics* 169 (2012), pp. 1343–1356.

[26] A.A. Krasnov, A.V. Sokolov, and L.S. Elinson. "A new air-sea shelf gravimeter of the Chekan series". In: *Gyroscopy and Navigation* 5 (2014), pp. 131–137.

[27] L.K. Zheleznyak et al. "The results of testing the Chekan gravimeter at the Leningrad gravimetric testing area". In: *Physics of the Solid Earth* 51 (2015), pp. 315–320.

[28] J. Hinderer, D. Crossley, and R.J. Warburton. *Gravimetric Methods – Superconducting Gravity Meters, Treatise on Geophysics*. 2nd ed. Vol. 3. Elsevier BV, 2007, pp. 65–122.

[29] R.J. Warburton and R.C. Reineman. "Initial results with the new GWR iGrav superconducting gravity meter". In: *International Association of Geodesy (IAG) Symposium on Terrestrial Gravimetry: Static and Mobile Measurements* (2010), pp. 22–25.

[30] R.P. Middlemiss et al. "Measurement of the Earth tides with a MEMS gravimeter". In: *Nature* 531 (2016), pp. 614–617.

[31] M. Schmidt. "A mobile high-precision gravimeter based on atom interferometry". PhD thesis. Humboldt-Universität zu Berlin, 2011.

[32] V. Ménoret, P. Vermeulen, and N. et al. Le Moigne. "Gravity measurements below 10^{-9} g with a transportable absolute quantum gravimeter". In: *Sci Rep* 8.12300 (2018). DOI: https://doi.org/10.1038/s41598-018-30608-1.

[33] μQUANS. *μQUANS, Absolute Quantum Gravimeter*. 2020. URL: https://www.muquans.com/product/absolute-quantum-gravimeter/.

[34] Zhijie Fu et al. "A new type of compact gravimeter for long-term absolute gravity monitoring". In: *Metrologia* 56.025001 (2019). DOI: https://doi.org/10.1088/1681-7575/aafcc7.

[35] Y. Bidel, N. Zahzam, and A. et al. Bresson. "Absolute airborne gravimetry with a cold atom sensor". In: *J Geod* 94.20 (2019). DOI: https://doi.org/10.1007/s00190-020-01350-2.

[36] Y. Bidel, N. Zahzam, and C. et al. Blanchard. "Absolute marine gravimetry with matter-wave interferometry". In: *Nat Commun* 9.627 (2018). DOI: https://doi.org/10.1038/s41467-018-03040-2.

[37] O. Carraz, F. Lienhart, and R. et al Charriére. "Compact and robust laser system for onboard atom interferometry". In: *Appl. Phys. B* 97.405 (2009). DOI: https://doi.org/10.1007/s00340-009-3675-9.

[38] X Wu et al. "Gravity surveys using a mobile atom interferometer". In: *Science Advances* 5.9 (2019). DOI: 10.1126/sciadv.aax0800. URL: https://advances.sciencemag.org/content/5/9/eaax0800.

[39] P Gillot et al. "Stability comparison of two absolute gravimeters: optical versus atomic interferometers". In: *Metrologia* 51.5 (2014), pp. L15–L17. DOI: 10.1088/0026-1394/51/5/l15. URL: https://doi.org/10.1088%5C%2F0026-1394%5C%2F51%5C%2F5%5C%2Fl15.

[40] R Karcher et al. "Improving the accuracy of atom interferometers with ultracold sources". In: *New Journal of Physics* 20.11 (2018), p. 113041. DOI: 10.1088/1367-2630/aaf07d. URL: https://doi.org/10.1088%5C%2F1367-2630%5C%2Faaf07d.

[41] Zhong-Kun Hu et al. "Demonstration of an ultrahigh-sensitivity atom-interferometry absolute gravimeter". In: *Phys. Rev. A* 88 (4 2013), p. 043610. DOI: 10.1103/PhysRevA.88.043610. URL: https://link.aps.org/doi/10.1103/PhysRevA.88.043610.

[42] Alexey V Veryaskin. *Gravity gradiometry, Gravity, Magnetic and Electromagnetic Gradiometry*. 2053-2571. Morgan & Claypool Publishers, 2018, 1-1 to 1–56. ISBN: 978-1-6817-4700-2. DOI: 10.1088/978-1-6817-4700-2ch1. URL: http://dx.doi.org/10.1088/978-1-6817-4700-2ch1.

[43] John Brett and James Brewster. *Accelerometer and rate sensor package for gravity gradiometer instruments*. Nov. 2008.

[44] Teledyne e2v. *Quantum technology commercialisation*. 2017. URL: teledyne-e2v.com/content/uploads/2017/08/Te2v_Brochure_Quantum_2017.pdf.

[45] J. M. McGuirk et al. "Sensitive absolute-gravity gradiometry using atom interferometry". In: *Phys. Rev. A* 65 (3 2002), p. 033608. DOI: 10.1103/PhysRevA.65.033608. URL: https://link.aps.org/doi/10.1103/PhysRevA.65.033608.

[46] Xiao-Chun Duan et al. "Operating an atom-interferometry-based gravity gradiometer by the dual-fringe-locking method". In: *Phys. Rev. A* 90 (2 2014), p. 023617. DOI: 10.1103/PhysRevA.90.023617. URL: https://link.aps.org/doi/10.1103/PhysRevA.90.023617.

[47] Sheng-wey Chiow, Jason Williams, and Nan Yu. "Noise reduction in differential phase extraction of dual atom interferometers using an active servo loop". In: *Phys. Rev. A* 93 (1 2016), p. 013602. DOI: 10.1103/PhysRevA.93.013602. URL: https://link.aps.org/doi/10.1103/PhysRevA.93.013602.

[48] T.W. Hänsch and A.L. Schawlow. "Cooling of gases by laser radiation". In: *Optics Communications* 13 (1975), pp. 68–69. DOI: https://doi.org/10.1016/0030-4018(75)90159-5. URL: http://www.sciencedirect.com/science/article/pii/0030401875901595.

[49] Steven Chu et al. "Three-dimensional viscous confinement and cooling of atoms by resonance radiation pressure". In: *Phys. Rev. Lett.* 55 (1985), pp. 48–51. DOI: 10.1103/PhysRevLett.55.48. URL: https://link.aps.org/doi/10.1103/PhysRevLett.55.48.

[50] William D. Phillips. "Nobel Lecture: Laser cooling and trapping of neutral atoms". In: *Rev. Mod. Phys.* 70 (1998), pp. 721–741. DOI: 10.1103/RevModPhys.70.721. URL: https://link.aps.org/doi/10.1103/RevModPhys.70.721.

[51] Claude N. Cohen-Tannoudji. "Nobel Lecture: Manipulating atoms with photons". In: *Rev. Mod. Phys.* 70 (1998), pp. 707–719. DOI: 10.1103/RevModPhys.70.707. URL: https://link.aps.org/doi/10.1103/RevModPhys.70.707.

[52] Steven Chu. "Nobel Lecture: The manipulation of neutral particles". In: *Rev. Mod. Phys.* 70 (1998), pp. 685–706. DOI: 10.1103/RevModPhys.70.685. URL: https://link.aps.org/doi/10.1103/RevModPhys.70.685.

[53] Harold J. Metcalf and Peter van der Straten. *Laser Cooling and Trapping*. Springer, 2001.

[54] C. J. Foot. *Atomic Physics*. Oxford, 2004.

[55] Daniel Steck. "Rubidium 87 D Line Data". In: (2003).

[56] K. I. Lee et al. "Single-beam atom trap in a pyramidal and conical hollow mirror". In: *Opt. Lett.* 21.15 (1996), pp. 1177–1179. DOI: 10.1364/OL.21.001177. URL: http://ol.osa.org/abstract.cfm?URI=ol-21-15-1177.

[57] Paul Berman. *Atom Interferometry*. Academic Press, 1996.

[58] Malo Cadoret et al. "Combination of Bloch oscillations with a Ramsey-Borde interferometer: New determination of the fine structure constant". In: *Phys. Rev. Lett.* 101 (2008), p. 230801. DOI: 10.1103/PhysRevLett.101.230801.

[59] E. Peik et al. "Bloch oscillations and an accelerator for cold atoms". In: *Applied Physics B* 65 (1997), pages685–692. DOI: https://doi.org/10.1007/s003400050334.

[60] S. Abend et al. "Atom-Chip Fountain Gravimeter". In: *Phys. Rev. Lett.* 117 (20 2016), p. 203003. DOI: 10.1103/PhysRevLett.117.203003. URL: https://link.aps.org/doi/10.1103/PhysRevLett.117.203003.

[61] Ekkehard Peik et al. "Bloch oscillations of atoms, adiabatic rapid passage, and monokinetic atomic beams". In: *Phys. Rev. A* 55 (4 1997), pp. 2989–3001. DOI: 10.1103/PhysRevA.55.2989. URL: https://link.aps.org/doi/10.1103/PhysRevA.55.2989.

[62] Pippa Storey and Claude Cohen-Tannoudji. "The Feynman path integral approach to atomic interferometry. A Tutorial". In: *Journal de Physique II* 4 (11 1994), pp. 1999–2027. DOI: 10.1051/jp2:1994103.jpa-00248106f.

[63] M. Kasevich and S. Chu. "Measurement of the gravitational acceleration of an atom with a light-pulse atom interferometer". In: *Appl. Phys. B* 54 (1992), pp. 321–332. DOI: https://doi.org/10.1007/BF00325375.

[64] K. I. Lee et al. "Single-beam atom trap in a pyramidal and conical hollow mirror". In: *Opt. Lett.* 21.15 (), pp. 1177–1179. DOI: 10.1364/OL.21.001177. URL: http://ol.osa.org/abstract.cfm?URI=ol-21-15-1177.

[65] Tim Kovachy, Sheng-wey Chiow, and Mark A. Kasevich. "Adiabatic-rapid-passage multiphoton Bragg atom optics". In: *Phys. Rev. A* 86 (1 2012), p. 011606. DOI: 10.1103/PhysRevA.86.011606. URL: https://link.aps.org/doi/10.1103/PhysRevA.86.011606.

[66] A. Bertoldi et al. "Atom interferometry gravity-gradiometer for the determination of the Newtonian gravitational constant G". In: *Eur. Phys. Jour. D* 40 (2006), p. 271. DOI: https://doi.org/10.1140/epjd/e2006-00212-2.

[67] SAES group. *Alkali Metal Dispensers*. 2020. URL: www.saesgetters.com/products-functions/products/dispensers/alkali-metals-dispensers.

[68] SAES group. *CapaciTorr NEG pumps*. 2020. URL: www.saesgetters.com/products-functions/products/vacuum-pumps/capacitorr-neg-pumps.

[69] Gamma Vacuum. *Small Ion Pumps*. 2020. URL: https://www.gammavacuum.com/index.php/product?id=1.

[70] L. Earl, M. Langlois, and M. Holynski. *Apparatus for Generating Vertically Separate Atom Clouds*. ZSR1208A. 2020.

[71] V. Ménoret et al. "Dual-wavelength laser source for onboard atom interferometry". In: *Opt. Lett.* 36.21 (2011), pp. 4128–4130. DOI: 10.1364/OL.36.004128.

[72] S. Merlet et al. "A simple laser system for atom interferometry". In: *Appl. Phys. B* 117 (2014), pp. 749–754. DOI: https://doi.org/10.1007/s00340-014-5890-2.

[73] J. Le Gouet et al. "Influence of lasers propagation delay on the sensitivity of atom interferometers". In: *Eur. Phys. J. D* 44 (2007), pp. 419–425. DOI: https://doi.org/10.1140/epjd/e2007-00218-2.

[74] Lingxiao Zhu et al. "Application of optical single-sideband laser in Raman atom interferometry". In: *Opt. Express* 26.6 (2018), pp. 6542–6553. DOI: 10.1364/OE.26.006542. URL: http://www.opticsexpress.org/abstract.cfm?URI=oe-26-6-6542.

[75] Clemens Rammeloo et al. "Performance of an optical single-sideband laser system for atom interferometry". In: *J. Opt. Soc. Am. B* 37.5 (2020), pp. 1485–1493. DOI: 10.1364/JOSAB.385919. URL: http://josab.osa.org/abstract.cfm?URI=josab-37-5-1485.

[76] iXblue. *MXIQ-LN-30*. 2020. URL: https://photonics.ixblue.com/product/md/mxiq-ln-30.

[77] P. Cheinet et al. "Compact laser system for atom interferometry." In: *Appl. Phys. B* 84 (2006), pp. 643–646. DOI: https://doi.org/10.1007/s00340-006-2266-2.

[78] Fabien Theron et al. "Narrow linewidth single laser source system for onboard atom interferometry". In: *Appl. Phys. B* 118 (2015), pp. 1–5. DOI: https://doi.org/10.1007/s00340-014-5975-y.

[79] Jie Fang et al. "Realization of a compact one-seed laser system for atom interferometer-based gravimeters". In: *Opt. Express* 26.2 (2018), pp. 1586–1596. DOI: 10.1364/OE.26.001586.

[80] Xiaowei Zhang et al. "Compact portable laser system for mobile cold atom gravimeters". In: *Appl. Opt.* 57.22 (2018), pp. 6545–6551. DOI: 10.1364/AO.57.006545. URL: http://ao.osa.org/abstract.cfm?URI=ao-57-22-6545.

[81] Fabien Theron et al. "Frequency-doubled telecom fiber laser for a cold atom interferometer using optical lattices". In: *Opt. Comms.* 393 (2017), pp. 152–155. DOI: https://doi.org/10.1016/j.optcom.2017.02.013.

[82] RIO. *RIO, GRANDE*. 2020. URL: https://rio-lasers.com/1550-nm-high-power-laser-module/.

[83] Keopsys. *CEFA-C-PB*. 2020. URL: https://www.keopsys.com/portfolio/cw-erbium-fiber-amplifier-c-pb-lp-series/.

[84] AA Opto-Electronic. *MT80-IIR30*. 2020. URL: http://www.aaoptoelectronic.com/wp-content/uploads/2018/08/MT40-MT80-MT110-MT160-MT200-IIR-Fio-VSF-ed1-18.pdf.

[85] NTT Electronics. *WH-0780*. 2020. URL: http://52ebad10ee97eea25d5e-d7d40819259e7d3022d9ad5r84.cf3.rackcdn.com/UK_NEL_WH-1064-000-F-B-C%5C%20-1064-SHG-Module_DS.pdf.

[86] Laser Components. *EOL 1×4 NIR*. 2020. URL: https://www.lasercomponents.com/fileadmin/user_upload/home/Datasheets/divers-lwl/switch/optical_switch_pm1x2.pdf.

[87] G. C. Bjorklund, M.D. Levenson, and C. Ortiz. "Frequency modulation (FM) spectroscopy". In: *Applied Physics B* 32 (1983), pp. 145–152. DOI: https://doi.org/10.1007/BF00688820.

[88] Jin-Bao Long et al. "Magnetic-enhanced modulation transfer spectroscopy and laser locking for 87Rb repump transition". In: *Opt. Express* 26.21 (Oct. 2018), pp. 27773–27786. DOI: 10.1364/OE.26.027773. URL: http://www.opticsexpress.org/abstract.cfm?URI=oe-26-21-27773.

[89] J.L. Hall et al. "Optical heterodyne saturation spectroscopy". In: *App. Phys. Lett.* 39 (1981), p. 680. DOI: https://doi.org/10.1063/1.92867.

[90] L. Earl, M. Langlois, and M. Holynski. *Laser System*. ZSR1208B. 2020.

[91] C. V. Rammeloo. "Optimisation of a compact cold-atoms interferometer for gravimetry". PhD thesis. University of Birmingham, 2018.

[92] Sheng-wey Chiow et al. "102$\hbar k$ Large Area Atom Interferometers". In: *Phys. Rev. Lett.* 107 (13 2011), p. 130403. DOI: 10.1103/PhysRevLett.107.130403. URL: https://link.aps.org/doi/10.1103/PhysRevLett.107.130403.

[93] Alexander J. Dunning. *Coherent Atomic Manipulation and Cooling*. Springer Theses, 2015.

[94] E. Black. "An introduction to Pound–Drever–Hall laser frequency stabilization". In: *American Journal of Physics* 69 (2001), p. 79. DOI: https://doi.org/10.1119/1.1286663.

[95] Storm Weiner et al. "A Flight Capable Atomic Gravity Gradiometer With a Single Laser". In: Mar. 2020, pp. 1–3. DOI: 10.1109/INERTIAL48129.2020.9090014.